ScuDo

Scuola di Dottorato ⤳ Doctoral School

WHAT YOU ARE, TAKES YOU FAR

Doctoral Dissertation

Doctoral Program in Electronics Engineering (29thcycle)

Experimental and Theoretical Analysis of Soft Magnetic Materials for Power Applications

By

Mahmood Khan

******

Supervisor(s):

Prof. Carlo Stefano Ragusa

Dr. Carlo Appino

Doctoral Examination Committee:

Prof. Zsolt Szabo, Referee, Budapest University of Technology and Economics, Budapest, Hungary.

Prof. Antonino Laudani, Referee, Università ROMA TRE, Rome, Italy.

Prof. Andrea Cristofolini, Università di Bologna, Bologna, Italy.

Prof. Luca Giaccone, Politecnico di Torino, Italy.

Prof. Maria Cristina Piccirilli, Università di Firenze, Firenze, Italy.

Politecnico di Torino

2017

Declaration

I hereby declare that the contents and organization of this dissertation constitute my own original work and does not compromise in any way the rights of third parties, including those relating to the security of personal data.

Mahmood Khan

2017

I would like to dedicate this thesis to my loving parents, beloved wife, sisters and parents-in-law

Acknowledgements

First of all, I would like to thank Almighty ALLAH for HIS countless blessings. Indeed, nothing is possible without HIS help and guidance.

I would like to express my deepest appreciation to my advisor, Professor Carlo Stefano Ragusa, for his consistent support, related research, motivation and great knowledge throughout my PhD study. I thank him for his supervision and indeed it is a great honor to work under his supervision. This dissertation wouldn't have been possible without his guidance.

I would like to express my deepest thanks to my co-supervisor, Dr. Carlo Appino working at Istituto Nazionale di Ricerca Metrologica (INRIM). I thank him for his endless help while performing lab activities at INRIM and especially for his valuable suggestions in this dissertation. I also thank him for his availability, encouragement, guidance and helping me out whenever required.

My sincere thanks goes to Dr. Olivier de la Barrière who gave me an opportunity to work in his research laboratory at "Ecole normale supérieure de Cachan". I am grateful to his hospitality during my stay and for granting me access to the research facilities. Without his precious support, novel hardware designs, innovative ideas and stimulating discussions, it would not have been possible to conduct my research activities.

Abstract

The efficiency of electrical machines carries a global impact because they fulfill about three quarters of global electrical energy consumption. Its improvement requires a sound knowledge of energy loss properties of magnetic materials used in the core of electrical machines, especially non conventional supply conditions, such as non-sinusoidal, high induction, alternating (1-D) and rotating (2-D) flux waveforms that have been posed with the incorporation of new electronic devices and materials in the systems. For these reasons, novel theoretical models and experimental techniques need to be developed to obtain the loss behavior under these complex flux regimes. To address these issues, experimental investigation and theoretical analysis have been carried out in this thesis on different magnetic materials and a wide ensemble of supply conditions.

The aim of the theoretical analysis was to fill the gap between the physicists and the engineers by developing simple models that can be applied to compute the loss under realistic supply conditions. This theoretical frame is rooted in the physical principle of the separation of loss and the Statistical Theory of Loss (STL) by which the loss can be separated into the hysteresis, classical, and excess components. The concept of loss separation has been exploited under 1-D flux and extended to 2-D fluxes, where the relations between alternating and rotational losses have been obtained on a number of different materials, this analysis restricted to the region not influenced by skin effect. The proposed theoretical models have been tested by comparing loss figure of different magnetic materials over a wide range of fre-

quencies, induction levels, and conventional or non-conventional supply conditions. To this purpose, loss characterization of non-oriented Fe-(3.2wt %)Si steels have been performed using a three phase magnetizer able to generate 1-D and 2-D flux patterns, up to saturation magnetization. Fieldmetric and Thermometric methods have been applied at low and very high induction levels. Loss characterization of other non-oriented Fe-Si and low carbon steels have also been performed under 1-D flux at very low and high sinusoidal inductions using Epstein frame, single sheet tester or ring samples, over frequencies ranging from quasi-static conditions up to 10 kHz. Systematic uncertainties have been observed in measurements using a Single Sheet Tester due to MMF drop in flux closing yoke and a compensated Permeameter has been designed to reduce these uncertainties by compensating the MMF drop in the flux closing yoke.

Contents

List of Figures

List of Tables

Nomenclature

Acronyms / Abbreviations

$1-D$ One dimensional

$2-D$ Two dimensional

B Magnetic Flux Density

$CSST$ Compensated Single Sheet Tester

H Magnetic Field

$INRIM$ Istituto nazionale di ricerca metrologica

LCS Low Carbon Steel

MC Magnetization Current

MMF Magnetomotive force

MO Magnetic Objects

MSE Modified Steinmetz Equation

Mt Metric Ton

SE Steinmetz Equation

SMM Soft Magnetic Material

SST   Single Sheet Tester

STL   Statistical Theory of Loss

SWM   Saturation Wave Magnetization

WCM   Wolfson Centre for Magnetics

Chapter 1

Introduction

According to the International Energy Outlook 2016 [1], compiled by the US Energy Information Administration, CO_2 emissions related to energy tends to increase from 32.3 billion Mt in 2012 to 35.6 billion Mt, and are expected to reach 43.2 billion Mt in 2040. At the same time, the world's net electricity generation is expected to increase from 21.6 trillion kWh in 2012 to 25.8 trillion kWh in 2020. About 70% of electricity is produced from fossil fuels and almost 46% of electrical energy is supplied to electrical motors driven systems according to International Energy Agency in 2011 [2]. Therefore, electrical machines are indirectly responsible for producing a significant amount of CO_2 emissions and thus the efficiency of electrical machines carries a global impact.

In order to improve it, a basic step is a sound knowledge of the energy loss properties of magnetic materials used in the core of the machines. Since many decades, the process of physical modeling and magnetic characterization of materials has been addressed. However, the invention of new devices, the discovery of new materials, and the widening of applications, have resulted in new experimental and theoretical challenges. For instance, a trend towards high working frequency operation has been observed in recent times. In addition, because of the application of
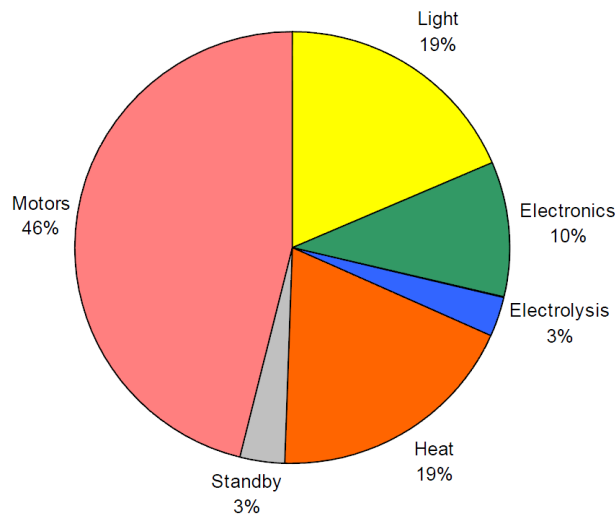
Fig. 1.1   Worldwide consumption of electrical energy adapted from IEA report 2011 [2]. About 46% of electrical energy is utilized by electrical motors, that are indirectly responsible of producing significant amount of CO_2 emissions.

switched mode power supplies and electronic drives, the magnetic cores of electrical machines have to go through growing complex non-sinusoidal flux waveforms [3]. New problems also appear when dealing with high velocity electrical machines used in powertrain applications because, for compactness reasons, levels of induction closed to magnetic saturation and frequencies in the kHz range are encountered [4]. Therefore, in order to deal with such complex regimes, novel experimental and theoretical models need to be developed.

Losses in electrical machines can be classified into ohmic loss, mechanical loss, and iron loss. Out of these, ohmic and mechanical loss are sufficiently recognized, but determining iron loss can be a complex task because their modeling rely on experimental data which can be difficult to obtain under such complex regimes of fluxes. As an example, in a single phase transformer the flux density changes sinusoidally versus time along a specific direction. This behaviour is termed as alternating or 1-Dimensional (1-D) flux. On the other end, in three phase transformer's T-joints and in the cores of rotating machines, flux density vector can rotate within. This is known as rotational flux or 2-Dimensional (2-D) flux. Under normal practical conditions,

both alternating and rotating fluxes coexist as shown in Fig. 1.2, adapted from [5]. The response of magnetic materials under 2-D flux is very different from 1-D flux, especially at high induction level [6, 7]. Therefore, an advanced charaterization requires both 1-D and 2-D flux regimes, at different frequencies and induction levels. Measurements under 1-D flux up to medium-high induction levels, far from saturation regimes, have become standardized. Epstein frames and Single Sheet Testers are used widely in the industry for this purpose [8, 9]. Since the last century, many researchers have investigated rotational core losses. Baily [6], in 1896, obtained results under alternating and rotating magnetic fields. It was noticed, for the first time, that the rotational loss decreases drastically approaching saturation, as reported in Fig.1.3. On the other end, measurements under 2-D fluxes are even more confined as compared to 1-D measurements, and still far from standardization.
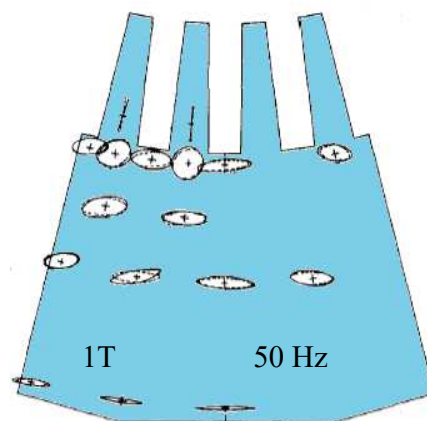
Fig. 1.2   Flux loci measured in the stator of an electrical machine at 50 Hz. Pairs of mutually orthogonal search coils were wound through holes in the sheet to detect flux loci (adapted from [5]).

The determination of magnetic loss in soft magnetic materials at high induction levels has always been challenging [10–12], because conventional power loss measurement carried out according to standard procedures, i.e measuring hysteresis loop area, cannot be applied upon approaching saturation. It is because the power factor becomes very low and the signals related to B and H are nearly in quadrature [13]. Under these conditions, the loss should be obtained from the measurement

of the rate of rise of the temperature of the magnetized sample. This procedure is called thermometric method, and can be employed because it is not influenced by low power factor [14, 15]. An additional issue is due to the control of the induction waveform at such high inductions [16–18], that is in general fairly critical.

For optimum modeling and efficient design, engineers need to take into account the core behavior of electrical machines under such complex regimes, but because of a lack of experimental data under 2-D flux, they can use only the available data obtained under alternating conditions: a situation far from the real conditions. For these reasons, the extension of magnetic characterization to such complex scenarios is the need of the day.
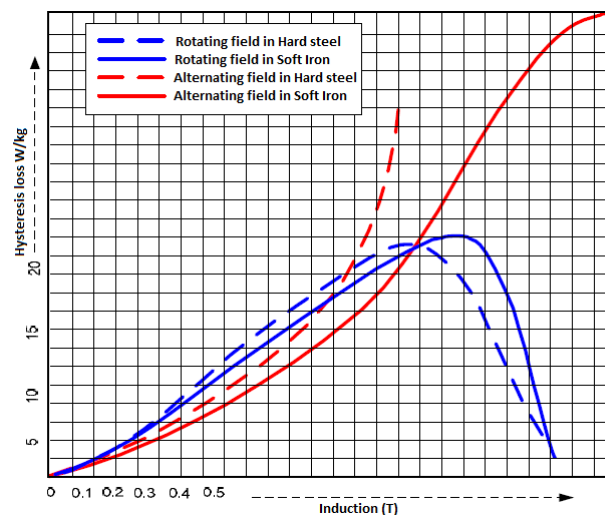
Fig. 1.3 Alternating and rotational loss in soft iron and hard steels at different induction levels [6]. It was observed for the first time that rotational loss (represented by blue colour), decreases significantly at high inductions.

1.1   Goal of the thesis

The main focus of this dissertation is to bridge the gap between physicists and electrical machine designers by providing loss behavior of magnetic materials through suitable experimental techniques and their theoretical analysis via iron loss models, and statistical theory of loss in particular. We have investigated the energy loss over a wide range of frequencies and induction levels, from very low values up to saturation, both under 1-D and 2-D fluxes. Even though the adopted approach has been mainly experimental, assessed iron loss models have been exploited to evaluate and validate the results, and new theoretical analyisis have been pursued. Epstein strips and ring samples have been measured under 1-D conditions, whereas circular samples have been investigated under 2-D flux loci. Alternating measurements have also been performed on circular samples in order to compare them with the one obtained via Epstein frame.

1.2 Thesis outline

The manuscript is divided into the following chapters:

Chapter 1: discusses introduction, goals, and motivation. The list of scientific publications originated from this dissertation is presented.

Chapter 2: discusses energy loss models. The Statistical Theory of Loss (STL) and the related loss separation procedure are explained. These concepts representing the theoretical background upon which the work is based.

Chapter 3: illustrates the main experimental techniques used for magnetic loss measurements together under 1-D and 2-D conditions. The setups utilized for energy loss measurements are described.

Chapter 4: this chapter presents a novel compensated single sheet tester featuring a compensation scheme for the accurate determination of magnetic loss in materials. Results obtained in non-oriented and grain-oriented materials are reported.

Chapter 5: alternating and rotational losses up to very high induction levels in non-oriented Fe-Si are discussed.

Chapter 6: broadband energy loss behavior in different non-oriented Fe-Si and low-carbon steel sheets at very high and very low induction are presented. In particular, the role of classical losses is evaluated and discussed.

Chapter 7: reports the conclusion and future work.

1.3   List of scientific publications

Following is the list of Journal and conference publications that originated from this dissertation.

Journal Publications :

• Carlo Appino, **Mahmood Khan**, Olivier de la Barrière, Carlo Ragusa, and Fausto Fiorillo, "Alternating and rotational losses up to magnetic saturation in non-oriented steel sheets," *IEEE Transactions on Magnetics*, vol. 52, no. 5, 2016, 7404019.

• Olivier de la Barriere, Carlo Ragusa, **Mahmood Khan**, Carlo Appino, Fausto Fiorillo, and F. Mazaleyrat, "A simple compensation method for the accurate measurement of magnetic losses with a single strip tester," *IEEE Transactions on Magnetics*, vol. 52, no. 5, 2016, 7404008.

• Carlo Ragusa, Hanyu Zhao, Carlo Appino, **Mahmood Khan**, Olivier de la Barrière, and Fausto Fiorillo, "Loss decomposition in non-oriented steel sheets: the role of the classical losses," *IEEE Magnetics Letters*, vol. 7, no. 1 (2016), 7556414.

Conference Publications :

• Carlo Appino, Fausto Fiorillo, Mauro Zucca, Olivier de la Barriere, Carlo Ragusa and **Mahmood Khan**, "Magnetic losses up to saturation in non-oriented steel laminations," 7th International Conference on Magnetism and Metallurgy, Rome, Italy, 2016.

• Carlo Ragusa, Hanyu Zhao ,Carlo Appino, **Mahmood Khan**, Olivier de la Barrière, and Fausto Fiorillo, "Loss decomposition and classical losses in non-oriented steel sheets," 14th International Workshop on 1 and 2-Dimensional Magnetic Measurement and Testing, Tianjin, China, 2016.

• Carlo Ragusa, Hanyu Zhao ,Carlo Appino, **Mahmood Khan**, Olivier de la Barrière, and Fausto Fiorillo," Magnetic losses versus frequency in non-oriented steel sheets and their prediction: the limits of the analytical approach," accepted for presentation at IEEE International Magnetics Conference, Dublin, 2017.

Chapter 2

Overview of iron loss models

In modern applications, such as renewable energy production and powertrain system [4, 19], the optimum design of electrical machines is a very complicated task, because a number of requirements and constraints need to be satisfied at the same time. In particular, torque density, efficiency, cost, weight, and reliability have to be taken into account [20, 21]. Stochastic algorithms, often employed to solve such multi-objective design problems, require the evaluation of a large number of design configurations, to achieve the optimum. The best trade-off between the computation time and the accuracy is therefore required.

The accuracy of iron loss models play a very important role in optimization procedures because they have a major influence on the final efficiency of the electrical machine [22]. Iron loss models can be classified into three main categories. The first category is based on heuristic formulas, e.g. the Steinmetz formula (extensively applied in electrical engineering [23]), provides simple and fast analytical expressions. By means of these models, the power loss is obtained under sinusoidal flux as a function of peak induction and frequency. Several modifications of these phenomenological models have been proposed to extend their application to distorted regimes. They will be discussed in section 2.1.

In the second category we classify the physical models based on the loss separation principle, where the total loss is assumed to be made of hysteresis, classical, and excess loss components. This approach is explained in section 2.2.

The last category is based on hysteresis models. By these models, static and dynamic J-H behavior can be represented under generic induction waveforms. Examples are the well known classical Preisach model [24] and the dynamic Preisach model [25]. The hysteresis models can be introduced into electromagnetic solvers to predict loss distribution in complicated magnetic cores. Such models require a preemptive set of experimental data not always available to the designers.

2.1   Steinmetz-like formulas

2.1.1   Standard Steinmetz formula

This category of models originates from the Steinmetz equation [26] given by

$$P_{\text{tot}} = C_{\text{SE}} f^{\alpha} B_{\text{p}}^{\beta}, \tag{2.1}$$

where f is the frequency, B_{p} is the peak induction, C_{SE}, α and β are suitable constants depending upon the materials. At very low frequencies, where the total loss can only be attributed to hysteresis loss, the value of β is almost equal to 1.6. At high frequencies, α, β and C_{SE} can be obtained via curve fitting techniques of Eq. 2.1 with experimental data. It is worth noting that the exponents α and β can change significantly with frequency and peak induction. Table 2.1 reports some typical values of β for a grain-oriented 3% Fe-Si steel sheet, at different peak inductions and frequencies [27]. Table 2.2 reports variation in the values of α for a medium frequency power transformer ferrite [28]. Another key point to note is that the classical Steinmetz equation is valid only for sinusoidal waveforms. However, as the

material can be subjected to non-sinusoidal flux, numerous attempts have been made to extend its applicability to non-sinusoidal waveforms. Some of the modifications are discussed in the following.

Table 2.1 Exponent β in Steinmetz equation 2.1 for a grain-oriented 3% Fe-Si at various frequencies and peak inductions.

Exponent β			Peak Induction (T)
f = 0 Hz	f = 50 Hz	f = 100 Hz	
1.57	1.84	1.6	0.7-1.0
3.53	2.653	2.6	1.5-1.7

Table 2.2 Variation of α for a medium frequency general purpose ferrite developed by Magnetics, Inc [28].

Ferrite Material	
Frequency Range	Frequency Exponent (α)
f <10 kHz	1.06
10 kHz < f <100 kHz	1.72
100 kHz < f <500 kHz	1.66
f >500 kHz	1.88

2.1.2 Modified Steinmetz equation

Following [29, 30], the standard Steinmetz equation has been extended to predict the material loss under arbitrary induction waveform as

$$P_{\text{tot}} = C_{\text{SE}} f_{\text{eq}}^{\alpha-1} B_{\text{p}}^{\beta} f, \tag{2.2}$$

where the equivalent frequency f_{eq} is given by

$$f_{\text{eq}} = \frac{2}{\Delta B^2 \pi^2} \int_0^T (dB/dt)^2 dt, \tag{2.3}$$

being

$$\Delta B = B_{\text{max}} - B_{\text{min}}. \tag{2.4}$$

Under a sinusoidal waveform of amplitude B_{p}, one finds

$$f_{\mathrm{eq}} = \frac{2}{4B_{\mathrm{p}}^2\pi^2} \int_0^T \omega^2 B_{\mathrm{p}}^2 \cos^2 \omega t = f, \qquad (2.5)$$

that is equation 2.1 is recovered.

A more general modification of Steinmetz equation is given in the Generalized Steinmetz Equation [31], where the loss is obtained as a function of flux density $B(t)$ and its derivative $\mathrm{d}B/\mathrm{d}t$. The power loss is given by

$$P_{\mathrm{tot}} = \frac{1}{T} \int_0^T C_{\mathrm{GSE}} |\mathrm{d}B/\mathrm{d}t|^\alpha |B(t)|^{\beta-\alpha} \, \mathrm{d}t \qquad (2.6)$$

where C_{GSE}, α and β are suitable constants depending upon the materials.

Despite the simplicity of Steinmetz-like equations, there are some limitations associated with this approach. In fact the coefficients depend significantly upon the input frequency and changes drastically when altered. Eventually it must be remarked that the Steinmetz models become less accurate over a wide range of frequency and degree of distortions.

2.2   Models based on loss separation

Adopting the loss separation approach, the energy loss W_{tot} is given by three components, the static hysteresis loss W_{hyst}, the classical loss W_{cl}, and the excess loss W_{exc}, as discussed in detail by Bertotti by means of the Statistical Theory of Losses (STL) [32]. Therefore, the loss can be written as

$$W_{tot} = W_{hyst} + W_{cl} + W_{exc}. \tag{2.7}$$

Each loss components will be discussed in the following.

2.2.1   Hysteresis loss

The hysteresis loss corresponds to the area of the hysteresis cycle obtained under quasi-static conditions, as shown in Fig. 2.1. In practice, the hysteresis loss is also obtained by extrapolating loss measurements up to $f = 0$ Hz, as shown in Fig. 2.2. Under quasi-static conditions, eddy currents dissipation mechanism still persist because the domain wall motion is not smooth and is blocked by pinning centers. Therefore the process takes place in a jerky manner, a phenomenon known as Barkhausen effect. The discrete jumps generate current pulses localized around the segment of the wall in motion, where time constant are very short as compared to the period of magnetization. Therefore it can be stated that hysteresis loss does not depend upon the rate of magnetization.
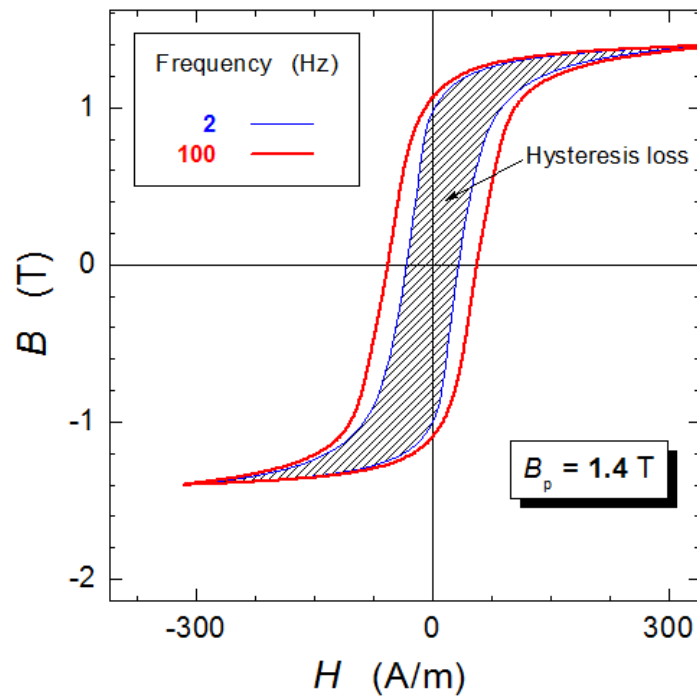
Fig. 2.1 $B - H$ loops at different frequencies, measured in 0.343 mm thick Fe-(3.2 wt%)Si-(0.5 wt%)Al along the longitudinal direction. The grey region represents the area of the $B(H)$ loop at $f = 2$ Hz (quasi-static condition) and is equal to the hysteresis loss.
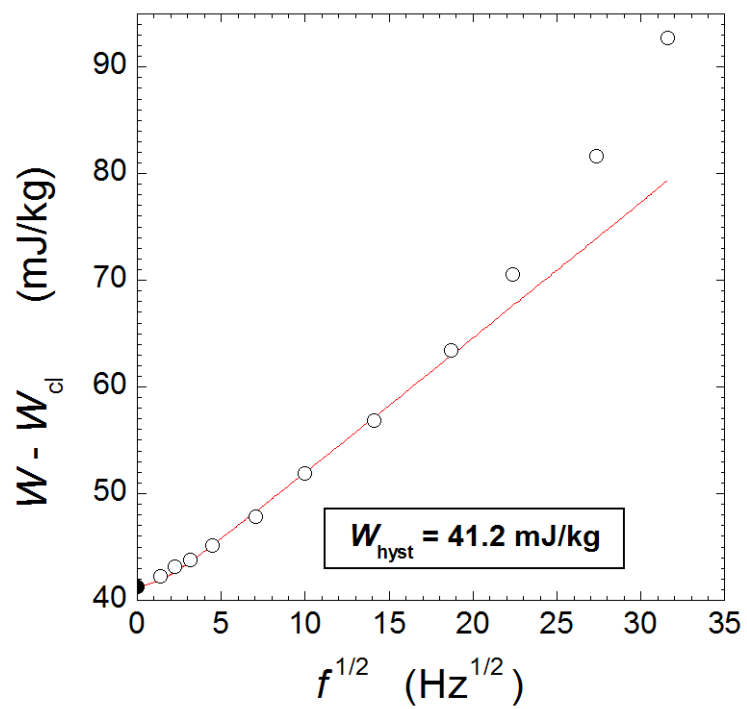
Fig. 2.2   The quantity W-W_{cl} at different frequencies obtained in a 0.35mm thick Fe-(3.2wt%)Si at B_p = 1.55T under 1D flux. The measurements have been extrapolated up to f = 0 Hz to obtain W_{hyst}.
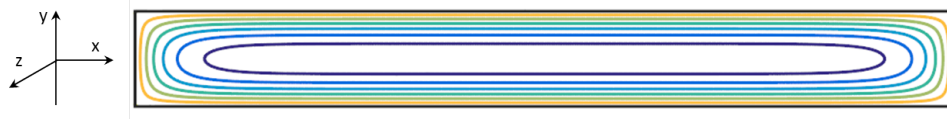
Fig. 2.3   Sample geometry for classical eddy current loss computation, where d is the thickness along the y axis. The sample is assumed infinitely long and the external field is applied along z axis. Under these assumptions, the induced eddy currents are confined to $x - y$ plane.

2.2.2   Classical loss

The classical loss component is the dynamic eddy current loss obtained by disregarding the magnetic structure. Let us calculate such loss for an electrical steel sheet of thickness d and conductivity σ (see Fig. 2.3) assuming the following conditions:

- the material is considered homogeneous;

- the thickness d is very small as compared to other dimensions;

- the magnetic field is applied along the z-direction and is represented by H_a;

In the low frequency limit, the effect of the induced eddy currents is small as compared to the applied field. Under such conditions, the induction B is approximated by taking its average over the slab cross section and is assumed independent of y. Applying Maxwell equations, we obtain

$$\frac{\partial H_z}{\partial y} = j_x, \tag{2.8}$$

and

$$\frac{\partial j_x}{\partial y} = \sigma \frac{dB_z}{dt}. \tag{2.9}$$

After deriving Eq. 2.8 and replacing $\partial j_x / \partial y$ through Eq. 2.9, we obtain

$$\frac{\partial^2 H_z}{\partial y^2} = \sigma \frac{dB_z}{dt}, \tag{2.10}$$

Integrating Eq. 2.9 w.r.t y, we obtain

$$j(y,t) = \sigma \frac{\mathrm{d}B}{\mathrm{d}t} y, \tag{2.11}$$

The following boundary conditions hold: $H = H_a$, for $y = \pm d/2$. After integration of Eq. 2.10, we obtain

$$H(y,t) = H_a(t) - \frac{\sigma}{2} \frac{\mathrm{d}B}{\mathrm{d}t} \left(\frac{d^2}{4} - y^2 \right). \tag{2.12}$$

The eddy currents generate a counterfield directed in opposite direction respect to H_a. It is worth noting that eddy current field will get strong with increase of the rate of change of magnetic induction. The instantaneous dissipated power is then obtained as

$$P_{cl}(t) = \frac{1}{d} \int_{-d/2}^{d/2} \frac{j^2(y,t)}{\sigma} dy = \frac{\sigma d^2}{12} \left(\frac{\mathrm{d}B}{\mathrm{d}t} \right)^2. \tag{2.13}$$

The loss per cycle under sinusoidal induction and negligible skin effect is then given by

$$W_{cl} = \int_0^T P_{cl}(t)\mathrm{d}t = \frac{< P_{cl}(t) >}{f} = \frac{\pi^2 \sigma d^2 f B_p^2}{6}. \tag{2.14}$$

where σ is the conductivity, B_p is the peak induction, and f is the frequency.

2.2.3   Excess loss

Weiss proposed the concept of magnetic domains within magnetic materials [33]. Magnetic domains are magnetized along different directions and are arranged in such a way so as to reduce the overall energy. Fig. 2.4 reports an example of domain structure for a single and polycrystal. The domains are separated by thin transitional regions known as domain walls or Block walls. When subjected to an external field,

domain walls movement drives eddy current paths around the Block walls that act as a source for the excess loss [34].
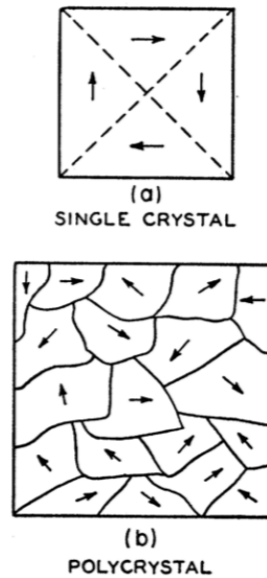
Fig. 2.4   Arrangement of domains for zero resultant magnetic moment in (a) single crystal and (b) polycrystalline specimen (adapted from [35]). The arrows correspond to the resultant magnetic moment of a single domain.

Single domain wall model

A fist step toward excess loss modelling was done by Williams, Shockley and Kittel in [36], who analyzed the Fe-Si single crystal shown in Fig. 2.5, and determined the velocity of propagation of the single domain boundary under weak and strong magnetic fields. The position of the domain wall (DW) was controlled by the magnetic field generated by the current in a coil wrapped around the sample. A secondary winding connected to a flux meter was used to measure the change of flux. The velocity of propagation of the single domain wall boundary was measured by timing the deflections on a flux meter with a stop watch. We will now discuss the wall dynamics under these conditions. Let us consider an electrical steel sheet of thickness d and conductivity σ, as shown in Fig. 2.6. It has a single domain wall
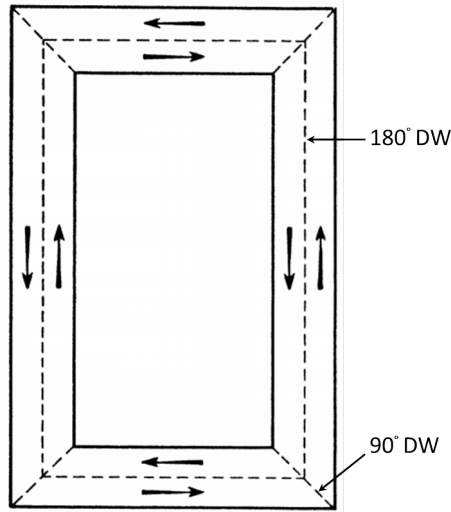
Fig. 2.5   A simple domain structure in a single cyrstal of Fe-Si (adapted from [36]). The rotation of magnetic field from one limb to another is controlled by four 90° domain walls (dashed oblique segments) existing in each of the four corners of the crystal. The arrows indicate the direction of local polarization.

located at $x = 0$. The field H_a is applied along the z direction. The flux ϕ can be computed from the position of the single domain wall x_w, as

$$\phi = 2J_s dx_w, \tag{2.15}$$

where $J_s = \mu_0 M_s$ is the saturation polarization. In addition

$$\frac{d\phi}{dt} = 2J_s dv_w, \tag{2.16}$$

where $v_w = dx_w/dt$ is the velocity of the wall. This is a 2D problem because the magnetization is directed along the z axis and the slab is supposed infinitely extended along the same direction. Therefore, the eddy current paths flow in the $x - y$ plane and are independent of z. If we assume a known $\phi(t)$ waveform, the eddy current loss can be obtained by solving Maxwell equations. From Ampere's law, we obtain

$$\mathrm{div}\, \vec{J} = 0, \tag{2.17}$$
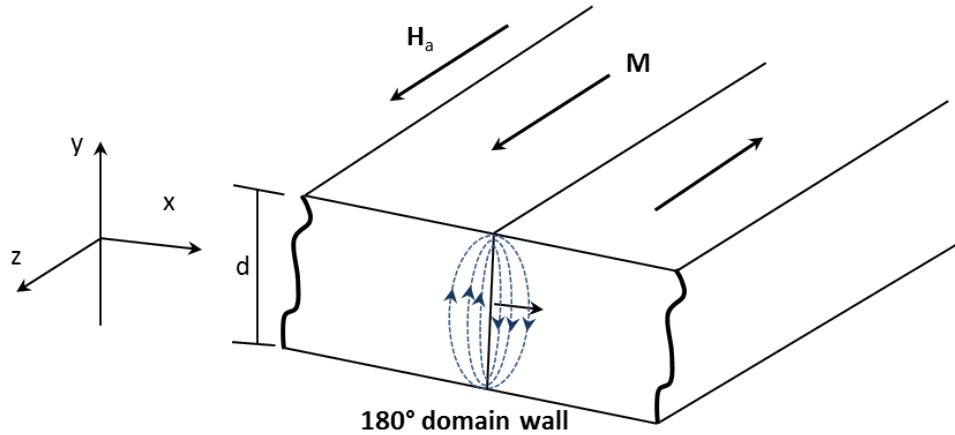
Fig. 2.6   A single magnetic domain wall for a sheet of thickness d and length l. The domain wall moves along the x direction under the action of the external field, and is surrounded by the induced eddy currents represented by dashed curves.

and from Faraday's law

$$\text{rot } \vec{J} = 0. \tag{2.18}$$

It is worth noting that Eq. 2.17 and 2.18 are obeyed everywhere except at domain wall position. The following boundary conditions hold

$$j_y(y = \pm\frac{d}{2}) = 0. \tag{2.19}$$

Around the moving domain wall, the application of Faraday's law provides

$$j_y(x = 0^-) = -j_y(x = 0^+) = \frac{\sigma}{2d}\frac{d\phi}{dt}, \tag{2.20}$$

where $x = 0$ represents the position of the wall. By solving together Eq. 2.17 and 2.18 under the given boundary conditions, the two components of eddy current density are computed. The eddy currents are approximately concentrated in a region of width d, and decreases exponentially as the distance is increased. The power dissipation is given by

$$P_w = \sigma G \left(\frac{d\phi}{dt}\right)^2, \qquad (\text{W}) \tag{2.21}$$
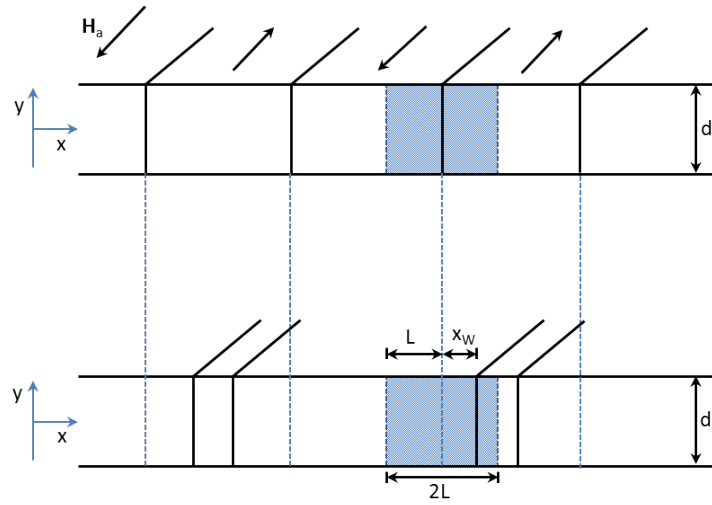
Fig. 2.7   Periodic domain walls with spacing 2L in a slab of thickness d along y direction in pry and bean model. The slab is assumed to have infinite length along z direction. With the application of the external field H_a along z axis, eddy currents are generated around each of the moving domain walls.

where $G \cong 0.1356$ is a dimensionless geometrical coefficient. The average power loss per unit volume of the slab, is given by

$$\frac{P_w}{V} = \frac{\sigma G}{S} \left(\frac{d\phi}{dt} \right)^2 = \sigma G S \left(\frac{dB}{dt} \right)^2, \qquad (W/m^3) \qquad (2.22)$$

where B is the average induction.

The loss can be compared to the one obtained under uniform flux distribution, $P_{cl}(t) = \sigma d^2 / 12 \, (dB/dt)^2$. The ratio is then

$$\frac{P_{w/V}}{P_{cl}} \sim \frac{12Gl}{d} > 1. \qquad (2.23)$$

Therefore, the power loss per unit volume with eddy currents concentrated around a single domain wall, is greater than the classical loss obtained by disregarding the magnetic structure.

Periodic domain walls model

Pry and Bean investigated the loss in a magnetic material by considering a set of identical 180° domain walls in an infinite slab as shown in Fig. 2.7. Each wall is displaced from its average position by the quantity $\pm x_w(t)$ and moves at a velocity $\pm v_w(t)$ under the action of the applied field H_a along the z-axis. The solution of Maxwell equations provide the following expression for the loss

$$P_{\text{PB}}(t) \cong \frac{\sigma}{2L} \left(\frac{d\phi}{dt} \right)^2 \frac{4}{\pi^3} \sum_{\text{odd}n} \frac{1}{n^3} \text{cth} \left(\frac{n\pi L}{d} \right), \qquad (2.24)$$

where $2L$ is the domain wall spacing.

For $2L \ll d$, i.e. domain size is small compared to the thickness of the slab, Eq. 2.24 provides

$$P_{\text{PB}}(t) \cong \frac{\sigma}{L^2} \left(\frac{d\phi}{dt} \right)^2 \frac{2}{\pi^4} \sum_{\text{odd}n} \frac{1}{n^4} = \frac{\sigma d^2}{12} \left(\frac{dB}{dt} \right)^2 = P_{\text{cl}} \qquad (2.25)$$

where $B(t)$ is the average induction in the slab. This means that as $2L \ll d$, the classical loss formula is recovered.

For $2L \gg d$, Eq. 2.24 becomes

$$P_{\text{PB}}(t) \cong \frac{\sigma G}{2Ld} \left(\frac{d\phi}{dt} \right)^2 = \frac{1}{2Ld} P_W(t) \cong 1.63 \frac{2L}{d} P_{\text{cl}}(t). \qquad (2.26)$$

Here, the influence of magnetic domains structure is expressed by the ratio $2L/d$. The additional loss due to magnetic domains becomes greater as the size of the magnetic domains $2L$ exceeds the thickness d. Fig. 2.8 illustrates this point showing the loss versus number of domain walls at a given average induction. It can be observed that the loss decreases with increase in the number of domain walls and finally becomes equal to the classical loss (Eq. 2.14). In addition, Fig. 2.9 shows eddy current patterns for different numbers of domain walls. Initially, eddy currents
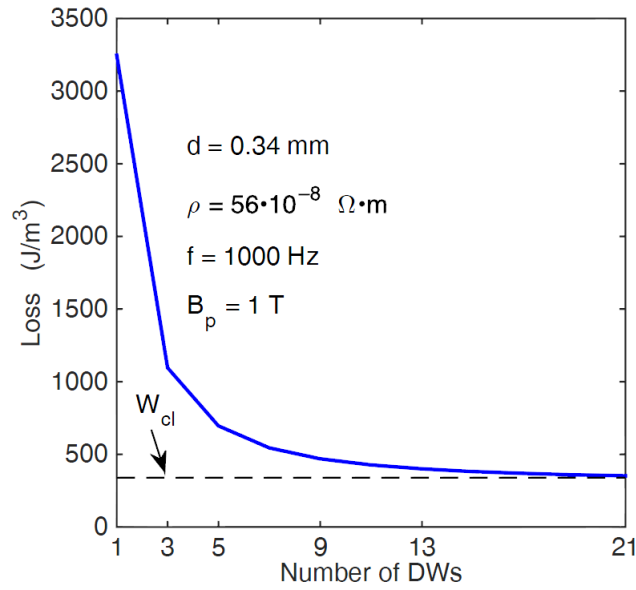
Fig. 2.8   Total loss vs. number of domain walls for a 0.34mm thick and 2mm long slab obtained by numerical simulation. It can be seen that the loss decreases with increase in the number of domain walls and ultimately becomes equal to the classical loss (Eq. 2.14).

are concentrated around domain walls only. Later, by increasing the number of domain walls (i.e. decreasing DW spacing 2L), the eddy currents interaction is increased and form patterns that are distributed all across the sheet.

Random Domain walls model

In real materials, the domain size and shape is not fixed because it changes from place to place and time. In order to take into account such random domain structure, Bertotti [37] introduced disorder through a statistical approach, ending with the following expression for the loss

$$P_{RW}(t) = P_{cl}(t) + \frac{\lambda}{d}\langle P_{w}(t)\rangle. \qquad (2.27)$$

Here, the first term is the classical loss obtained by dissregarding the magnetic structure (Eq. 2.13). The second term is the excess power, where $P_{w}(t)$ is the average
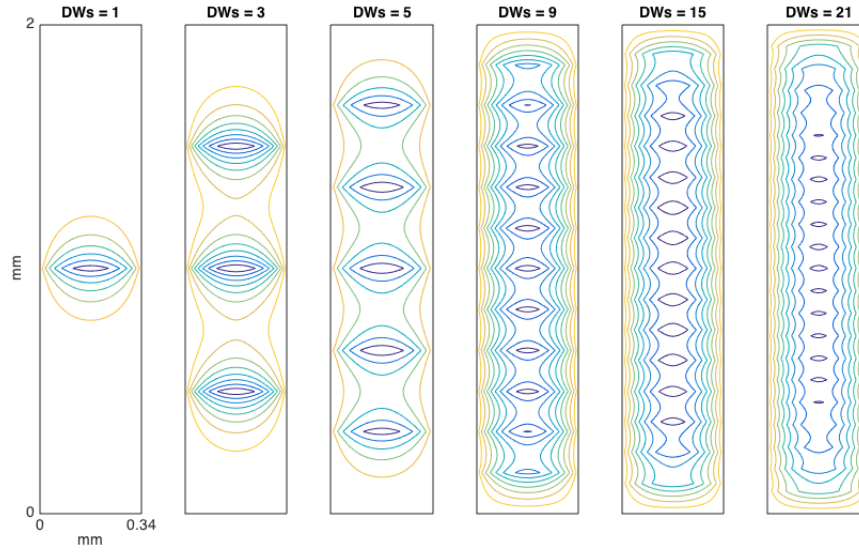
Fig. 2.9   Eddy current patterns for different number of domain walls simulated in a 0.34mm thick and 2mm long steel sheet. With few domain walls, the eddy currents are concentrated around domain walls only. By increasing the number of domain walls, the eddy currents interaction is increased and form patterns that are distributed all across the sheet.

power dissipated across each wall and λ is the average density of walls, being $1/\lambda$ the average domain wall spacing. The theory can now be applied to find a suitable expression for the excess loss in a real material.

We begin to consider the excess field given by

$$H_{\text{exc}} = P_{\text{exc}}/(\mathrm{d}\phi/\mathrm{d}t) \tag{2.28}$$

So, the excess field due to a single domain wall can be written as

$$H_{\text{exc}} = \sigma G \frac{\mathrm{d}\phi^{(\text{w})}}{\mathrm{d}t}, \tag{2.29}$$

In case of n active walls, the total flux rate should be equal to the required average flux rate. One can therefore write

$$n\frac{\mathrm{d}\phi^{(\mathrm{w})}}{\mathrm{d}t} = S\frac{\mathrm{d}J}{\mathrm{d}t}, \tag{2.30}$$

where $\mathrm{d}J/\mathrm{d}t$ is the polarization rate and S is the cross sectional area. The flux rate per wall is then

$$\frac{\mathrm{d}\phi^{(\mathrm{w})}}{\mathrm{d}t} = \frac{S}{n}\frac{\mathrm{d}J}{\mathrm{d}t}, \tag{2.31}$$

Therefore, Eq. 2.29 becomes

$$H_{\mathrm{exc}} = \frac{\sigma G S}{n}\frac{\mathrm{d}J}{\mathrm{d}t}. \tag{2.32}$$

It is only valid in case of large wall spacing $(2L >> d)$ [32], but fails when it is applied to fine domain structure $(2L <<< d)$. For fine domain structures, one can start from the physical description of domain structure dynamics supported by Barkhausen noise experiments where the magnetization proceeds through large magnetization clusters due to strong internal correlation fields. For such a cluster, we can write

$$P_{\mathrm{exc}} = \sigma G^{(\mathrm{is})}\frac{\mathrm{d}\phi^{(\mathrm{cl})}}{\mathrm{d}t}\frac{\mathrm{d}J}{\mathrm{d}t}. \qquad (\mathrm{W/m^3}) \tag{2.33}$$

where $G^{(\mathrm{is})}$ is a function of the internal structure while $\mathrm{d}\phi^{(\mathrm{cl})}/\mathrm{d}t$ is the average flux associated with the magnetization cluster [38]. Thus one can say that even in the fine domain structures, there is a high probability that the active wall is surrounded by many other active walls that form "Magnetic Objects" (MO) and are in-turn distributed randomly. MOs play the same role as active domain walls but with different eddy current damping effects due to different internal structures. They have different structural and dynamic properties in different materials evolving from one domain wall for $(2L >> d)$ to a magnetization cluster for $(2L <<< d)$. If an MO has a damping coefficient $G^{(\mathrm{x})}$ and flux rate $\mathrm{d}\phi^{(\mathrm{x})}/\mathrm{d}t$ and is distributed randomly, we
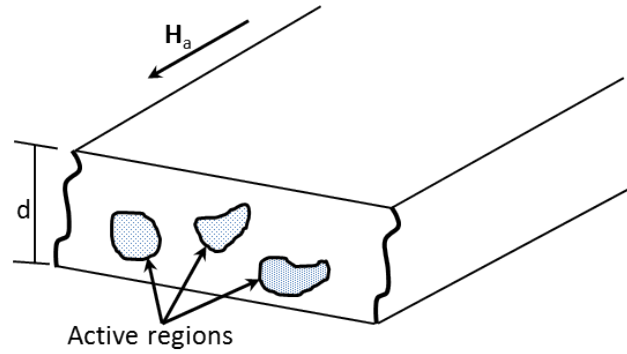
Fig. 2.10   Magnetic objects randomly distributed in a material that play the same role as active domain walls but with different eddy current damping effects due to different internal structures. MOs have different structural and dynamic properties in different materials.

can write the following equation

$$H_{\text{exc}} = \sigma G^{(\text{x})} \frac{\mathrm{d}\phi^{(\text{x})}}{\mathrm{d}t} \qquad , \tag{2.34}$$

In case of a number of n simultaneously active MOs, the same equation becomes

$$H_{\text{exc}} = \frac{\sigma G^{(\text{x})} S}{n} \frac{\mathrm{d}J}{\mathrm{d}t} \qquad , \tag{2.35}$$

Let us introduce the factor $\tilde{n} = nG/G^{(\text{x})}$, the effective number of active MOs. Eq. 2.34 then becomes

$$H_{\text{exc}} = \frac{H^{(\text{x})}}{\tilde{n}} \qquad . \tag{2.36}$$

where $H^{(\text{x})} = \sigma GS\mathrm{d}J/\mathrm{d}t$ is the excess field in a material where whole flux change is concentrated in a single $180°$ domain wall. This equation states that the excess field decreases with increase in the number of active MOs.

The magnetization process is highly inhomogeneous if the frequency is low. It is because there are very few active correlation regions in the sample. By increasing the applied field pressure (increasing frequency) higher flux rates in the active regions

will be produced. This applied field pressure will not only concentrate on the already active regions but also upon the rest of material. It can therefore result in the activation of other non-active MOs in the material. Hence, the magnetization process becomes more and more homogeneous with increasing frequency. These mechanisms are governed by the pressure due to applied field which in turn is controlled only by excess field in this case. Thus, we can say that $\tilde{n}$ is a general function of H_{exc} and it increases with increasing H_{exc}. The first order expansion of $\tilde{n}(H_{\text{exc}})$ is given by

$$\tilde{n}(H_{\text{exc}}) = n_0 + H_{\text{exc}}/V_0 + \ldots\ldots \tag{2.37}$$

where n_0 is the number of magnetically correlated regions (MO) in the sample when frequency approaches zero and V_0 is a statistical parameter that represents the pressure induced on other magnetic objects (MO) to try to align them in the same direction. Hence there are two competing mechanisms: Eq. 2.36 states that H_{exc} decreases with an increase in the number of active magnetic objects. On the other end, Eq. 2.37 states that the number of active regions increase when H_{exc} is increased. In the field range where Eq. 2.37 remains valid, one can obtain the following result by incorporating $\tilde{n}$ in Eq. 2.36

$$H_{\text{exc}}(n_0 + H_{\text{exc}}/V_0) = H^{(\text{w})}. \tag{2.38}$$

Solving for H_{exc}, one can then obtain the following equation

$$H_{\text{exc}} = \frac{n_0 V_0}{2}(\sqrt{1 + 4H^{(\text{w})}/n_0^2 V_0} - 1). \tag{2.39}$$

At low magnetization rates where $4H^{(\text{w})}/n_0^2 V_0 \ll 1$, Eq. 2.39 becomes

$$H_{\text{exc}} \cong H^{(W)}/n_0 \equiv \frac{\sigma G S}{n_0}\frac{\mathrm{d}J}{\mathrm{d}t}, \tag{2.40}$$

At high magnetization rates, where $4H^{(\mathrm{w})}/n_0^2 V_0 \gg 1$, Eq. 2.39 becomes

$$H_{\mathrm{exc}} \cong \sqrt{H^{(\mathrm{w})}V_0} \equiv \sqrt{\sigma GSV_0}\left(\frac{\mathrm{d}J}{\mathrm{d}t}\right)^{1/2}, \qquad (2.41)$$

Thus, the whole problem is conveniently solved with two phenomenological parameters, n_{o} and V_{o}. A general expression for excess power loss P_{exc} under arbitrary induction waveforms based on Bertotti's statistical theory of loss is given by

$$P_{\mathrm{exc}}(t) = \frac{n_{\mathrm{o}}V_{\mathrm{o}}}{2}\left(\sqrt{1 + \frac{4\sigma GSV_{\mathrm{o}}}{n_{\mathrm{o}}^2 V_{\mathrm{o}}^2}|\dot{J}(t)|} - 1\right)|\dot{J}(t)|. \qquad (2.42)$$

Here, $\dot{J}(t)$ is the time derivative of the magnetic polarization, $G \cong 0.1356$ and S is the cross-sectional area of the material. Normally V_{o} and n_{o} are very small, hence the following relation is normally assumed at typical applicative frequencies

$$\frac{4\sigma GSV_{\mathrm{o}}}{n_{\mathrm{o}}^2 V_{\mathrm{o}}^2}|\dot{J}(t)| \gg 1, \qquad (2.43)$$

Therefore, Eq. 2.42 correspondingly reduces to

$$P_{\mathrm{exc}} \cong \sqrt{\sigma GSV_{\mathrm{o}}}|\dot{J}(t)|^{3/2}, \qquad (2.44)$$

The excess energy loss can be obtained by integrating Eq. 2.44

$$W_{\mathrm{exc}} \cong \sqrt{\sigma GSV_{\mathrm{o}}}\int_0^T |\dot{J}(t)|^{3/2}\mathrm{d}t. \qquad (2.45)$$

Equation 2.45 can be applied to any desired waveform. For a sinusoidal $J(t)$, it becomes

$$W_{\mathrm{exc}} \cong 8.76\sqrt{\sigma GSV_{\mathrm{o}}}J_{\mathrm{p}}^{3/2}f^{1/2}, \qquad (2.46)$$

while for triangular $J(t)$ Eq. 2.45 provides

$$W_{\text{exc}} \cong 8\sqrt{\sigma GSV_o}J_p^{3/2}f^{1/2}. \tag{2.47}$$

When condition in Eq. 2.43 cannot be assumed, the integration of Eq. 2.42 provides under sinusoidal $J(t)$

$$W_{\text{exc}}(f) = 2n_0V_0J_p \cdot \int_0^{\pi/2} \left(\sqrt{1 + \frac{8\sigma GSV_0}{n_0^2 V_0^2}\pi f J_p \cos\phi} - 1 \right) \cos\phi \, d\phi \tag{2.48}$$

In all cases where the conditions mentioned in Eq. 2.43 cannot be assumed, Eq. 2.48 should be applied to obtain the excess loss. Finally, the total loss under a sinusoidal $J(t)$ is given by

$$W_{\text{tot}} = W_{\text{hyst}} + \frac{\pi^2 \sigma d^2 f B_p^2}{6} + 8.76\sqrt{\sigma GSV_o}J_p^{3/2}f^{1/2} \tag{2.49}$$

It must be noted that Eq. 2.49 holds only if the skin effect is negligible [39]. It is because the standard classical loss equation, incorporated in the model, cannot be applied with the emergence of skin effect.

2.3   Loss separation procedure

The loss separation procedure is the method by which the different loss components are obtained. The procedure is discussed as follows.

The first step is to measure the total loss. After that, the classical loss is computed by using Eq. 2.14. The third step is to obtain W_{diff}, given by

$$W_{\text{diff}} = W_{\text{tot}} - W_{\text{cl}}. \tag{2.50}$$
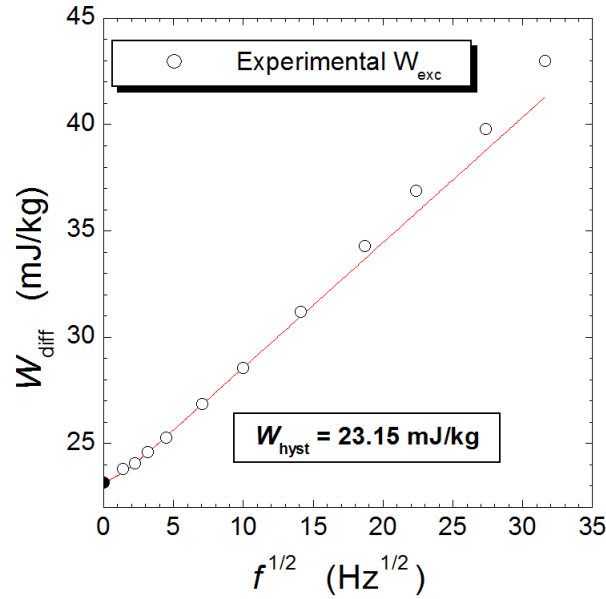
Fig. 2.11   A loss separation procedure has been applied to a 0.35mm thick Fe-(3.2wt%)Si at B_p = 1.2 T under 1D flux. The quantity $W_{diff} = W_{tot} - W_{cl}$ is obtained (open circles) and then extrapolated up to $f = 0$ to obtain W_{hyst}.

An example of such procedure is reported in Fig. 2.11, for a Fe-(3.2wt%)Si lamination at B_p = 1.2 T, showing the quantity $W_{diff} = W_{tot}$ - W_{cl} vs. $\sqrt{f}$. Here, W_{diff} has been extrapolated up to $f = 0$ Hz to obtain W_{hyst}. Finally, experimental W_{exc} is obtained by subtracting W_{hyst} from W_{diff}. Fig. 2.12 reports the total loss vs. frequency together with its components.

2.4   Modeling of loss under generic flux loci

The physical modelling of loss under 2-D flux regimes has not been yet completely achieved [40]. Nevertheless the literature show that the concept of loss separation has been extended to 2-D regimes, and some phenomenological expression for the loss have been obtained. To introduce such phenomenological models, we consider the generic elliptical flux loci of Fig 2.13, where J_p is the half-length of the major axis and $a \cdot J_p$ with $a \leq 1$ is the half length of the minor axis. Here $J_x(t) = J_p \sin(\omega t)$
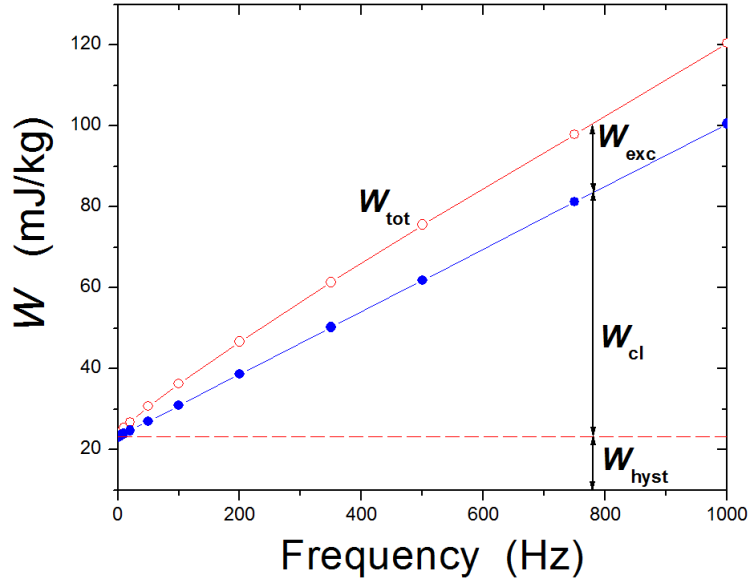
Fig. 2.12   Total loss has been separated into the hysteresis loss W_{hyst}, the classical loss W_{cl}, and the excess loss W_{exc} in a 0.35mm thick Fe-(3.2wt%)Si lamination at $B_p = 1.2$ T under 1D flux. W_{cl} is obtained by applying the standard classical formula (Eq. 2.14), W_{hyst} by extrapolating W_{diff} up to $\sqrt{f} = 0$ Hz, and W_{exc} by subtracting W_{hyst} from W_{diff}.

and $J_y(t) = aJ_p \cdot \cos(\omega t)$, where ω is the angular frequency. The application of the loss separation principle provides

$$W(J_p, a) = W_{hyst}(J_p, a) + W_{cl}(J_p, a) + W_{exc}(J_p, a). \tag{2.51}$$

A rational approach by which the different components of loss are estimated can be introduced by considering the relationship between alternating and rotational loss components. To this end, we define the ratios $R_{hyst} = W_{hyst}^{(ROT)}/W_{hyst}^{(ALT)}$, $R_{class} = W_{class}^{(ROT)}/W_{class}^{(ALT)}$, and $R_{exc} = W_{exc}^{(ROT)}/W_{exc}^{(ALT)}$. Regarding R_{class}, the theory provides, under negligible skin effect, $R_{class} = 2$. On the other end, the theoretical behavior of R_{hyst} and R_{exc} versus peak polarization is at present not completely developed. Nevertheless, phenomenological expressions for the loss components under whatever elliptical flux loci, have been worked out in [41]. Regarding the hysteresis loss, we
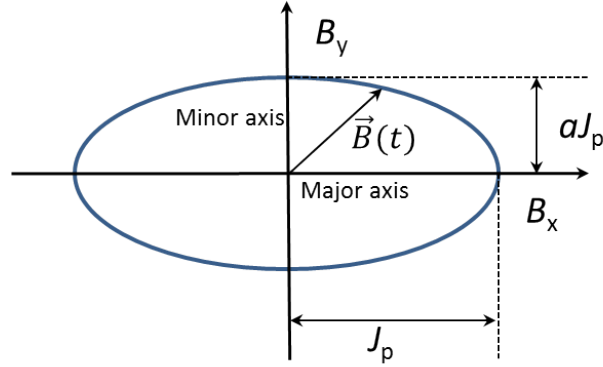
Fig. 2.13   An general elliptical flux loci, where J_p is the half-length of the major axis and aJ_p with $a \leq 1$ is the half length of the minor axis.

can interpolate the corresponding loss under alternating $W_\mathrm{hyst}^{(\mathrm{ALT})}$ and pure rotating (circular) $W_\mathrm{hyst}^{(\mathrm{ROT})}$ through the power law

$$W_\mathrm{hyst}(J_\mathrm{p},a) \cong W_\mathrm{hyst}^{(\mathrm{ALT})}(J_\mathrm{p}) \cdot (1-a^r) + W_\mathrm{hyst}^{(\mathrm{ROT})} a^r. \qquad (2.52)$$

By introducing the ratio between alternating and rotational loss components, Eq. 2.52 can be written as

$$W_\mathrm{hyst}(J_\mathrm{p},a) \cong W_\mathrm{hyst}^{(\mathrm{ALT})}(J_\mathrm{p}) \cdot \left[1 + (R_\mathrm{hyst}(J_\mathrm{p}) - 1)a^r\right]. \qquad (2.53)$$

The experiments have shown that $W_\mathrm{hyst}^{(\mathrm{ALT})}(J_\mathrm{p})$ follows a power-law similar to a^r such that $W_\mathrm{hyst}^{(\mathrm{ALT})} \propto J_\mathrm{p}^r$. Therefore we can reformulate the previous Eq. 2.53 as

$$W_\mathrm{hyst}(J_\mathrm{p},a) \cong W_\mathrm{hyst}^{(\mathrm{ALT})}(J_\mathrm{p}) + W_\mathrm{hyst}^{(\mathrm{ALT})}(aJ_\mathrm{p}) \cdot \left(R_\mathrm{hyst}(J_\mathrm{p}) - 1\right). \qquad (2.54)$$

where the ratio $R_\mathrm{hyst}(J_\mathrm{p})$ follow a rather general behavior. Regarding the excess loss, we start our analysis from the instanteneous excess power loss formula (Eq. 2.44)

under 1-D flux. The natural extension of such equation to 2D fluxes is

$$P_{\text{exc}}(t) \cong \sqrt{\sigma GSV_{\text{o}}} \left| \frac{\mathrm{d}\vec{J}}{\mathrm{d}t} \right|^{3/2}. \tag{2.55}$$

Under the elliptical flux loci shown in Fig. 2.13, the integration of Eq. 2.55 upon a period T provides

$$W_{\text{exc}}(J_{\text{p}}, a, f) = g(a) 8.76 \sqrt{\sigma GSV_0(J_{\text{p}}, a)} J_{\text{p}}^{3/2} \sqrt{f}. \tag{2.56}$$

where $g(a)$ is a non-dimensional coefficient that is given by

$$g(a) = \frac{\sqrt{2\pi}}{8.76} \int_0^{2\pi} \left(\sin^2(\phi) + a^2 \cos^2(\phi) \right)^{3/4} \mathrm{d}\phi. \tag{2.57}$$

The value of $g(a)$ ranges between 1 (alternating flux) to 1.8 (rotational or circular flux). Eq. 2.56 can be rewritten by interpolating the excess loss component measured under alternating and rotational conditions. Following this approach, we obtain

$$W_{\text{exc}}(J_{\text{p}}, a, f) = g(a) \left[W_{\text{exc}}^{(\text{ALT})}(J_{\text{p}}, f) \cdot (1 - a^q) + \frac{W_{\text{exc}}^{(\text{ROT})}(J_{\text{p}}, f)}{g(1)} a^q \right]. \tag{2.58}$$

Assuming $W_{\text{exc}}^{(\text{ALT})} \propto J_{\text{p}}^q$ and introducing the ratio $R_{\text{exc}}(J_{\text{p}})$, we eventually obtain

$$W_{\text{exc}}(J_{\text{p}}, a, f) \cong g(a) \left\{ W_{\text{exc}}^{(\text{ALT})}(J_{\text{p}}, f) + W_{\text{exc}}^{(\text{ALT})}(aJ_{\text{p}}, f) \cdot \left[\frac{R_{\text{exc}}(J_{\text{p}})}{g(1)} - 1 \right] \right\}. \tag{2.59}$$

It is worth noting that the ratio $R_{\text{exc}}(J_{\text{p}})$ can be considered independent of frequency as it will be shown later in Chapter 5. In addition, assuming $W_{\text{exc}}^{(\text{ALT})}(J_{\text{p}}, f) \propto \sqrt{f}$ we

can write

$$W_{\text{exc}}(J_{\text{p}}, a, f) \cong g(a) \left\{ W_{\text{exc}}^{(\text{ALT})}(J_{\text{p}}, f_0) + W_{\text{exc}}^{(\text{ALT})}(aJ_{\text{p}}, f_0) \cdot \left[\frac{R_{\text{exc}}(J_{\text{p}})}{g(1)} - 1 \right] \right\} \frac{\sqrt{f}}{\sqrt{f_0}},$$

$$(2.60)$$

that is the excess loss behavior under any elliptical flux loci can be obtained from the ratio $R_{\text{exc}}(J_{\text{p}})$ and the alternating excess loss at a reference frequency f_0. Regarding the classical loss, the theory provides

$$W_{\text{class}} = \frac{\sigma d^2}{12} \int_0^{1/f} \left[\left(\frac{\mathrm{d}B_{\text{x}}}{\mathrm{d}t} \right)^2 + \left(\frac{\mathrm{d}B_{\text{y}}}{\mathrm{d}t} \right)^2 \right] \mathrm{d}t, \tag{2.61}$$

In particular, for the given elliptical loci, we obtain

$$W_{\text{class}}(J_{\text{p}}, a, f) = W_{\text{class}}^{(\text{ALT})}(J_{\text{p}}, f) \cdot (1 + a^2). \tag{2.62}$$

2.5 Conclusion

The objective of this chapter was to give an overview of different iron loss models. Modelling of losss based on loss separation and STL, has been discussed. The concept of loss separation has been phenomenologicaly extended to the modeling of loss under a generic flux loci. These concepts represent the theoretical background upon which the present work is based. The next chapter will focus upon the experimental techniques.

Chapter 3

Experimental techniques

3.1 Measurement techniques

The magnetic materials have commercial value only if their magnetic properties are determined under defined AC and DC excitations. Although the amount of information provided by the manufacturers is limited by the technical difficulties and cost, there is still a growing demand of material data by engineers who need to compare different materials for optimizing their designs. It has lead to the development of comprehensive measuring methods and preparing updated measuring standards such as IEC 60404-2, IEC 60404-4, and IEC 60404-6. In this chapter we will discuss the measuring techniques and experimental setups, at low and medium frequencies, adopted by the research and industry, within the general framework provided by the international measuring standards.

3.1.1 Fieldmetric method

This method allows one to obtain the hysteresis loops, and consequently the energy loss represented by the area of the cycle, by measurement of the magnetic field

strength H and the flux density B waveforms. The flux density is obtained by means of B sensing coils, either wound across the sample, or inside holes drilled through the sample, depending upon the setup. The corresponding voltage detected by the sensing coils is then integrated to obtain B as

$$B(t) = \int \frac{1}{N_2 S} u_2(t) \mathrm{d}t, \tag{3.1}$$

where N_2 is the number of windings of the sensing coil, and S is the cross sectional area of the sample enclosed by the windings. When dealing with 2-D loss analysis, two sensing coils should be wound along the two orthogonal directions as shown in Fig. 3.1.

The magnetic field H can be obtained by two different methods. With the first method, usually applied when closed magnetic circuits are employed, the H field is obtained by measuring the magnetization current in the primary coil and is then given as

$$H = \frac{N_1}{l_\mathrm{m}} i_\mathrm{H}, \tag{3.2}$$

where N_1 is the number of turns of primary winding, i_H is the primary current, and l_m is the effective magnetic path length. With the second method, usually applied to open samples, the field H is locally measured at the surface of the sample by using H-sensor made up of thin windings wrapped around a very thin sheet as shown in Fig. 3.2. The corresponding magnetic field strength H is then obtained as

$$H = \frac{1}{\mu_0 K_\mathrm{H}} \int V_\mathrm{H} \mathrm{d}t, \tag{3.3}$$

where V_H is the terminal voltage and K_H is the coil coefficient determined via calibration of the H-coil. H-sensors employed in 2-D loss measurements have windings along the two orthogonal directions as shown in Fig. 3.2.
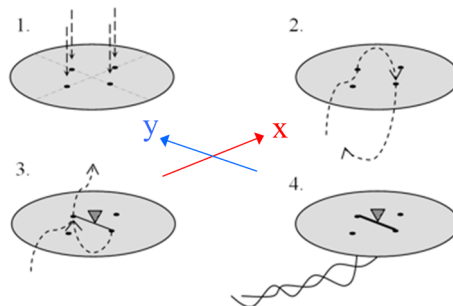
Fig. 3.1   A typical *B*-coil obtained by threading wires in holes drilled through the sample along the two orthogonal directions. Change in *B* induces voltage in these coils which is then integrated to obtain *B*.
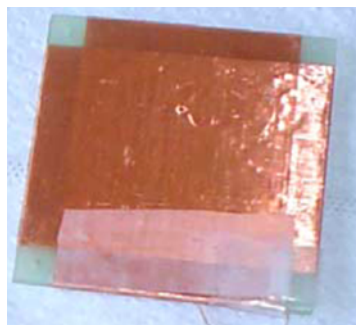
Fig. 3.2   A typical *H*-coil employed in 2D measurements with windings along the two orthogonal directions. The *H*-coil is placed very close to the surface of the sample.

The instantaneous values of B and H gives us the required information about the flux loci and the corresponding energy loss in the sample. The total specific loss occurring in the sample, in case of 1-D supply conditions is given by

$$P_t = \frac{1}{T\rho_m} \int_0^T (H_a \cdot \frac{dB}{dt}) dt. \qquad \text{(J/kg)} \qquad (3.4)$$

where T is the period and ρ_m is the mass density of the sample.

In 2-D loss analysis, the corresponding total power loss is obtained by

$$P_t = \frac{1}{T\rho_m} \int_0^T (H_x \cdot \frac{dB_x}{dt} + H_y \cdot \frac{dB_y}{dt}) dt, \qquad \text{(J/kg)} \qquad (3.5)$$

where B_x, B_y, H_x and H_y are the components of flux density and magnetic field strength along the two orthogonal directions x and y.

3.1.2 Thermometric method

The fieldmetric method becomes inaccurate at high induction because of the very low power factor. As an example, in non-oriented alloys, the fieldmetric method fails to perform accurate measurements at induction greater than $B_p \sim 1.6$ T. Beyond this threshold, an alternative technique for loss measurement, called thermometric method, able to operate under whatever flux loci, comes into play. Fig. 3.3 shows an example of the energy loss behavior vs. peak induction at different frequencies under rotational flux. It can be seen that the loss obtained using the fieldmetric method deviates from thermometric loss measurements beyond 1.6 T and is affected by a large increasing uncertainty.

The thermometric method measure the loss by exploiting the dependence between the rate of rise of temperature of the sample dT/dt and the dissipated power [42]. The temperature of the sample can be measured by an extended copper-constantan thermocouple (TC), attached to the measuring area of the sample via a conducting
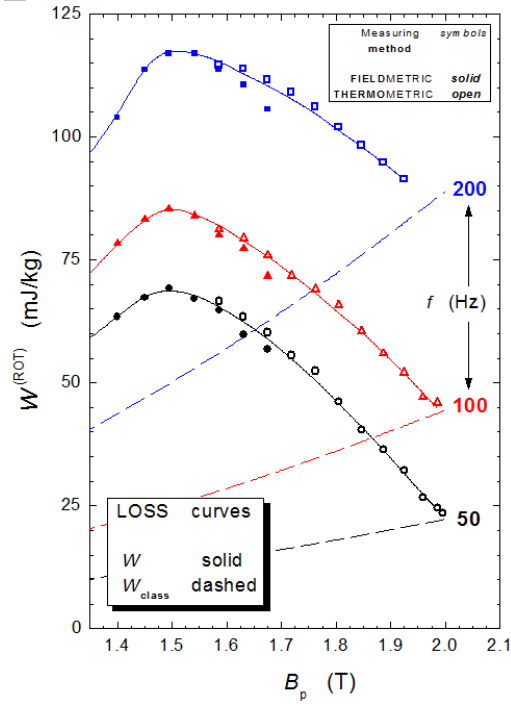
Fig. 3.3   Energy loss vs. peak induction measured under circular flux at 50 Hz, 100 Hz and 200 Hz. At low induction, measurements have been carried out using fieldmetric method (solid symbols). At high inductions i.e. beyond 1.55T, the fieldmetric measurements could not represent the true loss value due to the very low power factor, therefore, the loss measurements have been performed via the thermometric method (open symbols).

glue (normally a silver paste) as shown in Fig. 3.4. An identical copper-constantan junction, insulated from the sample, is connected in series opposition with the active junction of TC. The output differential signal is then fed into a nanovoltmeter. The sample is placed in a vacuum chamber where quasi-adiabatic conditions are achieved.

Under stationary regime the dynamic energy balance (see Fig 3.6) is described by the following equation

$$P = \frac{\mathrm{d}Q}{\mathrm{d}t} + \frac{\mathrm{d}Q_{\mathrm{int}}}{\mathrm{d}t} + \frac{\mathrm{d}Q_{\mathrm{ext}}}{\mathrm{d}t}, \qquad (3.6)$$

where $\mathrm{d}Q/\mathrm{d}t$ is the rate of cumulation of thermal energy in the sample, $\mathrm{d}Q_{\mathrm{ext}}/\mathrm{d}t$ is the rate of heat transmission to external reservoir (environment) at temperature T_{o}
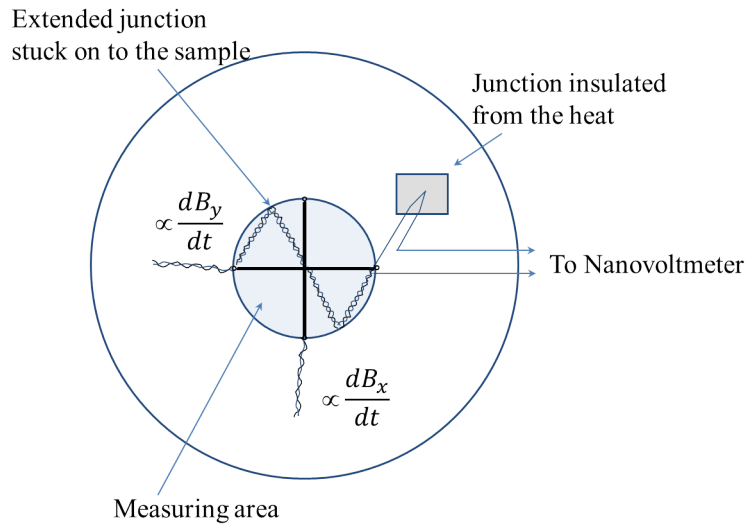
Fig. 3.4   Copper-constantan junctions used to detect temperature variations and perform thermometric loss measurements. The two orthognal black lines in the center represent B-windings threaded into the holes drilled through the sample. An identical copper-constantan junction, insulated from the sample, is connected in series opposition with the active junction of thermocouple.
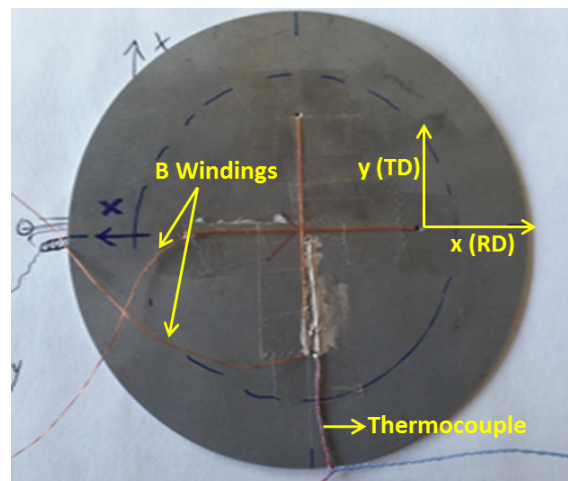
Fig. 3.5   A sample with two orthogonal B windings threaded in holes drilled through the sample. A thermocouple is also attached to the sample by using a conductive glue.
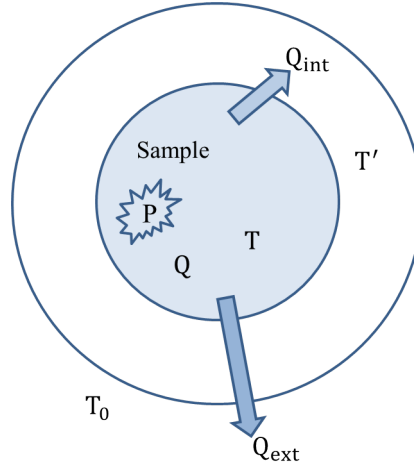
Fig. 3.6   Scheme of the heat transfer processes inside the disk. T is the temperature of the measuring area (dark inner region). Q_{int} is the heat transferred to the disk at temperature T' while Q_{ext} is the heat transferred to the external environment at a temperature T_o.

and dQ_{int}/dt is the rate of heat transmission to the part of the disk, at temperature T', sorrounding the measuring (central) region, P is the dissipated power as a consequence of the magnetization process. The first term of the right hand side of Eq. 3.6 is given by

$$\frac{dQ}{dt} = c_p \frac{dT(t)}{dt}, \tag{3.7}$$

where T is the temperature of the measuring area of the sample and c_p is the specific heat per unit mass of material. The second term of Eq. 3.6 is given by

$$\frac{dQ_{int}}{dt} = K_{int}[T(t) - T'(t)], \tag{3.8}$$

being K_{int} the internal heat transmission coefficient. Finally, the last term of Eq. 3.6 is given by

$$\frac{dQ_{ext}}{dt} = K_{ext}[T(t) - T_o], \tag{3.9}$$
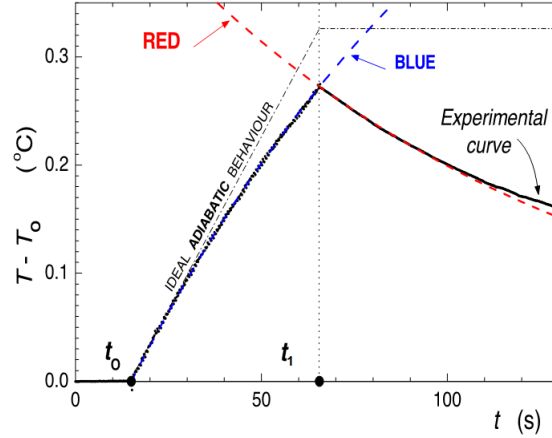
Fig. 3.7   Experimental increase of T vs. time represented by black solid curves for a non-oriented Fe-(3.2wt%)Si-(0.5wt%)Al lamination at $B_p = 1.7$ T and $f = 50$ Hz. The blue dashed line is obtained by applying Eq. 3.13 while the red dashed line is obtained via Eq. 3.14. It can be seen that the experimental curves can be excellently predicted by this technique.

where K_{ext} is the external heat transmission coefficient. From Eq. 3.7, 3.8 and 3.9, Eq. 3.6 takes the following form

$$P = c_p \frac{dT(t)}{dt} + K_{int}[T(t) - T'(t)] + K_{ext}[T(t) - T_o]. \qquad (3.10)$$

In our analysis we have assumed that the temperature of the sample is uniform. Therefore $T(t) = T'(t)$ and equation 3.10 reduces to

$$P = c_p \frac{dT(t)}{dt} + K_{ext}[T(t) - T_o] \qquad (3.11)$$

 Before starting the experiment, the sample must be in thermal equilibrium with its surroundings. The experiment starts at the *switch on* time t_0, and stops at the *switch off* time t_1, at which the sample has reached temperature T_1.

Under perfect adiabatic conditions, the external heat transmission coefficient K_{ext} is zero and Eq. 3.11 further reduces to

$$P = c_{\mathrm{p}} \frac{\mathrm{d}T(t)}{\mathrm{d}t} = c_{\mathrm{p}} \frac{(T_1 - T_{\mathrm{o}})}{(t_1 - t_0)}. \tag{3.12}$$

However, in reality, K_{ext} is not zero and has to be determined experimentally. If Eq. 3.11 is integrated from the *switch off* time t_1, the exponential decay of temperature is obtained as

$$T(t) = T_{\mathrm{o}} + (T_1' - T_{\mathrm{o}})\exp\left[-\frac{K_{\mathrm{ext}}}{c_{\mathrm{p}}}(t - t_1) \right]. \tag{3.13}$$

The only unknown in this equation is K_{ext} which can easily be determined via a fitting procedure (for $t > t_1$), as shown in figure 3.7. Eventually the increase of temperature of the sample between t_0 and t_1 is given by the following equation

$$T(t) = T_{\mathrm{o}} + \frac{P}{K_{\mathrm{ext}}}\left[1 - \exp\left(-\frac{K_{\mathrm{ext}}}{c_{\mathrm{p}}}(t - t_0) \right) \right]. \tag{3.14}$$

The last expression can provide the dissipated power loss P. Again, as shown in Fig. 3.7, a good fit of the temperature behavior is also possible in this region with consequent achievement of P. This method was used extensively to measure the localized power loss in [43, 44]. Part of the experiments described in Chapter 5 are obtained by using the thermometric method.

3.2   Measurement setups

3.2.1   1-D Measurement setup

In this section we will describe the wattmeter-hysteresisgraph used to perform 1-D loss measurements. Magnetizers such as Epstein frame, Single Sheet Testers and Ring samples can be employed within the setup. A scheme of the hysteresisgraph is given in Fig. 3.8. The waveform is supplied by a signal generator to a power amplifier and is used to drive the primary coil of the magnetizer. The voltage drop u_H is measured on a calibrated resistor R_H so obtaining the magnetizing current $i_H = u_H / R_H$. The corresponding magnetic field strength is then obtained as

$$H = \frac{1}{G_H} \frac{N_1}{l_m} i_H(t), \tag{3.15}$$

where G_H is the low-noise pre-amplifier gain, N_1 is the number of windings of the primary coil, and l_m is the magnetic path length which depends upon the type of magnetizer. On the other end, the voltage u_2 induced in the secondary coil of the magnetizer is amplified by a low-noise preamplifier, and then fed into the digital oscilloscope. The induced voltage is integrated to obtain B as

$$B(t) = \int \frac{1}{G_B} \frac{1}{N_2 S} u_2(t) \mathrm{d}t, \tag{3.16}$$

where G_B is the gain of the preamplifier, N_2 is the number of windings of the secondary coil and S is the cross sectional area of the sample. Two channel digital oscilloscope capable of performing synchronous acquisitions should be used to perform simultaneous acquisiton of both signals. The signals are then elaborated by a software in PC, where the energy loss is obtained as

$$W = \frac{1}{G_B S N_2} \int_0^T u_2 \cdot i_H \mathrm{d}t. \qquad (\mathrm{J/m^3}) \tag{3.17}$$
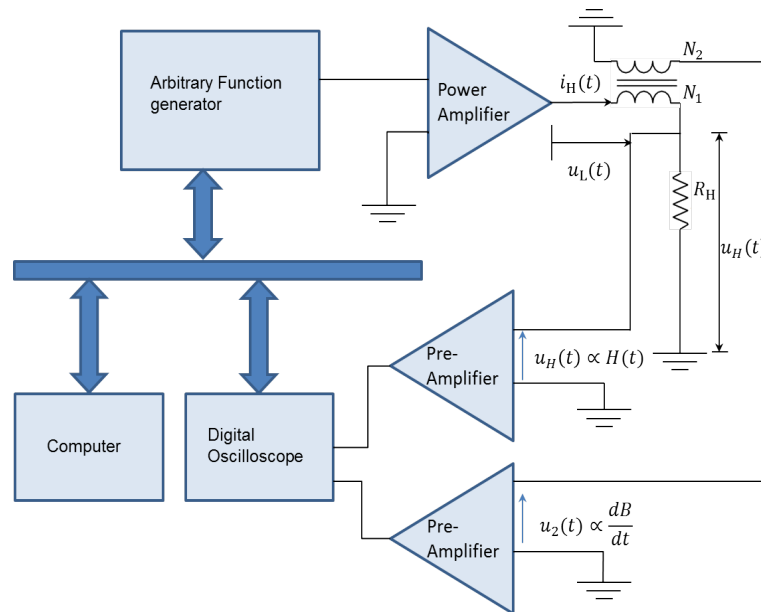
Fig. 3.8   The wattmeter-hysteresisgraph developed by Fiorillo and co-workers [45] at INRIM. The system implements digital control of the waveform of dB/dt by an iterative process. Samples such as Epstein strips, and ring samples can be employed in the system.

A sinusoidal dJ/dt is recommended by the standards for AC characterization. It is controlled by using the iterative procedure discussed in section 3.2.3. Let us now discuss different magnetizers that can be employed in the setup.

Epstein Frame

The standard Epstein frame, recommended by IEC 60404-2 [8], consists of four rectangular solenoids into which the strips can be inserted in such a way as to form a closed magnetic circuit. The frame can either have 200 turns or 700 turns of primary and secondary windings. The primary winding is used to magnetize the specimen and is located on the outside of each limb. A secondary winding, located on the inner side of each limb, is used for the detection of voltage. Samples are cut along the transverse and rolling directions and loaded in the opposite sides of the frame. The samples form double lapped joints and there are overlapping corners in the circuit.
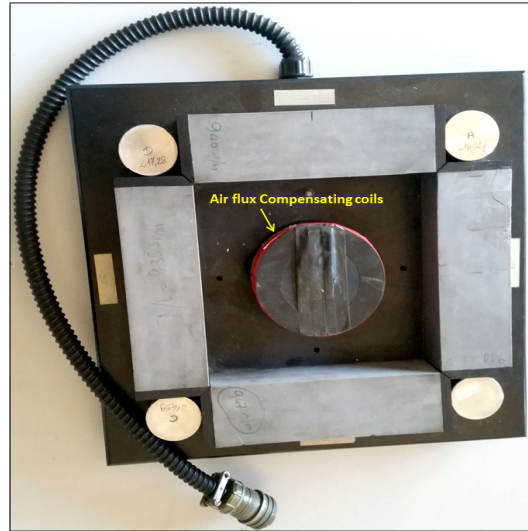
Fig. 3.9   A 700 turns compensated Epstein frame. The standard weights are placed at each corner. The samples cut along the transverse and rolling directions should be loaded into the opposite limbs.

In order to measure the loss, we exploit Eq. 3.4 where the field H is obtained by

$$H = \frac{N_1}{l_m} i_H,$$

$$(3.18)$$

being N_1 the number of turns of primary winding, i_H is the primary current, and l_m is the effective magnetic path length whose value is recommended to be 0.94 m [46].

There are some problems associated with the Epstein frame in terms of determining the true loss behavior of magnetic materials. In fact, the double lapped joints and overlapping corners introduce inhomogenities in the circuit. Then, the effective magnetic path length is not always fixed and such assumption introduces systematic errors in the experiments. The sample preparation procedure includes stress relief annealing which can be time consuming. Irrespective of these problems, it is used extensively in the industry because of its reproducibility and standardization. Fig. 3.9 shows a 700 turns Epstein frame with an air flux compensation, where the primary winding of the air flux compensator is connected with the primary winding of Epstein frame, while the secondary windings are connected in series opposition. The number
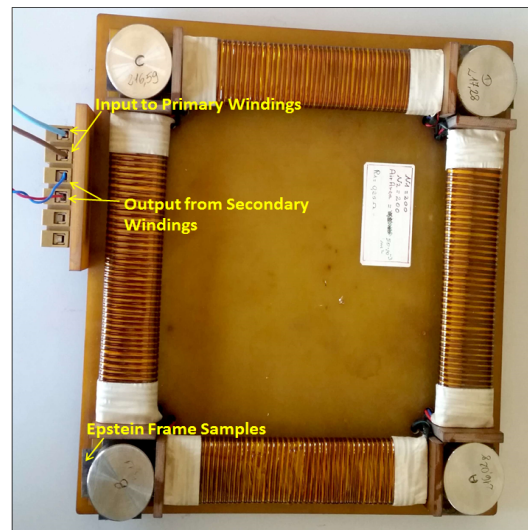
Fig. 3.10   A 200 turns non-compensated Epstein Frame loaded with sample and standard weights on each corner. The primary windings are located on the outside of each limb while secondary winding are located on the inside. This Epstein frame is recommended for frequencies up to 10 kHz.

of turns in the compensator is then veried in such a way that it produces a voltage equal but opposite to the voltage produced by the Epstein Frame with no sample. In this way, the air flux is compensated for almost all of the current levels. A 200 turn Epstein frame is shown in Fig. 3.10. The use of any of the frame depends upon the input frequency.

Ring core measurements

Ring samples, e.g. as in Fig. 3.11, are recommended by IEC 60404-6 and can be employed to perform loss measurements of magnetic materials with high permeabilities, soft magnetic composite powders and non-oriented steel sheets. The ring samples have a fixed circumferential magnetic path length, no airgaps and can be mounted directly without any addtional setup. However, materials can undergo through bending stress, and magnetic properties become dependent upon the radius of the ring sample.
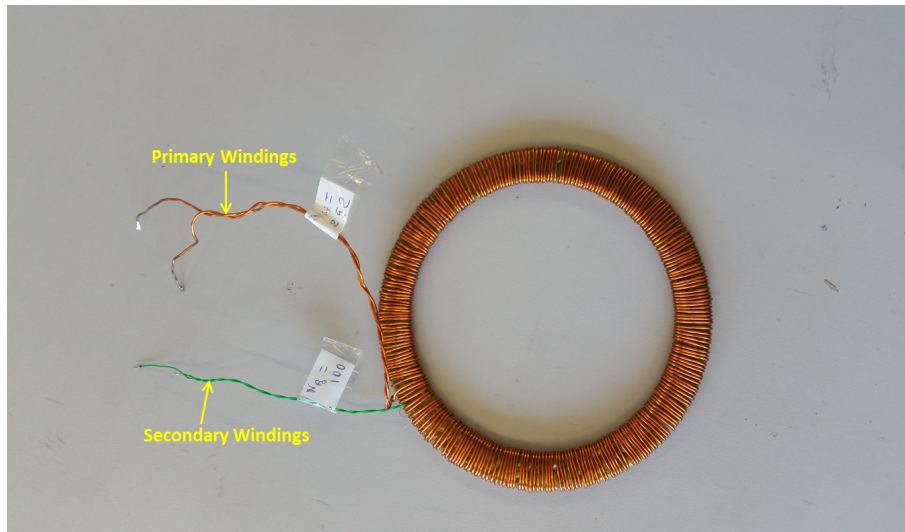
Fig. 3.11   A low Carbon Steel ring sample with the number of primary and secondary windings of 252 and 100 respectively.

Two layers of windings are wrapped around the sample. The outer one is the primary winding used to create the field in the sample while the inner winding is used to determine the secondary voltage. The magnetic field is obtained through

$$H = \frac{N_1 i_\mathrm{H}}{2\pi r_\mathrm{m}}, \qquad (3.19)$$

where r_m is the mean radius of the ring, N_1 is the number of primary windings and i_H is the excitation current. Finally, the loss is determined by applying Eq. 3.4. In order to get good uniformity of magnetization over the ring cross-section, it is recommended in IEC 60404-6 that the ratio between the outside and inside diameters be $D_\mathrm{o}/D_\mathrm{i} \leq 1.1$.

Single Sheet Tester measurements

Energy loss in different magnetic materials can also be determined by the application of Single Sheet Testers (SST). Fig. 3.12 shows a SST recommended by IEC 60404-3, used in industrial measurements. Samples of 500 mm long and between 300-500

mm are used. The yoke of the SST is laminated and can be constructed either from grain oriented Fe-Si or Ni-Fe laminations, by U-bending and stacking them upon one another. Double C-yokes are usually made of grain oriented Fe-Si laminations and should be 25 mm thick and within 0.5 mm coplanar to eliminate the air gaps between opposite poles. Minimum recommended length for primary and secondary windings are 440 mm [47]. The upper C-yoke is made to move in the upward direction to allow insertion of the sample. Moreover, the weight of the upper C-yoke is counterbalanced by a suspension in such a way that a maximum force of 200 N is applied on the sheet. The magnetic path length is fixed at 0.45 m. Although H fields could be measured either by using Hall probe, a flat H-sensing coil, or a Rogowski-Chattock potentiometer, the standard IEC 60404-3 prescribe to obtain H from the current circulating in the primary winding [47]. The field is then

$$H = \frac{N_1 i_H}{l_m},\tag{3.20}$$

where N_1 is the number of turns of the excitation coil, i_H is the excitation current and l_m is the effective length of magnetic circuit. The arrangement must be placed in the east-west direction to mitigate the effect of earth magnetic field upon the measurements.

Sources of systemetic errors in SST are the assumption of a fixed magnetic path length, and the loss in the yoke which were compensated by using additional magnetizing windings, a Rogowski-Chattock potentiometer and a feedback circuit in [49, 50]. This lead to an expansion towards Compensated Single sheet/strip tester (CSST). However, the designed circuit, arrangement of coils, and stability of the structure of potentiometer, prevented it from considering it as a measurement standard. Nafalski and Moses [51] designed a double yoke system with low specific loss and reduced the length of Rogowski-Chattock potentiometer coil to half of the magnetization windings. Despite of the design improvements, the system still had
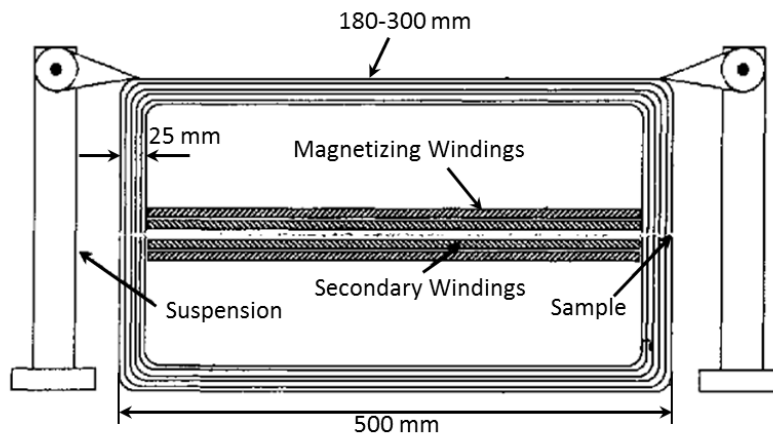
Fig. 3.12   Single Sheet Tester recommended by IEC 60404-3 adapted from [48]. The pole face is 25mm thick. The primary and secondary windings should be at least 440mm long. The primary windin can be a single layer, made of 1mm diameter wire with 400turns. The number of secondary windings is not fixed, and is suited to accurate signal acquisition.

considerable loss in the yoke of the system. To compensate the losses in the yoke of SST precisely, a simple and effective compensation technique has been proposed and a single strip double-C yoke permeameter has been developed. It is discussed in chapter 4.

Medium to high frequency measurements

Although, the focus of thesis is upon low and power frequencies, medium to high frequency measurements will be discussed in this section briefly, to get a basic idea about the problems that come into play if the input magnetization frequency is increased beyond few kHz. Characterization of soft magnetic materials in the kHz range and beyond is required due to the increasing use of motors and transformers at high frequencies. Some of the problems encountered in high frequency measurements are as follows:

• Skin effect: The counter field generated by the eddy currents can lead to non-uniform penetration of flux in the sample under investigation. Skin effect can also affect the conductors and even the calibrated resistor used to measure the magnetizing current. This can significantly influence the output result.

• Increasing frequency can drastically increase the temperature of the sample. As an example, a Mn-Zn ferrite ring sample can show an increase of the temperature of 2 °C per second when it is excited at 1MHz at $J_p = 0.1$T.

• For the detection of signals, rapid A/D converters are required. The power requirements of the system also increases significantly. As such, the peak induction that can be achieved in the sample becomes limited. In case of single sheet measurements, the materials used in the yoke for flux closure should be such as to exhibit minimum skin effect.

• Stray inductances and capacitances start to play a very important role when the magnetizing frequency exceeds the kilohertz range. The leakage flux can be neglected as compared to the flux produced by the sample. However, effects related to parasitic capacitance cannot be ignored. With the increase of frequency, increased current is drained due to the winding capacitance in connecting cables and at the input of acquisition devices. Self capacitance in the range of 50 pF/m to 100 pF/m can be found in coaxial cables while 10 pF to 50 pF is common in acquisition devices.

Self capacitance of the primary and secondary windings of 700 turns epstein frame is between 50 pF and 200 pF while interwinding capacitance is in the order of 1000 pF to 3000 pF which is huge. IEC 60404-10 therefore recommends the use of 200 turn Epstein frame beyond 400 Hz, which can appropriately be used till 10 kHz.

Numerous methods of incorporating the effects of inductances and capacitances in the circuit are discussed in [48]. The discussion of these techniques are beyond the scope of this thesis, as here all the measurements are performed in conditions where the effects of inductances and capacitances due to the circuit can be neglected. In case of analysis at frequencies beyond 400 Hz, a 200 turn Epstein frame has been used, as recommended by IEC 60404-10. Also, at high frequencies and low induction, the material can be treated as a linear medium which brings acceptable simplification in the analytical treatment of power loss at high frequencies. It is advised to consult Chapter 6 for further details regarding magnetic behavior of soft magnets at high frequencies and low inductions.

3.2.2   2-D measurement setups

In this section, magnetic measurements systems under 2D (rotational or elliptical) flux are discussed. In particular, the scheme of our experimental setup, developed at INRiM, is shown in Fig. 3.13 and 3.14 for the fieldmetric and thermometric methods, respectively. Previous work have been carried out on grain oriented materials and is reported in [52–54]. Loss analysis in different non-oriented steel sheets under 2D flux has been perfomed in [41, 55]. An intercomparison of rotational loss measurements in non-oriented Fe-Si alloys has been performed in [56], while comprehensive investigation of alternating and rotational losses in non-oriented steel sheets has been carried out in [44]. Disk shaped samples has been analyzed by C. Ragusa and co-workers under 2D flux up to high inductions in [16, 18].
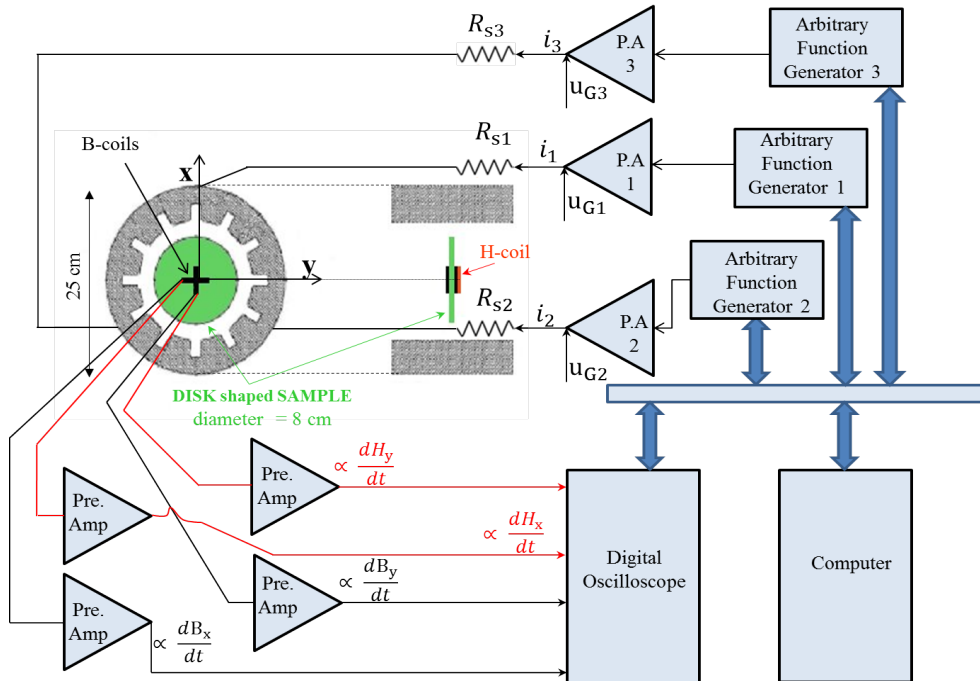
Fig. 3.13 Experimental setup for the loss measurement of soft magnetic materials under controlled 2D flux loci via fieldmetric method. The arbitrary function generators provide a suitable voltage to the three phase magnetizer via power amplifiers to achieve the desired flux loci. Two orthogonal windings are threaded along *x* and *y* directions to detect *B* while *H* is obtained by using a 700 turn flat *H*-coil. The signals *B* and *H* are amplied using a preamplifier, converted to digital form using an oscilloscope and then elaborated by a software in PC. The 2D energy loss is obtained by adding the areas of the loops along the two orthognal axis.

In our setup, disk shaped sample having 80 mm diameter are employed. The desired flux density is obtained through a three-phase magnetizer by supplying the exciting coils through suitable currents fed by the power amplifiers that are driven by the arbitrary function generators. Suitable waveform for the generator can be obtained through a feedback system that eventually achieve the flux loci and waveform. The signals detected by the search coils are amplified, read by digital oscilloscope and elaborated by a PC.
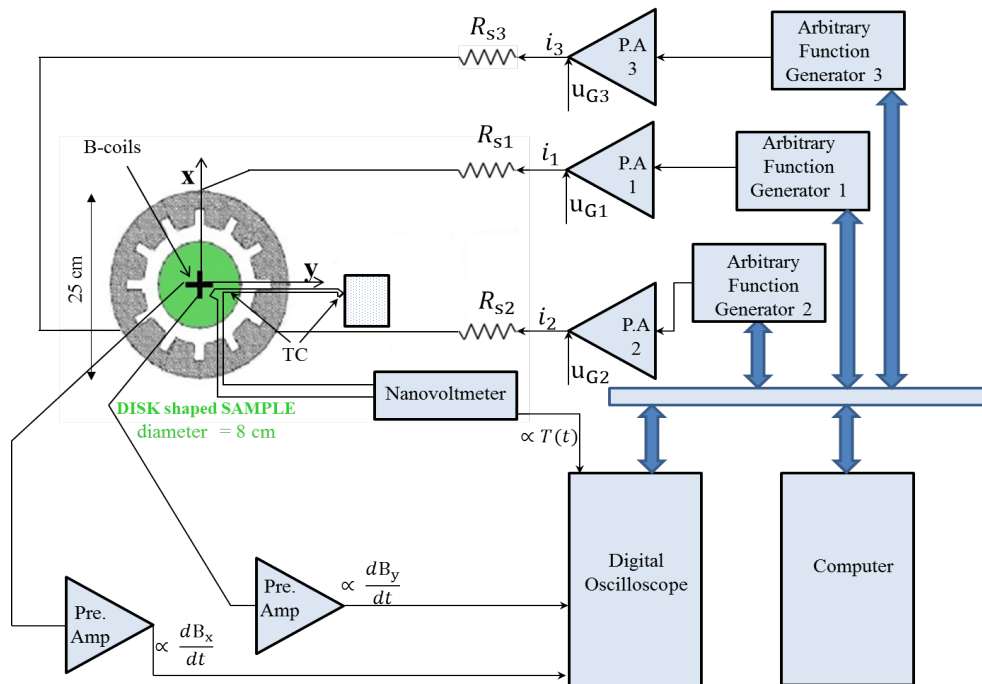
Fig. 3.14 Experimental setup for the characterization of soft magnetic materials under controlled 2D flux loci via thermometric method. Here the rate of the rise of the temperature of the sample is detected by using thermocouples along the *x* and *y* direction which are stuck on the surface of the lamination using a conductive glue (normally silver paste). The thermocouples are connected in series opposition with a junction insulated from the sample to compensate any fluctuations. The thermocouples are connected to a digital oscilloscope through a nano-voltmeter. The application of thermometric method requires adiabatic conditions. To this purpose, the bore of the magnetizer was designed to accomodate a cylindrical Plexiglas vacuum chamber. The desired flux loci is obtained through arbitray function generators that supply suitable currents to the magnetizer via power power amplifiers. The energy loss along each axis is obtained by applying Eq. 3.13 and 3.14.
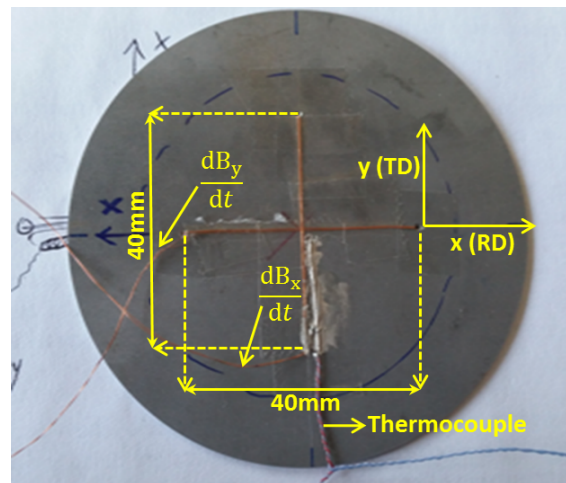
Fig. 3.15   Sample with two orthogonal B windings threaded along the holes (diameter=0.7mm) spaced 40 mm apart.

B and H-coil

To measure magnetic field B, holes of 0.7mm diameter are drilled through the sample along the x and y axes. Fig. 3.15 shows the two orthognal windings, each having a few turns, threaded into the holes to detect the corresponding voltages.
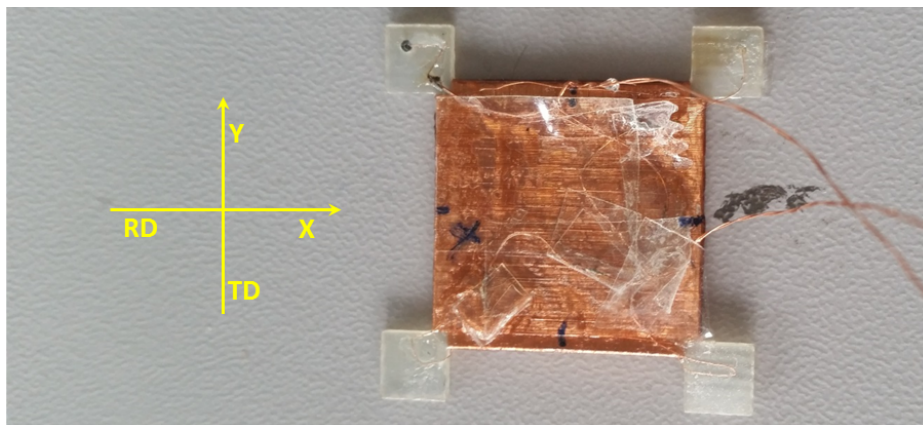
Fig. 3.16   A 700-turn H-coil with two orthogonal windings along rolling and transverse directions. The coil is made of very thin wire and wrapped around a thin sheet. It should be placed as close to the surface of the sample as possible.

To measure the effective field, the H-coil exploits the property of conservation of the tangential component of the field at the sample's surface [57]. Fig. 3.16
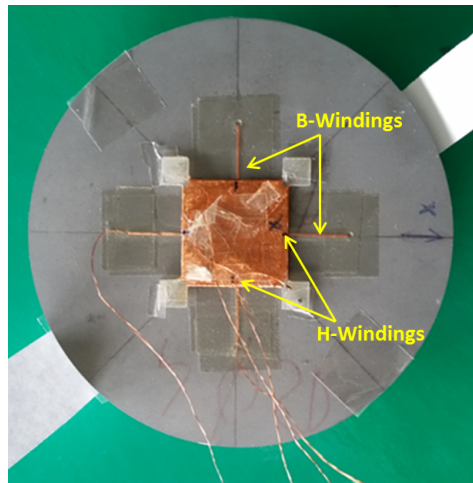
Fig. 3.17   *B*-Windings threaded through the sample through holes drilled in the sample. These windings are placed orthogonal to each other to measure the field in x and y directions. *H*-sensor is placed very close to the surface to measure *H* at its surface with double windings along x and y direction.

shows a vectorial 700-turn flat *H*-coil with two windings along the *x* and *y* axis, which is placed at the center of the sample (Fig. 3.17). To reduce the errors, the *H*-coil is made of very thin windings, wrapped around a very thin sheet, and is placed very close to the surface of the sample. After integration of the voltages, the tangential field components H_x and H_y of the field $\overrightarrow{H}$ are obtained. The *H*-coil is positioned in such a way that the direction of H_x and H_y should coincide with B_x and B_y respectively. Small misalignment are compensated by performing measurements along clockwise and anticlockwise direction and then taking their averaged value [58].

Magnetizers

Two different kinds of three phase magnetizers have been applied. The first magnetizer designed to perform high frequency measurements up to 5 kHz [59] is shown in Fig. 3.18. A small air gap width of 1 mm between the sample and the yoke has been adopted to reduce the demagnetizing field and the magnetizing currents in each phase. The magnetizer has two-pole stator core, with three slots per pole, and a
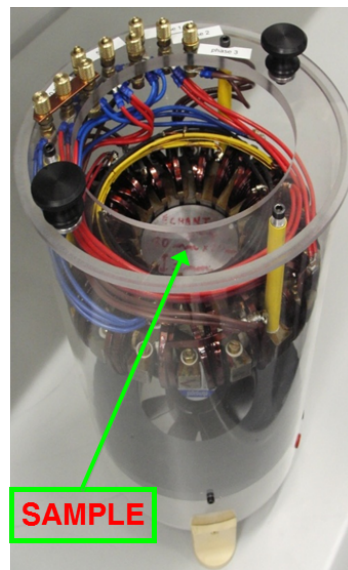
Fig. 3.18   The high frequency low induction magnetizer with sample placed in its center

toroidal winding configuration as shown in Fig. 3.19. The core was assembled by using 0.35 mm thick non-oriented Fe-Si sheets.

The second magnetizer was designed for the thermomtric and high induction loss characterization. It is shown in Fig. 3.20. To excite the sample at high peak inductions, the windings are made of thin copper wires as the number of turns per coil is large as compared to the first magnetizer. Moreover, to get adiabatic conditions, the bore of the magnetizer was designed to accomodate a cylindrical Plexiglas vacuum chamber, shown in Fig. 3.21. In the vacuum chamber, a residual pressure of around 10^{-3} Pascals was reached by using a vacuum pump.
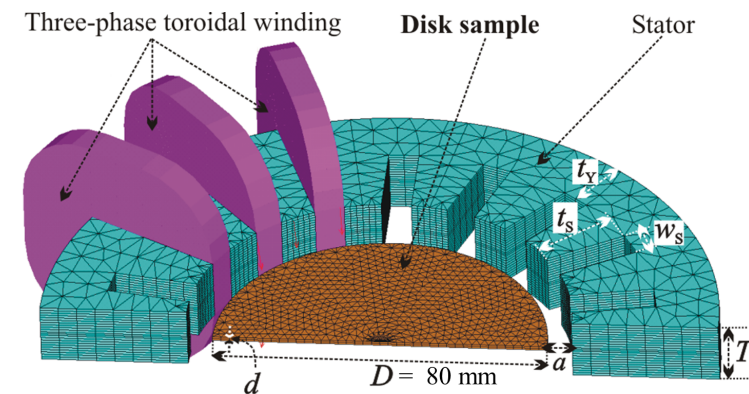
Fig. 3.19 The magnetizer has two-pole stator core, with three slots per pole, and a toroidal winding configuration. Geometric parameters slot depth t_s, core-thickness t_y, axial height of core T and width of slot w_s were optimized to excite the 80mm disk shaped sample at high frequencies. The coils in the magnetizer are made up of thick copper wires and the number of turns per coil is limited to 10. Moreover, there is a mid-point connection on each coil by which number of turns per coil n_s can be changed to 5 to perform high frequency measurements
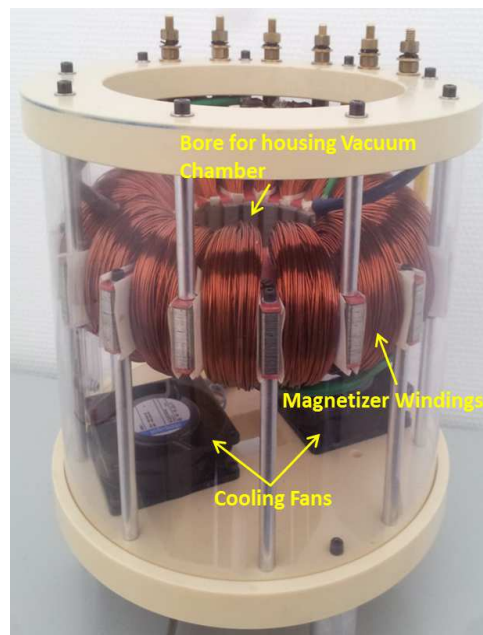
Fig. 3.20 High induction magnetizer designed to perform analysis at high inductions close to saturation conditions. The bore of the magnetizer can accommodate a cylindrical plexiglas vacuum chamber to achieve adiabadic conditions.
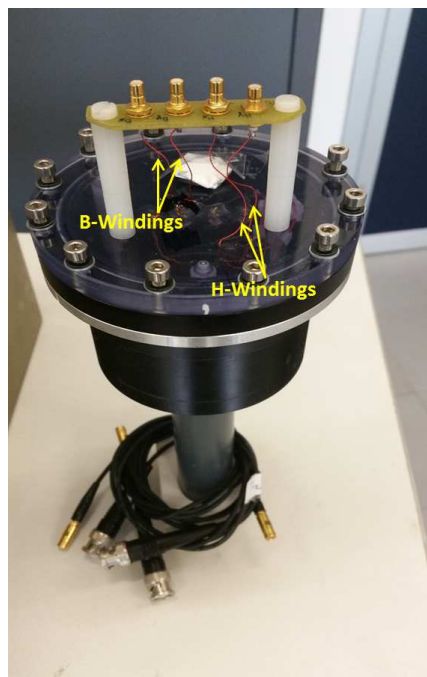
Fig. 3.21   Cylindrical Plexiglas vacuum chamber enhousing the sample to obtain quasiadi-abatic conditions required for analysis via thermometric method.

3.2.3   Control of the induction waveform

The measuring standards prescribe that the AC characterization of magnetic materials should be carried out under a controlled sinusoidal waveforms. With the development of electronic setups, the sinusoidal induction waveforms can be maintained even in small samples using a negative feedback. Here the actual voltage on the secondary side is compared with the reference voltage supplied to the primary circuit. The difference is amplified and reinjected in to the primary till it reduces to zero. Digital feedbacks are preferred because of the stability and bandwith limitations in analog feedbacks.

   The block diagram of the feedback algorithm used in the measurement setups is shown in Fig. 3.22 adapted from [60]. The whole system can be considered as a voltage/flux, input/output nonlinear dynamical system with the voltage u as the main physical output. The desired waveform is obtained by controlling the function generator through an iterative procedure in which the next voltage is obtained by the addition of the term linearly dependent upon the difference between the desired and actual flux. It is given by

$$e^{k+1} = e^k + \alpha(\phi_\mathrm{p} - \phi^k) + \beta(u_\mathrm{p} - u^k) \qquad (3.21)$$

where e^{k+1} is the input voltage obtained upon $k+1$- iteration, e^k is the input voltage obtained upon the k-th iteration, ϕ_p is the prescribed flux, ϕ^k is the actual flux measured upon the k-th iteration, u_p is the prescribed voltage while u^k is the voltage measured upon the k-th iteration, α is a system dependent suitable positive constant and β is a dimensionless quantity. The feedback can also be implemented in such as way that it acts either on the flux or the voltage. In case of 2-D flux loci, the applied fields are controlled by three programmable function generators via a similar iterative procedure to ensure the correct flow of three phase currents into the windings of magnetizer, through power amplifiers and resistances connected in series.
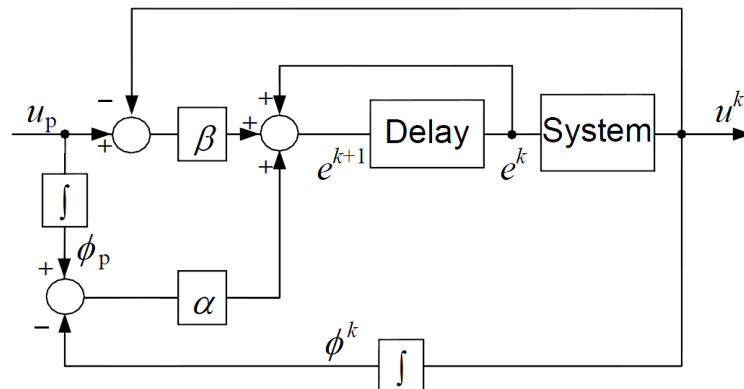
Fig. 3.22   Block diagram of the feedback algorithm (adapted from [60]). The system can be considered as a voltage/flux, input/output nonlinear dynamical system in which a numerical feedback periodically refreshes the voltage input so that the actual voltage gets a better match of the prescribed periodic output.

Chapter 4

A novel compensated Single Strip Tester

4.1   Introduction and motivation

Power loss measurement in different materials has always been a subject of interest for many years. The goal of the measurement setups is to determine the magnetic losses as a function of induction and frequency accurately. Moreover, the results should be repeatable and reproducible. Various standards have been devised to achieve this goal. Burgwin suggested Epstein Frame and it has been used as a standard (IEC 60404-2) for loss measurements. However, the method requires tedious preparation of samples and results in the systematic deviations due to inhomogeneities in the magnetic circuit. [61, 62, 48]. Single sheet tester is also widely used to measure the magnetic loss properties of magnetic materials and has been standardized by IEC 60404-3. SST shows good reproducibility but the assumption of fixed magnetic path length and losses in the yoke introduce systematic errors in loss measurements. To address these issues, a single strip double-C yoke permeameter with a simple, effective and a novel compensation technique has been implemented

to compensate losses in the yoke of SST, thereby reducing systematic errors in loss measurements. The system uses Epstein strips because they are practically convenient. However, it can be easily adapted to the standard SST permeameter. The idea is to use the upper half yoke of the permeameter as a zero MMF indicator and the lower half of the yoke for the implementation of compensation circuit.

4.1.1 Sample geometry
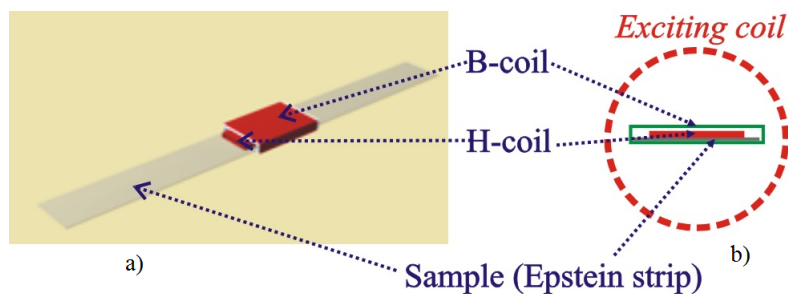
Fig. 4.1   a) Epstein Strip used as a sample in the compensated single strip tester; b) cross-sectional view of the strip sample and coils.

Fig. 4.1 shows the sample used in the permeameter. As previously stated, it is a conventional Epstein strip. A 500 turn and 30 mm long B-coil is placed across the center of the sample. A calibrated multi-turn flat H-coil, having a thickness of 1 mm and 0.0225 m^2 turn-area, is placed inside the B-coil over the surface of the sample to measure the tangential field. The effective fields and inductions are found to be highly uniform across the measuring region. The obtained loss is therefore, the true loss of the material. The results obtained by using B and H-coils will be used as a reference. The designed permeameter is shown in Fig. 4.2. It consists of a double-C laminated yoke, each yoke is in turn composed of 0.30 mm thick high-permeability grain-oriented strips with cross sectional area of 2500 mm^2. There is a distance of $L_1 = 190$ mm between the pole faces of the yokes. A uniformly wound solenoid is placed within the pole faces. Supplementary thin windings are placed at the end
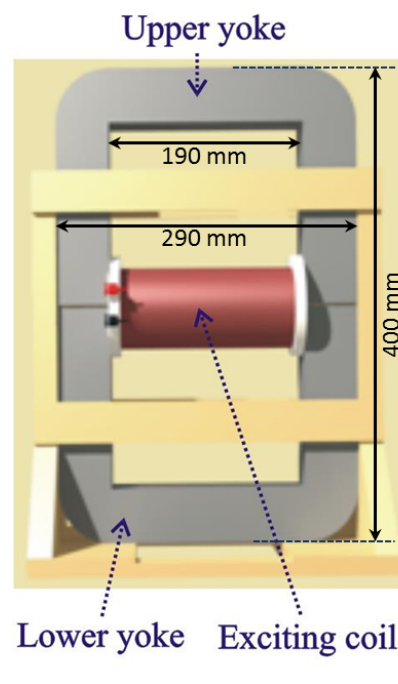
Fig. 4.2   A 3-D view of the designed permeameter. Middle part contains the sample and is enclosed by exciting coils.

of the solenoid to obtain maximum uniformity of the applied field over the whole length [48].

4.1.2   Magnetic path length

As discussed in 3.2.1, the magneto motive force *NI*, where *I* is the current flowing through *N* number of windings is related to magnetic field *H* along the closed path can be obtained by using Ampere's law and is given as

$$N \cdot I = \oint_{L} H \cdot dl = H \cdot L_{s} + H \cdot L_{p} \tag{4.1}$$

where $(H \cdot L_{p})$ represents the MMF drop in the yokes and $(H \cdot L_{s})$ represents the MMF drop in the sample. If somehow the MMF drop in the yokes is made very
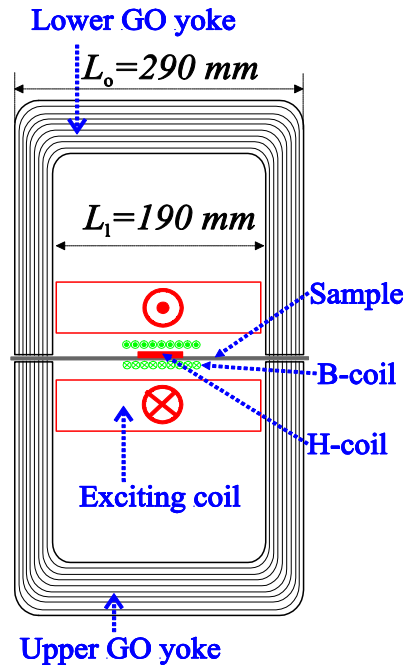
Fig. 4.3   A 2-D view of magnetizer, measuring coils and exciting current

close to zero or compensated precisely, the Eq. 4.1 will reduce to

$$N \cdot I = H \cdot L_{\mathrm{s}} \tag{4.2}$$

where L_{s} has a value intermediate between L_1 and L_{o}. L_1 is the distance between the pole faces and L_{o} is the total width of the permeameter (see Fig. 4.3). The value of L_{s} apparently depends upon flux channeling into the yoke from sample as shown in Fig. 4.4. It also depends upon the magnetization levels in the sample and changes considerably when the sample enters into the non-linear regime.

In order to get the accurate prediction of the field generated in the sample, the length of the flux L_{s} needs to become equal or close to the distance between the pole faces L_1 (which is a known quantity). To achieve this target, the following modification has been proposed in the upper yoke of permeameter. As shown in Fig. 4.5, beneath the limbs of the upper yolk, wedge-shaped iron poles are inserted. Contact lines between the poles and sheet surface are positioned at the distance L_1.
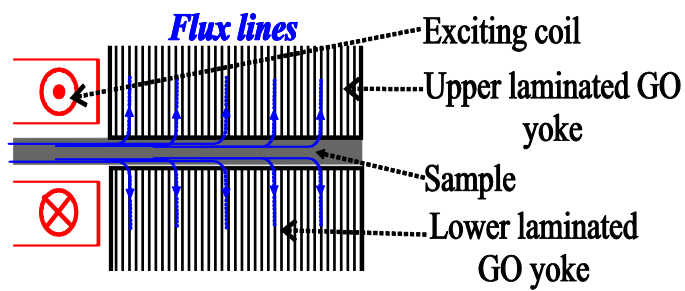
Fig. 4.4 Standard Configuration
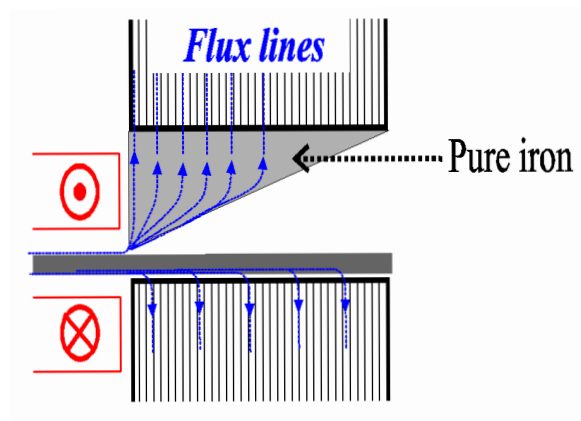
Fig. 4.5   Modified Configuration: the massive Wedge shaped poles have in practice flux ϕ_1 = 0 when the feedback is operational

Thus the flux path length in the sample matches the same distance L_1 under the operation of feedback system.

Once the magnetic path length becomes fixed such as $L_s = L_1$, and the flux in the yoke of the permeameter is compensated precisely, we can easily obtain the exact magnetic field H in the sample according to the following expression

$$N \cdot I = H \cdot L_1 \tag{4.3}$$

4.1.3   Principle of MMF compensation

The compensation scheme proposed here is based upon the idea of cancellation of MMF analogous to the use of the Chattock coil. This approach is proven to be much simpler as compared to the Rogowski-Chattock [51]. Unlike the weak and noisy signal generated by the Chattock coil, the signal generated and controlled using this approach is large and therefore easy to handle. Here, the upper yoke by itself is used as a zero MMF indicator. A secondary coil of few turns is wrapped around the upper yoke to obtain the derivative of magnetic flux ϕ_1 flowing through the upper yoke. The equivalent reluctance circuit of the proposed scheme is given in Fig. 4.6. Here the reluctance of the sample is represented by R_s, reluctance of lower and upper yoke by R_Y, and reluctance of wedge-shaped pole by R_p. It is evident that magnetic flux drop E, the drop occurring outside the sample, is directly proportional to the derivative of the flux ϕ_1. As there is no other MMF source in the upper yoke, so if somehow the magnetic flux ϕ_1 gets canceled, E will reduced to zero and when this happens, the corresponding voltage $v_1 \propto \frac{d\phi_1}{dt}$ induced in the secondary coil will also become zero. The only MMF drop in the circuit under such conditions will be the one across the sample.

The condition has been obtained by employing compensation windings on the lower yoke of the permeameter. Its output is controlled and adjusted in such a way as
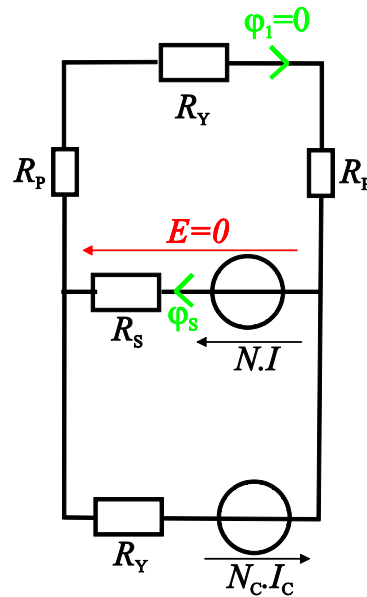
Fig. 4.6   Equivalent Reluctance circuit of compensated permeameter

to generate flux equal to ϕ_1 and opposite to its direction. Under such condition, the net flux flowing through the yoke of the permeameter and corresponding magnetic flux drop E is made equal to zero. The schematic diagram of the feedback control loops is given in Fig. 4.7. The output of the compensation windings (N_cI_c) on the lower yoke is adjusted via PID controller and then amplified with a high gain amplifier in such a way that the voltage v_1 is brought to zero.

The proposed method is very simple as it does not require any MMF sensor. Moreover, the sensitivity is very high. The yoke is made of highly permeable GO lamination due to which the signal to noise ratio is very good. The voltage obtained from the windings wounded on the upper yoke is very high as compared to the voltage obtained from chattok coil. Therefore, it is much more precise and relatively easy for the feedback system to control it to zero. The pole reluctance R_p due to the poor contact between the sample and wedge shape pole carries negligible effects upon the performance of permeameter because the flux in the upper pole is ultimately made to disappear.
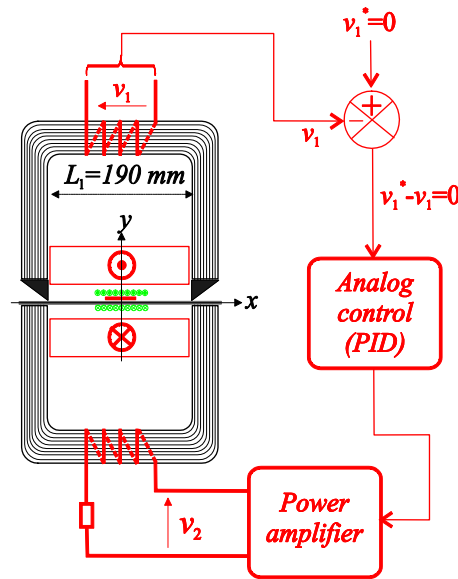
Fig. 4.7   Compensated permeameter's control circuit

4.1.4   Experimental results

Non-oriented Fe-(3wt%)Si sheets and high-permeability grain-oriented (HiB) sheets having a thickness of 0.35 mm and 0.28 mm respectively, have been tested in the compensated permeameter. Under sinusoidal induction waveform at 100 Hz, apparent power, hysteresis loops and energy loss have been measured with a peak polarization range of 0.2 T $\leq J_p \leq$ 1.5 T. The value of magnetic field H can either be found locally using H-coil placed at the center of the strip or by measuring the magnetizing current in the primary windings (MC method).

Non-oriented Fe-Si steel sheets

Energy loss vs. peak polarization obtained by utilizing the H-coil method and MC method is shown in Fig. 4.8. The system has been used in a compensated and uncompensated mode, with and without wedge-shaped poles. The results are then compared to the one obtained via H-coil. It can be seen that the use of uncompensated permeameter have resulted in overestimated values because of the
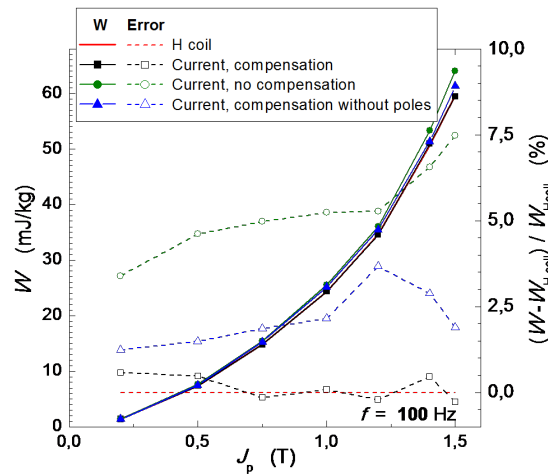
Fig. 4.8   Comparison of the energy loss measured by the H-coil method and the current measurement method

MMF drop in the yokes. In addition, the loss deviation increases with increase in the value of J_p and a deviation of about 7 percent can be seen at high J_p. When the compensated permeameter is used without the wedge-shaped poles, the loss values are still overestimated, ranging between 2 to 4%. It is due to the fact that magnetic flux lines cannot be limited exactly to the distance between the pole faces L_1, and that the real value is somewhat larger. Finally, the results with compensation scheme including wedge-shaped iron poles shows remarkable agreement with the local H-coil measurements.

Fig. 4.9 shows the corresponding hysteresis loops measured via local H-coil, MC method with compensation without compensation. It can be seen that a very good resemblance is obtained between the H-coil and the compensated current methods.

Grain-Oriented HiB sheets

The use of the permeameter becomes more important in case of grain-oriented materials. Here, the MMF drop in the yokes is higher as compared to that of
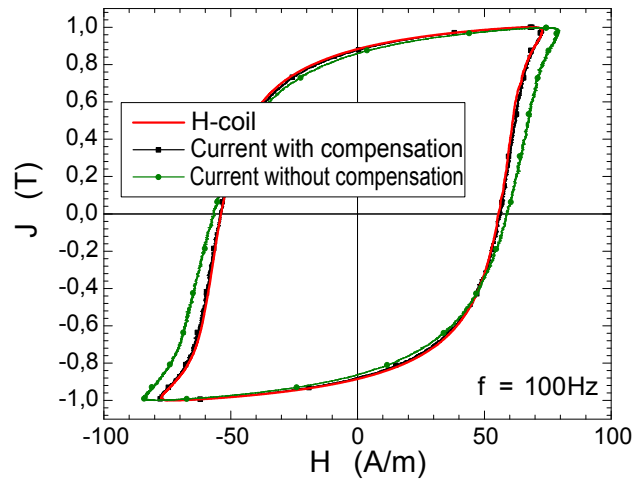
Fig. 4.9   Comparison of the cycles measured by the H-coil method and by MC method, with and without compensation
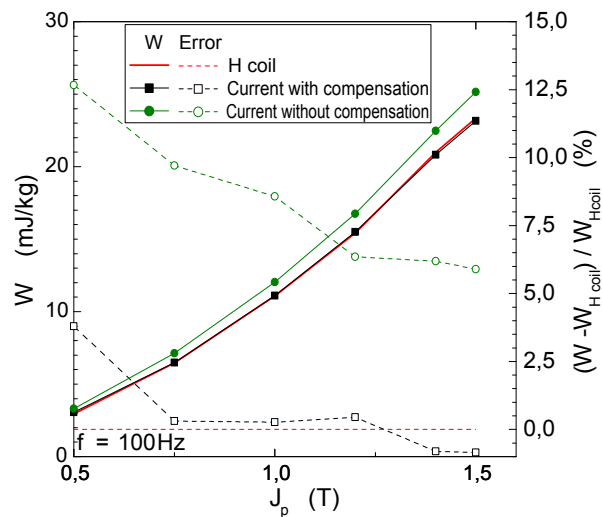
Fig. 4.10   Energy loss comparison of H-coil method and MC method with and without compensation.

the sample, and the loss in the yokes become more important. The signal can be very small in this case, especially at low frequencies, due to which the localized measurements with H-coil can be very challenging. The proposed design is very helpful and interesting under such conditions. Figure 4.10 shows energy loss values obtained through MC method, with and without compensation, and via local H-coil method in grain-oriented HiB sheet. In the case of a compensated permeameter, the results are in a very good agreement with that of an H-coil. When an uncompensated permeameter is used, it is observed that the MC method overestimates the magnetic loss by a remarkable extent. Overestimation of about 10% is observed at low induction levels ($J_p = 0.5$ T) and about 6% at high induction levels ($J_p = 1.5$ T). The observed behavior is expected because the loss in the yoke does not depend upon the type of material under test but instead depends only on J_p.

Behavior of the measured apparent power is given in Fig. 4.11. Again, remarkable resemblance is obtained between the results obtained via MC method with compensation, and that of H-coil method. A small difference of 3% in the apparent power is observed between the two techniques at low J_p. Small signal levels, and integration problems associated with H-coil may be the main reasons of this difference and the proposed method is therefore very useful in this regard.
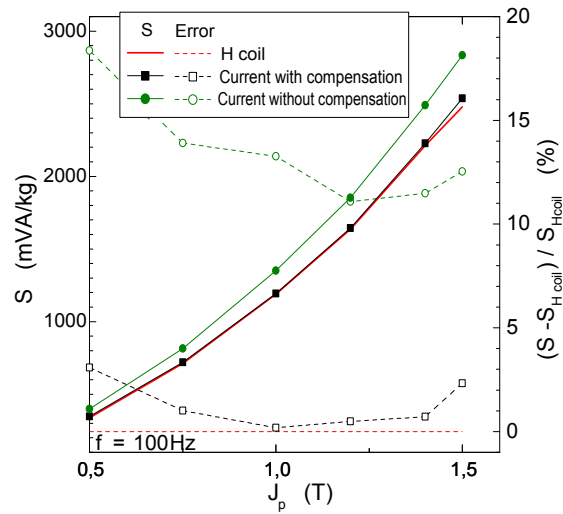
Fig. 4.11   Apparent Power comparison of H-coil method and MC method with and without compensation.

4.1.5   Conclusion

A permeameter has been designed for accurate power loss measurements by compensating the MMF drop in the flux closing yoke. It uses a wedge shaped pole face for obtaining a precise magnetic path length. The permeameter works on the principle of using the flux-closing yoke for sensing and compensation. The performance of the device has been validated by measurements on different non-oriented and grain-oriented Fe-Si sheets.

Chapter 5

Alternating and rotational losses in non-oriented steel sheets at high inductions

5.1   Introduction and motivation

Iron cores of electrical machines are subjected to complex operating conditions, including 2-D fluxes and high induction levels often close to magnetic saturation. The characterization of magnetic materials in these conditions, over a broad range of frequencies, can be a challenging task because of the difficulties in the control of the waveforms and the required power. Very limited literature has been published so far about this topic [16] [17] [18], so compelling machine designers to extrapolate the data obtained in standard conditions at medium inductions and frequencies to these extreme working conditions, a process that entails errors in the evaluation of the electrical machine efficiency. A detailed investigation of different magnetic materials under 2-D flux is therefore required. To this purpose, in this chapter we will display and discuss some results of measurements obtained on a Fe-(3.2wt%)Si circular

disk sample. Two kind of three-phase magnetizers are applied in combination of fieldmetric and thermometric techniques as dicussed in section 3.2.2. We have measured the alternating and rotating magnetic loss over a wide range of peak polarization J_p (0.1 T - 1.965 T) and frequency f (2 Hz- 1 kHz).

5.2 Experimental setup and sample geometry

The experimental setup used for the characterization of non-oriented Fe-(3.2wt%)Si sheets under rotational and alternating fields is shown in Fig. 5.1, whereas the electronic scheme has already been depicted in Fig. 3.13 and 3.14 in Chapter 3. The disk shaped samples with a diameter of 80 mm, and 0.35 mm thickness, are laser cut and annealed at 780 °C for 2 hours in vacuum. Their physical parameters are listed below

electrical conductivity $\sigma = 2.04 \times 10^6$ S/m ;

density $\delta = 7650$ kg/m^3 ;

average grain size (s) $= 92 \times 10^{-6}$ m ;

specific heat per unit mass c_p= 462 J/(kg $\cdot$ K) ;

saturation polarization $J_s = 2.01$ T ;

sheet thickness $d = 0.356$ mm .
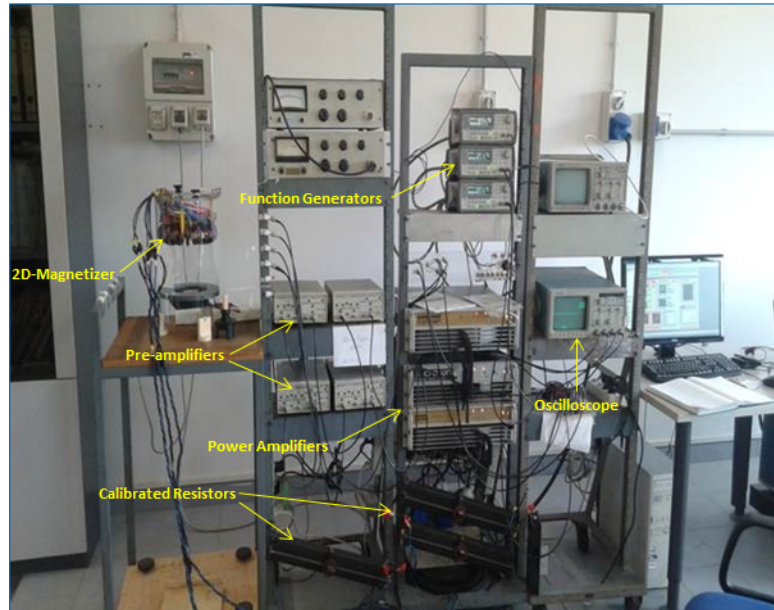
Fig. 5.1   Setup for 1D and 2D characterization of magnetic materials. Three function generators provide suitable voltage to the primary windings of the magnetizer, through a power amplifier, that in turn setup the desired fields in the sample. The corresponding values of B and H detected by the sensors are amplified, converted to digital form via oscilloscope, and then elaborated by a software in the PC.

5.3   Results and discussion

Fig. 5.2 and 5.3 report the energy loss behavior vs. peak induction under alternating and rotational supply conditions, in the frequency range (2 Hz -1 kHz), up to B_p = 2.0 T. Approaching saturation, the difference between peak induction B_p and peak polarization J_p cannot be neglected, and then it might be appropriate to distinguish between the $W^{(\mathrm{ALT})}$ and $W^{(\mathrm{ROT})}$ dependence on B_p and J_p. In the current situation, a maximum polarization value J_p= 1.965 T was achieved at B_p= 2.0 T. It should be noted that W_hyst and W_exc depends upon J_p only, whereas the classical loss depends upon B_p, and consequently the contribution of the term $\mu_0 H$ cannot be ignored. Under alternating conditions, the measurements are carried out separately along the easy and hard axis and then averaged to get the loss. Fig. 5.4 reports the high induction region of the experimental 2-D loss curve v.s J_p, plotted as a function of

reduced polarization $J_\mathrm{p}/J_\mathrm{s}$, up to $f = 200$ Hz. It can observed that 200 Hz is the maximum frequency at which the sample under investigation was brought very close to saturation magnetization due to the power limit of the setup. In addition, the dashed lines in Fig. 5.4 represent the rotational classical loss, which is twice the classical loss under alternating conditions

$$W_\mathrm{class}^{(\mathrm{ROT})} = \frac{\pi^2 \sigma d^2 f B_\mathrm{p}^2}{3} \; \left(\mathrm{J/m^3}\right) \quad , \tag{5.1}$$

being such formula valid under negligible skin effect. A remarkable result is the ability of the equipment to point out the theoretical limit of rotational loss, where the total loss becomes equal to the classical loss upon reaching the saturation polarization.

By applying the loss separation procedure, the hysteresis loss $W_\mathrm{hyst}^{(\mathrm{ROT})}$ is obtained by extrapolating the quantity $W_\mathrm{diff}^{(\mathrm{ROT})} = W^{(\mathrm{ROT})} - W_\mathrm{class}^{(\mathrm{ROT})}$ up to $f = 0$ Hz. The excess loss W_exc is then obtained as

$$W_\mathrm{exc}^{(\mathrm{ROT})}(f) = W^{(\mathrm{ROT})}(f) - W_\mathrm{hyst}^{(\mathrm{ROT})}(f) - W_\mathrm{class}^{(\mathrm{ROT})}(f). \tag{5.2}$$

From Fig. 5.5, it can be observed that W_hyst and W_exc start to decrease beyond $J_\mathrm{p}/J_\mathrm{s} \approx 0.75$. Upon reaching saturation induction $J_\mathrm{p}/J_\mathrm{s} \approx 0.98$, the two loss components become zero as the total loss $W^{(\mathrm{ROT})}$ reduces to $W_\mathrm{class}^{(\mathrm{ROT})}$. The application of the Statistical Theory of Loss, provides the following expression for the excess loss under rotational magnetization flux loci [39]

$$W_\mathrm{exc}^{(\mathrm{ROT})} \cong g \cdot 8.76 \cdot \sqrt{\sigma G S V_\mathrm{o} J_\mathrm{p}^3} \cdot \sqrt{f} \qquad \left(\mathrm{J/m^3}\right), \tag{5.3}$$

where $G \cong 0.1356$, S is the cross-sectional area of the sample, σ is the conductivity and V_o is a statistical parameter, depending on J_p. The value of g in the rotational case is approximately equal to 1.8 (Eq. 2.57 in chapter 2).
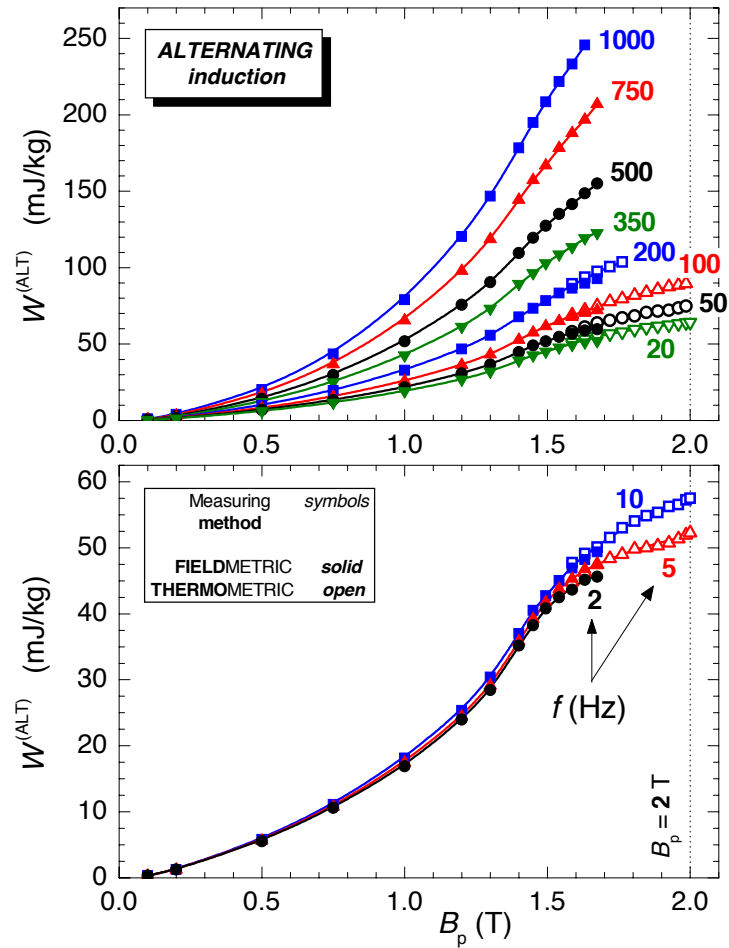
Fig. 5.2   Energy loss vs. peak induction in the frequency range (2 Hz- 1 kHz) under **alternating** sinusoidal flux. At low induction, measurements are carried out by fieldmetric method (solid symbols) while measurements at high induction are carried out by thermometric method (open symbols). Remark that a region exists where the solid and the open symbols overlap.
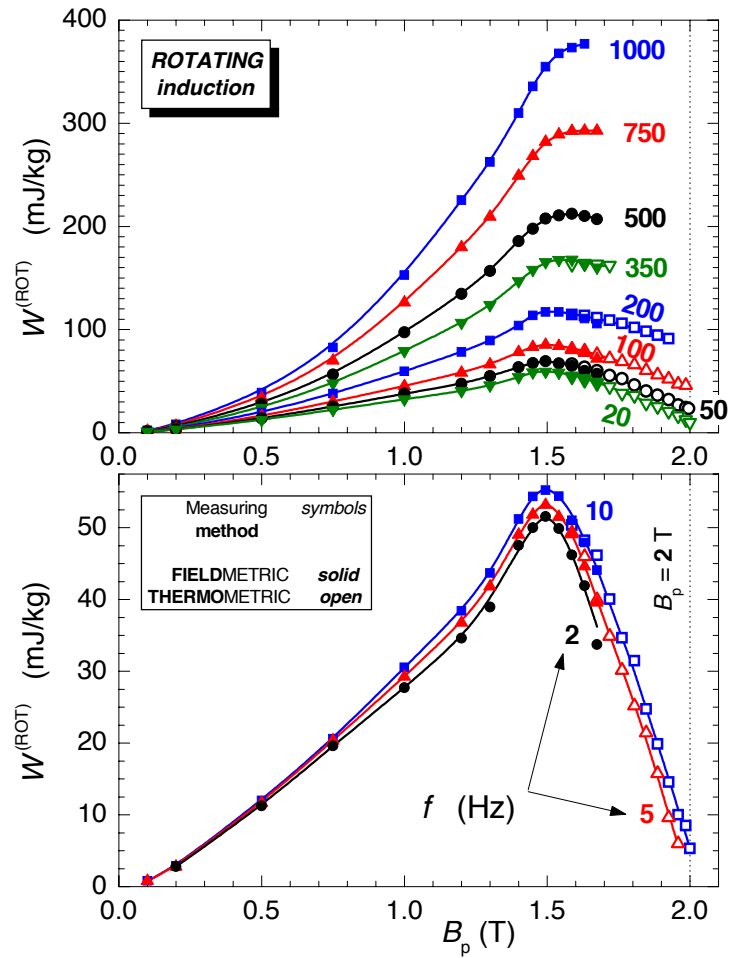
Fig. 5.3   Energy loss vs. peak induction in the frequency range (2 Hz- 1 kHz) under **rotational** flux. As in Fig. 5.2, measurements are carried out by applying both fieldmetric and thermometric methods and a region exists where the solid and the open symbols overlap.
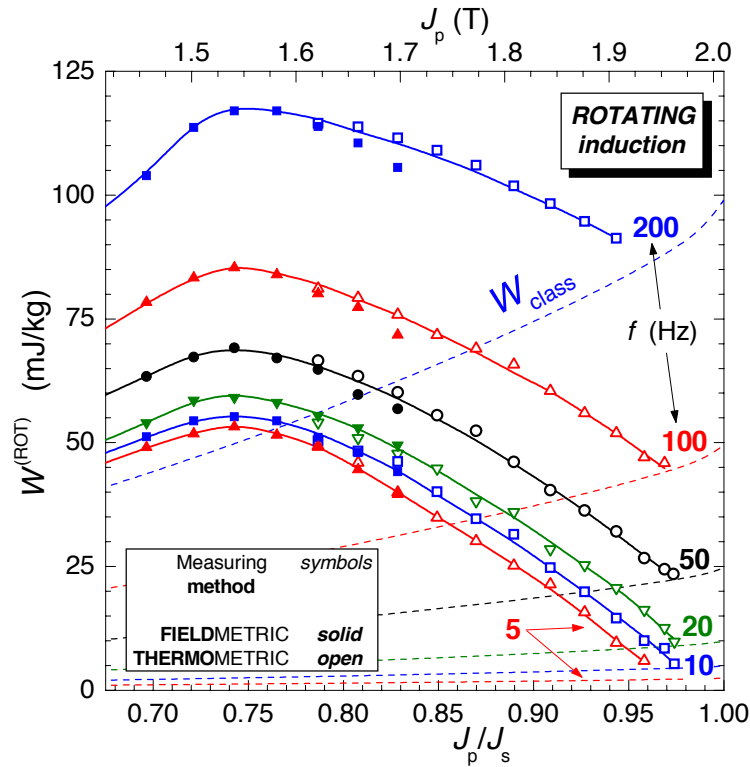
Fig. 5.4   2-D loss behavior at high polarization values close to saturation. Rotational loss (solid lines) achieves the value of classical loss (dashed lines) at $J_p/J_s \cong 0.98$.

We have validated the theoretical formula Eq. 5.3, under both rotational and alternating conditions, by comparing it with the experimental data. As an example, Fig. 5.6 and 5.7 show, under alternating and rotational inductions, the $\sqrt{f}$ dependence predicted by Eq. 5.3 at $B_p = 1.4$ T. The divergence from the experimental data at high frequencies is due to the appearence of skin effect. In Fig. 5.8, the ratio $R_{hyst} = W_{hyst}^{(ROT)}/W_{hyst}^{(ALT)}$ is plotted versus J_p/J_s. It can be noticed that it decreases monotonically, eventually becoming zero at saturation. In addition, results obtained by Brailsford [63] for different materials are superposed. We can argue that R_{hyst} follows a rather universal behavior in non-oriented sheets.

Fig. 5.9 shows the alternating and rotational excess loss, along with their ratio R_{exc}. In this case, different symbols in the graph represent different frequencies. Though some scattering is present in the experimental data, in particular at low
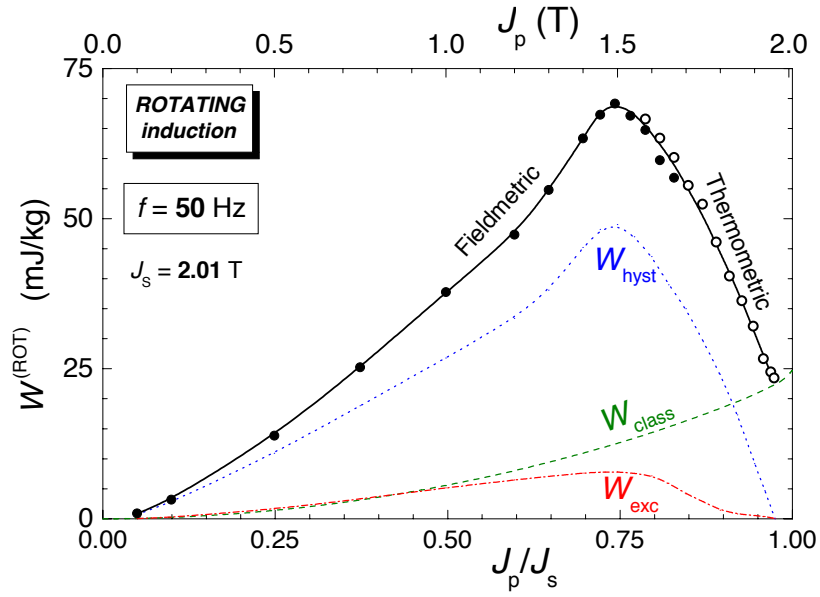
Fig. 5.5 Separation of loss obtained under rotating induction at 50Hz. The components W_{hyst} and W_{exc} vanishes at $J_p/J_s \approx 0.98$ as the total loss approaches to W_{class}.

frequency regimes, it can be stated confidentially that the ratio R_{exc} is independent of frequency.

5.3.1 Example of practical estimation of loss under a given 2-D flux

On the basis of the above results, we have applied the procedure discussed in section 2.4 by which the 2-D magnetic loss under any polarization loci (alternating, circular, elliptical) can be obtained. Fig. 5.10 reports an example of B-loci in a non-oriented material at $J_p = 1.14$ T. The first step is to determine an equivalent elliptical loci having same J_p and area of the B-loci. Once we have obtained it, the different loss components can be computed by applying equations given in section 2.4. Let us start our analysis from hysteresis loss, that is computed by applying the following equation
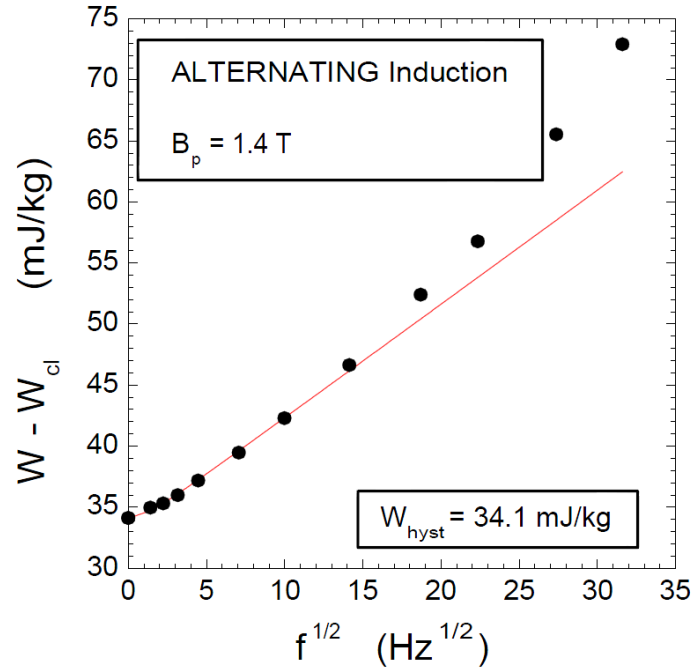
Fig. 5.6 Predicted dependence of $W - W_{cl}$ vs. $\sqrt{f}$ by applying Eq. 5.3 at $B_p = 1.4$ T under **alternating** flux (solid line) . The dots represent the experimental values. W_{hyst} is obtained by extrapolating the experimental data up to $f = 0$ Hz. The difference between the theoretical results and the experimental data, at high frequencies, is due to the emergence of skin effect.

$$W_{hyst}(J_p, a) \cong W_{hyst}^{(ALT)}(J_p) + W_{hyst}^{(ALT)}(aJ_p) \cdot \left(R_{hyst}(J_p) - 1 \right) \tag{5.4}$$

The corresponding values of $W_{hyst}^{(ALT)}$ at $J_p = 1.14$ T and $aJ_p = 0.81$ T as well as R_{hyst} at $J_p = 1.14$ T can be obtained from Fig. 5.8. Let us now compute the excess loss which is given as

$$W_{exc}(J_p, a, f) \cong g(a) \left\{ W_{exc}^{(ALT)}(J_p, f_0) + W_{exc}^{(ALT)}(aJ_p, f_0) \cdot \left[\frac{R_{exc}(J_p)}{g(1)} - 1 \right] \right\} \frac{\sqrt{f}}{\sqrt{f_0}} \tag{5.5}$$

From Fig. 5.9, the corresponding values of $W_{exc}^{(ALT)}$ at $J_p = 1.14$ T and $aJ_p = 0.81$ T as well as R_{exc} at $J_p = 1.14$ T can be obtained. For $a = 0.71$, the corresponding value of $g(a)$ can be obtained by using Eq. 2.57. Finally, the classical loss is computed through numerical integration, under negligible skin effect, as
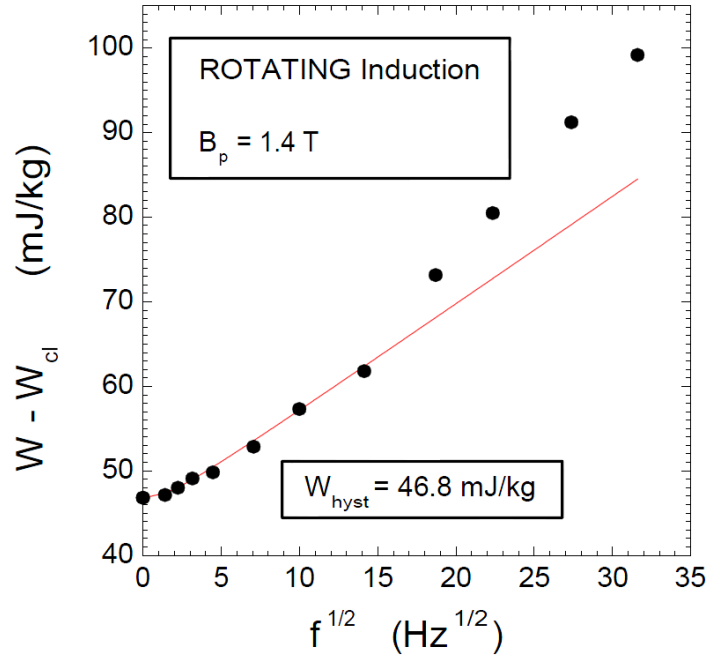
Fig. 5.7   Predicted dependence of $W - W_{cl}$ vs. $\sqrt{f}$ by applying Eq. 5.3 at B_p = 1.4 T under **rotational** flux (solid line). The dots represent the experimental values. W_{hyst} is obtained by extrapolating the experimental data up to $f = 0$ Hz. The difference between the theoretical results and the experimental data, at high frequencies, is due to the emergence of skin effect.

$$W_{cl} = \frac{\sigma d^2}{12} \int_0^{1/f} \left[\left(\frac{dB_x}{dt} \right)^2 + \left(\frac{dB_y}{dt} \right)^2 \right] dt \qquad (5.6)$$

Fig. 5.11 shows the computed total energy loss behavior vs. frequency, together with the loss components.

5.4   Conclusion

Loss characterization of non-oriented Fe-(3.2wt %)Si steel sheet has been performed using a three phase magnetizer under 1-D and 2-D flux till very high induction levels-close to magnetic saturation. It was shown experimentally for the first time that upon approaching saturation, the total measured loss coincides with the theoretically predicted classical loss, in the absence of skin effect. Since the alternating and
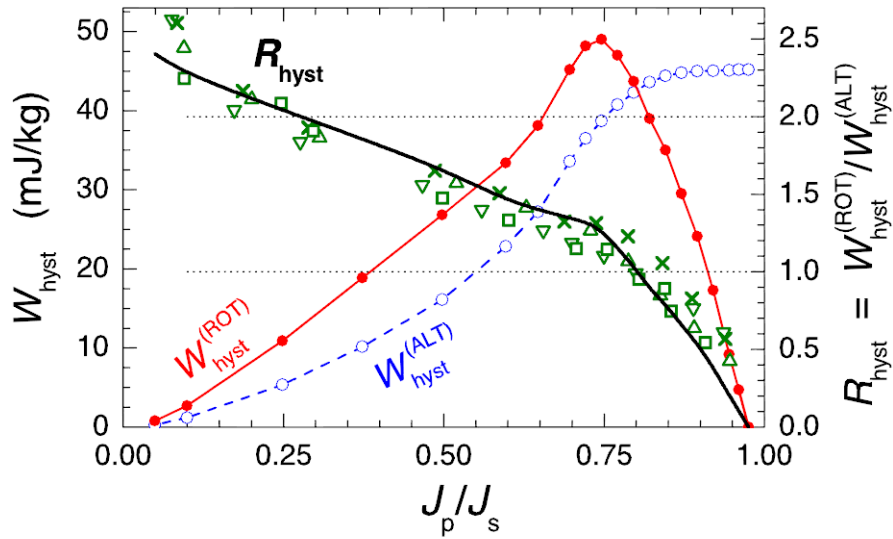
Fig. 5.8   Comparison of our results for R_{hyst} (represented by black line) to those obtained by Brailsford for different magnetic materials [63]. Different symbols represent different materials. It can be seen that R_{hyst} follows a rather universal behavior and decreases monotonically eventually becoming zero at saturation. $W_{\text{hyst}}^{(\text{ROT})}$ and $W_{\text{hyst}}^{(\text{ALT})}$ are the hysteresis loss obtain under rotational and alternating conditions respectively. It can be seen that at high inductions, $W_{\text{hyst}}^{(\text{ROT})}$ decreases drastically, while $W_{\text{hyst}}^{(\text{ALT})}$ remains almost constant.

the rotational energy loss components are found to be related in a rather universal fashion, at all frequencies, it is concluded that the loss under a given 2-D loci can be estimated on the basis of a limited set measurements, obtained under alternating conditions, and the corresponding loss ratios.
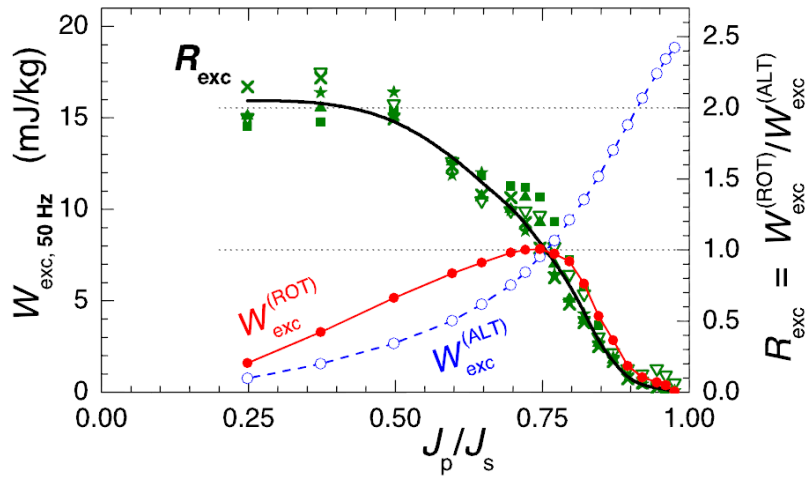
Fig. 5.9   The excess loss ratio R_{exc} at different values of J_p/J_s. Different symbols in the graph represent different frequencies. Despite of some scattering at low frequencies, it can be stated confidentially that the ratio R_{exc} is almost independent of frequency. Here, $W_{hyst}^{(ROT)}$ decreases at high inductions while $W_{hyst}^{(ROT)}$ continues to increase till magnetic saturation.
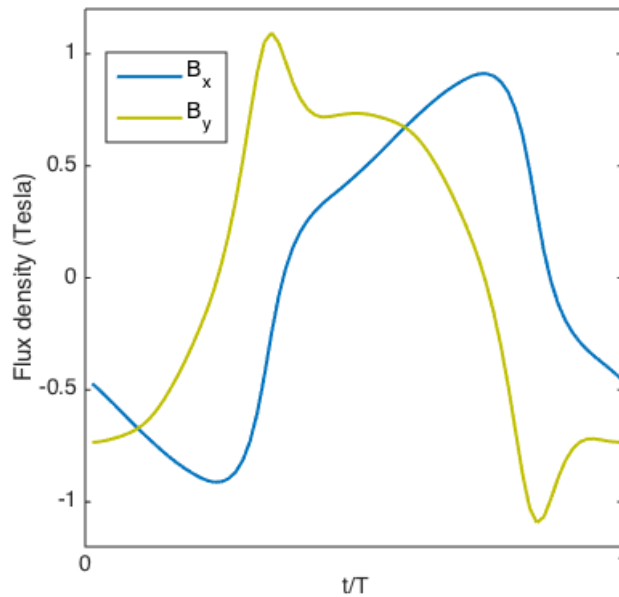
Fig. 5.10   Flux density vs. t/T for the two components of B-loci.
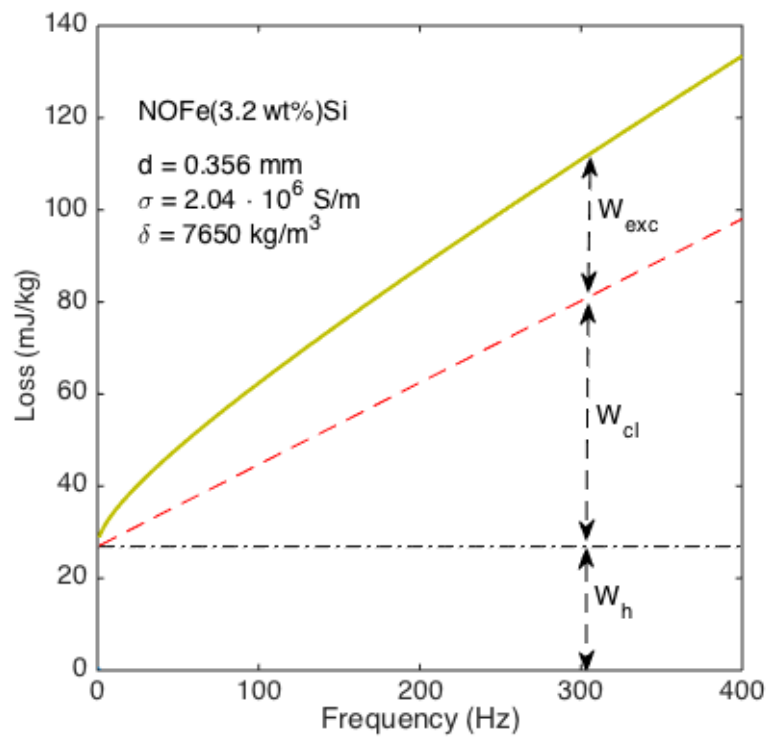
Fig. 5.11   The computed 2-D loss behaviour in a 0.356 mm thick non-oriented Fe-Si at J_p = 1.14 T. The hysteresis loss is computed by applying Eq. 5.4, the excess loss is computed by applying Eq. 5.5 and the classical loss by Eq. 5.6. The total loss is obtained by adding up the individual contributions.

Chapter 6

Classical loss computation under 1-D fluxes

6.1 Motivation

Classical loss discussed in section 2.2.2 plays a very important role in the loss separation approach based on STL. The computation of classical loss component usually assumes a uniform magnetization throughout the cross section of the magnetic sheet, thereby presupposing no skin effect. Under sinusoidal induction the classical energy loss is given by the equation

$$W_{\text{cl}} = \frac{P_{\text{cl}}}{f} = \frac{\pi^2 \sigma d^2 f B_{\text{p}}^2}{6} \quad , \tag{6.1}$$

where σ is the conductivity, B_{p} is the peak induction, and f is the frequency. It is worth noting that by this formula we can obtain the classical loss disregarding the magnetic constitutive law of the material. The assumption of negligible skin-effect is satisfied at low frequencies, but at high frequencies the same formula cannot be applied anymore and a solution of the magnetic diffusion equation is in general

required. The main challenge is posed by the material constitutive law and its intrinsic strong non-linearity. One possibility is to solve the diffusion equation through numerical models like as in [64, 65], under a hysteretic and dynamic constitutive relationship. However, at very low inductions, a linear approximation of the constitutive relationship equation ($\vec{B} = \mu \vec{H}$) can be assumed and the solution of Maxwell's equations can be worked out without resorting to numerical analysis. On the other end, at high induction a simple expression for the classical loss could be derived by assuming a kind of step-like characteristic. In this chapter, the two models for the classical loss will be worked out and the obtained theoretical results will be compared to the experimental data.

6.1.1   Computation of classical loss at low induction

At low induction a linear approximation of the constitutive equation ($\vec{B} = \mu \vec{H}$) is here adopted by assuming $\mu = B_p/H_p$, where B_p is the peak induction and H_p is the peak value of the magnetic field. As an example Fig. 6.1 shows the $B - H$ loop of a non-oriented Fe-Si lamination at $B_p = 0.2$ T where a constant relative permeability of $\mu = 5900$ can be assumed. Let us now derive a formula for the classical loss. Consider the sample geometry shown in Fig. 6.2. Here, the magnetic field is directed along the z-axis and the Maxwell's equations can be written as

$$\frac{\partial H_z}{\partial y} = j_x, \tag{6.2}$$

and

$$\frac{\partial j_x}{\partial y} = \sigma \frac{\partial B_z}{\partial t}. \tag{6.3}$$

After deriving Eq. 6.2 and replacing $\partial j_x / \partial y$ through Eq. 6.2, we obtain

$$\frac{\partial^2 H_z}{\partial y^2} = \sigma \frac{\partial B_z}{\partial t}, \tag{6.4}$$
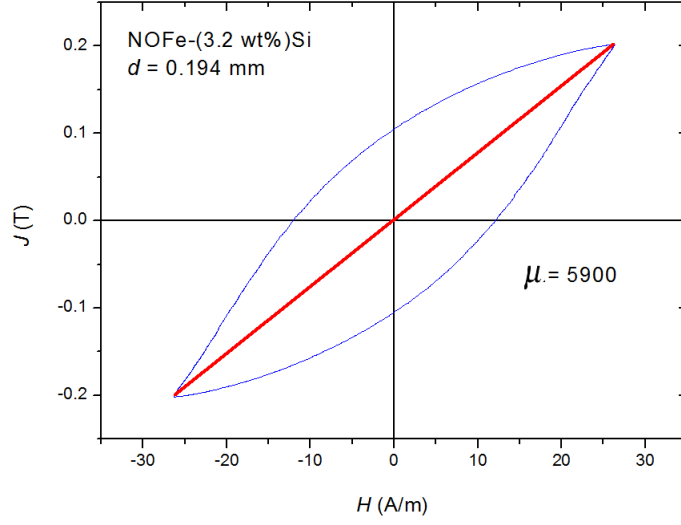
Fig. 6.1 $B - H$ loop of a 0.345 mm thick non-oriented Fe-Si at $B_p = 0.2$ T. At such low inductions, a constant relative permeability $\mu = 5900$ can be assumed.

Assuming the constitutive equation $B_z = \mu H_z$, we finally obtain

$$\frac{\partial^2 H_z}{\partial y^2} = \sigma \mu \frac{\partial H_z}{\partial t}.$$ (6.5)

Under sinusoidal regime, we can introduce complex quantities by which we obtain

$$\frac{\partial^2 \underline{H}_z}{\partial y^2} = j\sigma\omega\mu\underline{H}_z.$$ (6.6)

In addition, the following boundary conditions hold

$$\frac{\partial \underline{H}_z}{\partial y}\bigg|_{y = d/2} = j\omega\sigma\frac{d}{2}\underline{B}_{zp},$$ (6.7)

where $\underline{B}_{zp}$ is the average $\underline{B}_z$, and

$$\frac{\partial \underline{H}_z}{\partial y}\bigg|_{y = 0} = 0.$$ (6.8)
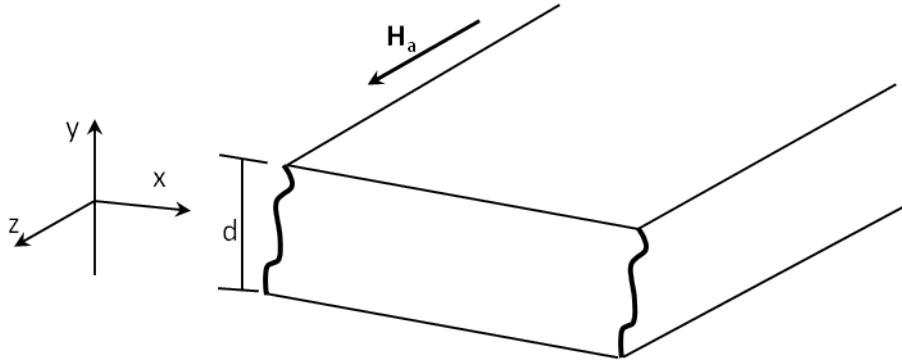
Fig. 6.2   The sample geometry for the computation of loss at low induction. Here d is the thickness along y axis and l is the width of the sample along the x-axis. The sample is assumed infinitely long and the external field is applied along z axis

The solution of previous Eqs. provide the classical loss [66] as

$$W_{\mathrm{cl}}(f) = \frac{\pi \gamma B_{\mathrm{p}}^2}{2} \cdot \frac{\sinh\gamma - \sin\gamma}{\cosh\gamma - \cos\gamma}, \quad [\mathrm{J/m^3}] \tag{6.9}$$

where

$$\gamma = \sqrt{\pi \sigma \mu d^2 f}. \tag{6.10}$$

If $\gamma \leq 2$, the skin effect can be neglected [67] and Eq. 6.9 is reduced to the standard classical formula (Eq. 6.1).

6.1.2   Computation of loss at high induction

This case is related to very high fields at which the materials exhibit a response close to ideal soft magnetic material, and hence become saturated at fields lower than the maximum field. One possibility is to adopt a kind of step-like $J - H$ characteristic because in such a case, a simple expression for the classical loss can be derived. As an example, Fig. 6.3 reports the $J - H$ loop of low carbon steel (LCS-3); see table 6.1. At high inductions, it can be seen that the loop can be well approximated by a step-like responce.
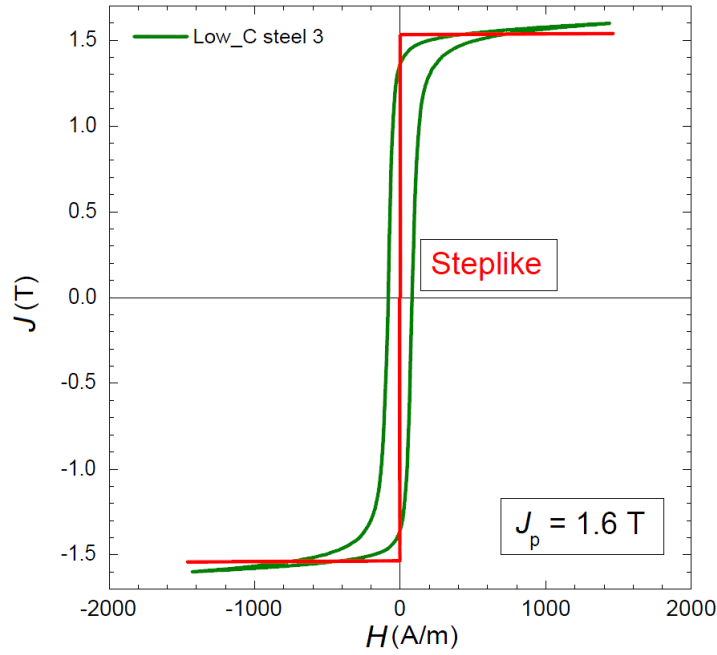
Fig. 6.3   The $J - H$ responce of sample LCS-3 at J_p = 1.6T (green line). At such a high induction, the constitutive relationship is highly non-linear and the loop can be approximated by a steplike responce (red line).

According to this approach, the magnetization change is not uniform. Instead, it occurs only in a certain portion of slab cross section in the form of one dimensional fronts as shown in Fig. 6.4. In our analysis we assume the peak induction equal to the maximum induction ($B_p \approx B_{max}$). Under these circumstances, the two symmetric fronts will propagate towards the center where they annihilate in each half period. The instantaneous values of $B(t)$ has a direct correspondence with the position of the front $y_F(t)$. For increasing B, we obtain

$$y_F(t) = \pm \frac{d}{4} \left[\frac{B(t)}{B_p} - 1 \right], \qquad (6.11)$$

and for decreasing B, the equation becomes

$$y_F(t) = \pm \frac{d}{4} \left[\frac{B(t)}{B_p} + 1 \right]. \qquad (6.12)$$
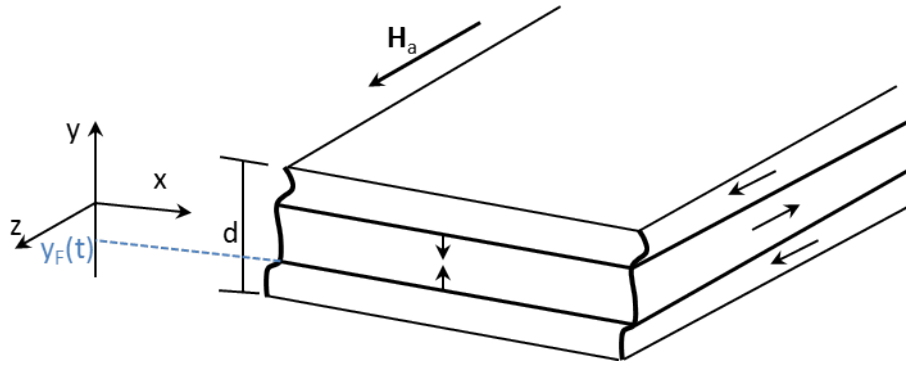
Fig. 6.4   Propagating fronts in magnetic materials observing step-like magnetization law

Due to the symmetry between the two fronts, we will limit the analysis to the region where $(-d/2 < y < 0)$. Applying Faraday's law we obtain

$$
j(y,t) = \begin{cases} -\frac{\sigma d}{2} \frac{\mathrm{d}B}{\mathrm{d}t} & -d/2 \leq y < y_F(t) \\ 0 & y_F(t) < y \leq 0 \end{cases}
\tag{6.13}
$$

By integrating Eq. 6.13 with respect to y, the field H is obtained as

$$
H(y,t) = \begin{cases} -\frac{\sigma d}{2} \frac{\mathrm{d}B}{\mathrm{d}t} [y_F(t) - y] & -d/2 \leq y < y_F(t) \\ 0 & y_F(t) < y \leq 0 \end{cases}
\tag{6.14}
$$

In addition, the following boundary condition holds

$$
H(y,t) \mid_{y=\pm d/2} = H_a(t),
\tag{6.15}
$$

where $H_a(t)$ is the applied field. Incorporating Eq. 6.11 and 6.12 in Eq. 6.14, the following magnetization law is obtained

$$
H_a(t) = \frac{\sigma d^2}{8} \left[\left| \frac{\mathrm{d}B}{\mathrm{d}t} \right| \frac{B(t)}{B_\mathrm{p}} + \frac{\mathrm{d}B}{\mathrm{d}t} \right].
\tag{6.16}
$$

Here, the field is proportional to frequency f as it depends upon $\mathrm{d}B/\mathrm{d}t$. As the power loss per unit cycle is given by

$$W_{\mathrm{cl}}^{(\mathrm{SWM})} = \frac{P_{\mathrm{cl}}^{(\mathrm{SWM})}}{f} = \int_0^{1/f} H_{\mathrm{a}} \frac{\mathrm{d}B}{\mathrm{d}t} \mathrm{d}t, \tag{6.17}$$

by incorporating Eq. 6.16 in 6.17, we obtain

$$W_{\mathrm{cl}}^{(\mathrm{SWM})} = \frac{\sigma d^2}{8} \int_0^{1/f} \left[\left| \frac{\mathrm{d}B}{\mathrm{d}t} \right| \frac{B(t)}{B_{\mathrm{p}}} \frac{\mathrm{d}B}{\mathrm{d}t} + \left(\frac{\mathrm{d}B}{\mathrm{d}t} \right)^2 \right] \mathrm{d}t. \tag{6.18}$$

As the first term of the right hand side of equation 6.18 oscillates to zero, Eq. 6.18 is reduced to

$$W_{\mathrm{cl}}^{(\mathrm{SWM})} = \frac{\sigma d^2}{8} \int_0^{1/f} \left(\frac{\mathrm{d}B}{\mathrm{d}t} \right)^2 \mathrm{d}t, \tag{6.19}$$

Under sinusoidal induction Eq. 6.19 becomes

$$W_{\mathrm{cl}}^{(\mathrm{SWM})} = \frac{\pi^2}{4} \sigma d^2 B_{\mathrm{p}}^2 f = 1.5 W_{\mathrm{cl}}(f). \tag{6.20}$$

From this relation, it can be observed that the SWM model provides a classical loss much greater than the loss obtained under uniform flux density (Eq. 6.1). The expriment will show that this approach unfortunately leads to non-physical results because the computed classical loss can result greater than the experimental.

6.2 Experimental

Magnetic energy losses have been measured at low and high inductions at different frequencies to compare the theoretical results, obtained with the models discussed in the previous sections. Table 6.1 provides the list of the investigated low carbon steels (LCS) and non-oriented iron silicon alloys. The samples have been chosen because of different conductivity, thickness and density. At high inductions, the

LCS samples emulate a step-like response. In addition, the classical loss is relatively high compared to the excess loss because of the low resistivity. The samples have been measured either as Epstein strips or ring samples and the measurements have been performed with the calibrated wattmeter-hysteresisgraph, described in section 3.2.1, under controlled sinusoidal induction. At low induction, the frequency span from quasi-static conditions up to 10 kHz. On the other hand, at high inductions the analysis is only limited to the region not influenced by the skin effect. Because of different conductivity, sheet thickness, and permeability, the frequency span not influenced by skin effect varies from one sample to another. Two different Epstein frames have been used with number of turns equal to 200 and 700.

Table 6.1   The list of non-oriented and low carbon steel sheets analyzed at very high and low inductions. The samples have been measured either as Epstein strip or a ring. The LCS samples in particular have low resistivity and tends to emulate a step-like response.

Material	Sample shape	Density (kg/m^3)	Resistivity $(\Omega \cdot m)$	Thickness (mm)
LCS-1	Epstein	7850	19.2×10^{-8}	0.506
LCS-2	Ring	7860	15.3×10^{-8}	0.507
LCS-3	Epstein	7870	12×10^{-8}	0.636
Fe-Si (NO)- 1	Ring	7650	52×10^{-8}	0.194
Fe-Si (NO)- 2	Epstein	7600	56×10^{-8}	0.345

6.2.1   Low induction measurements

The loss has been measured at $J_p = 0.2$ T and frequency ranging from quasi-static conditions up to 10 kHz. Fig. 6.5 shows the total loss decomposed into its three components, with the classical loss computed by applying Eq. 6.9, and assuming a relative permeability $\mu = 5900$. Fig. 6.6 reports the quantity $W_{diff} = W_{tot} - W_{cl}$ vs. $\sqrt{f}$ up to $f = 10$ kHz. The hysteresis loss W_{hyst} has been obtained by extrapolation up to $f = 0$ Hz. The quantity $W_{diff} = W_{hyst} + W_{exc}$ is then computed theoretically where W_{exc} is obtained through the following equation

Fig. 6.5 Measured energy loss at $J_p = 0.2$ T up to 10kHz, in 0.194 mm thick non-oriented Fe-(3.2wt%)Si sample. The open circles represent the experimental loss. The total loss is decomposed into its three components where $W_{cl}(f)$ is obtained through Eq. 6.9.

$$W_{exc} = 2n_0V_0J_p \cdot \int_0^{\pi/2} \left(\sqrt{1 + \frac{8\sigma GSV_0}{n_0^2V_0^2}\pi fJ_p cos\phi} - 1 \right) cos\phi d\phi \qquad (6.21)$$

In addition, Fig. 6.7 shows the corresponding number of active magnetic objects n versus H_{exc}. It can be seen that the theoretically assumed linear dependence of n versus H_{exc} has been validated upon the complete range of frequencies.

We wanted to examine the limit of the standard classical formula neglecting skin effect (Eq. 6.1). To this end, the loss separation has been newly obtained by applying the classical loss formula Eq. 6.1 till 1 kHz and the results are shown in Fig. 6.8. Fig. 6.9 reports the quantity $W_{diff} = W_{tot} - W_{cl}$ vs. $\sqrt{f}$. Again, the experimental results have been validated theoretically by applying Eq. 6.21. However, as the frequency range is extended till 10 kHz, it can be seen from Fig. 6.11 that the quantity $W_{diff} = W_{tot} - W_{cl}$ deviates from $\sqrt{f}$ law beyond 2500 Hz because of the emergence of the
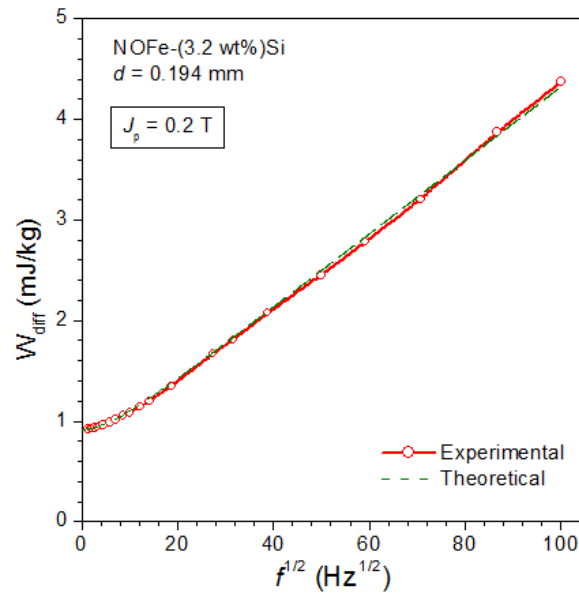
Fig. 6.6   The quantity $W_{\text{diff}} = W_{\text{tot}} - W_{\text{cl}}$ is plotted vs. the square root of frequency in the 0.194 mm thick non-oriented Fe-(3.2wt%)Si sample up to $f = 10$ kHz (open circles). The same quantity W_{diff} is then computed theoretically as $W_{\text{diff}} = W_{\text{hyst}} + W_{\text{exc}}$, where W_{exc} is obtained through Eq. 6.21 (dashed lines).
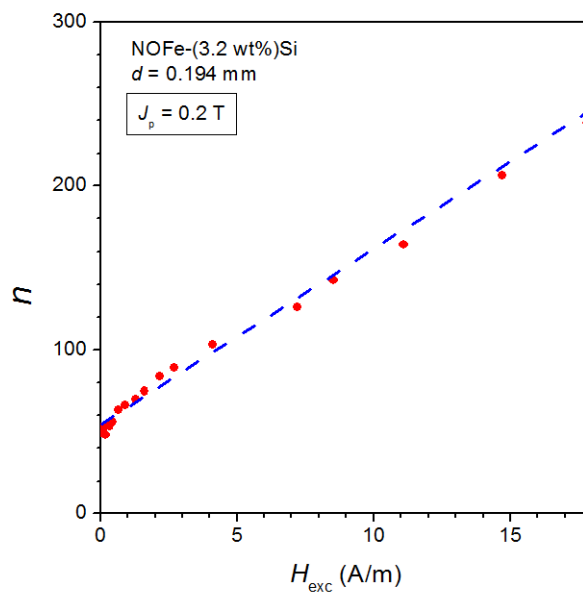
Fig. 6.7   The number of active magnetic objects n is plotted against H_{exc} in the investigated 0.194 mm thick non-oriented Fe-(3.2wt%)Si sample. It can be seen that n follows a linear relationship with H_{exc} upon the complete range of frequencies.
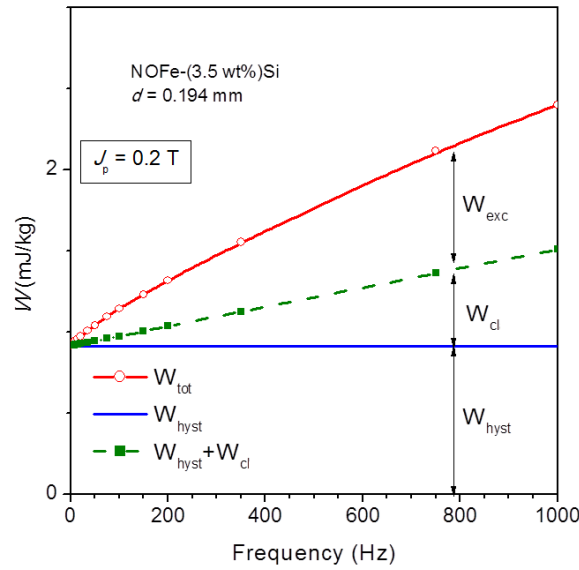
Fig. 6.8   Measured energy loss at J_p = 0.2 T up to 1 kHz in a 0.194 mm thick non-oriented Fe-(3.2wt%)Si sample. Experimental loss represented by open circles. The loss is decomposed in to its three components, where W_{cl} is obtained by applying standard classical loss formula (Eq. 6.1).
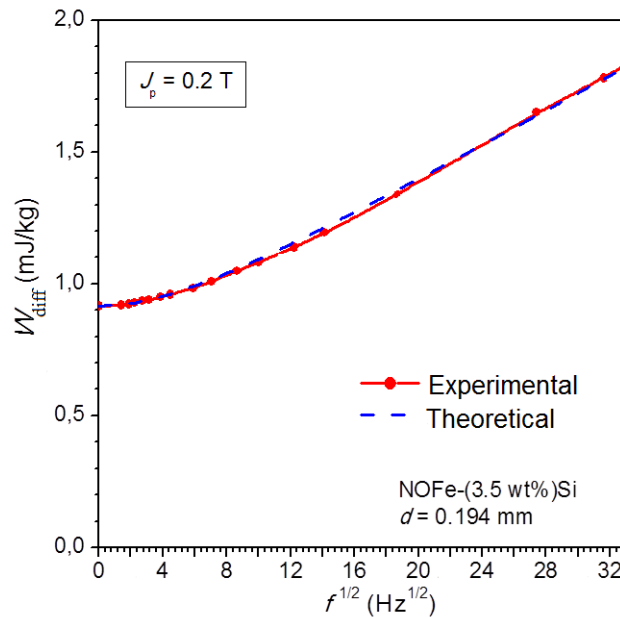
Fig. 6.9   Quantity $W_{diff} = W_{tot} - W_{cl}$ is plotted against $\sqrt{f}$ in 0.194 mm thick non-oriented Fe-(3.2wt%)Si sample till 1 kHz (dots), where W_{cl} is computed through standard classical loss formula (Eq. 6.1). The dashed line represents the same quantity obtained theoretically where Eq. 6.21 is applied to compute the excess loss.
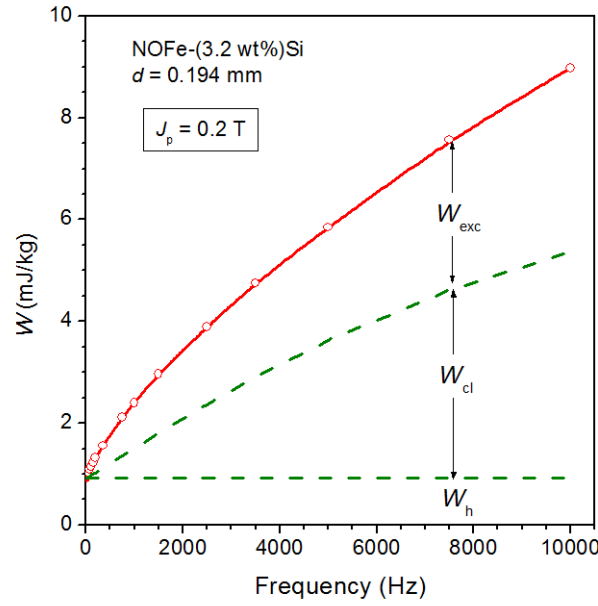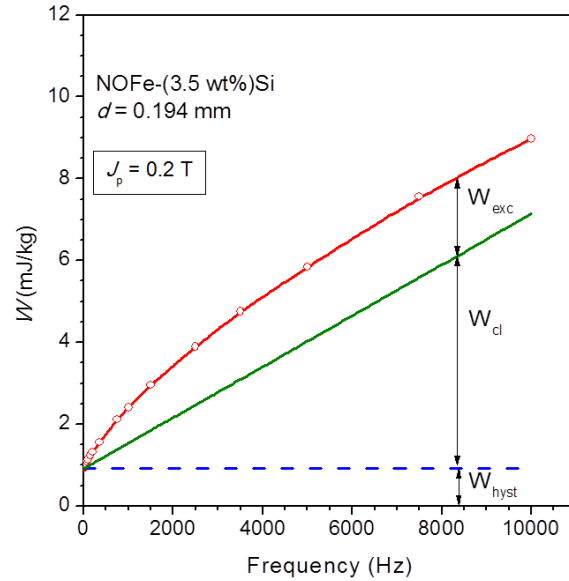
Fig. 6.10   Measured energy loss at J_p = 0.2 T up to 10 kHz in a 0.194 mm thick non-oriented Fe-(3.2wt%)Si sample. Experimental loss represented by open circles. The loss is decomposed in to its three components, where W_{cl} is obtained by applying standard classical loss formula (Eq. 6.1).

skin effect. A comparison between the classical loss formulas Eq. 6.9 and Eq. 6.1 is reported in Fig. 6.12. It can be seen that the two computed classical losses begin to deviate from one another at frequencies beyond 2500 Hz.

The conclusion is that at low inductions, the theoretical frame offered by STL can be applied even in the presence of skin effect.

6.2.2   High induction case

The investigation is now carried out on LCS steel sheets at high peak-induction (J_p = 1.6 T) to check the validity of the classical loss formula obtained under the SWM model (Eq. 6.20) . To this end, we have selected three LCS samples whose quasi-static $B - H$ loops emulate the step-like response (Fig 6.13). As the sample conductivity is high, the excess loss component is much lower than the classical loss. All the measurements have been restricted to the region not influenced by the skin
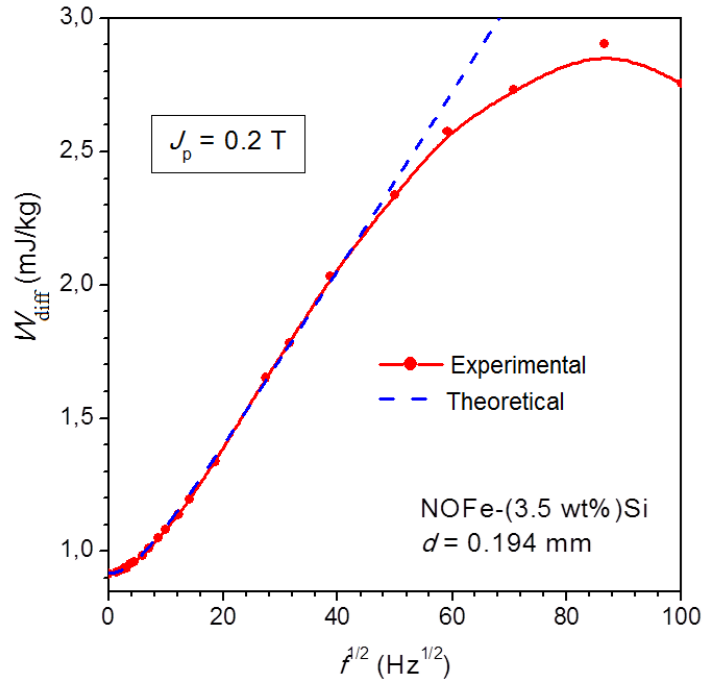
Fig. 6.11 $W_{\text{diff}} = W_{\text{tot}} - W_{\text{cl}}$ is plotted against $\sqrt{f}$ in a 0.194 mm thick non-oriented Fe-(3.2wt%)Si sample till 10 kHz (dots), where W_{cl} is computed through standard classical loss formula (Eq. 6.1). The same quantity $W_{\text{diff}} = W_{\text{hyst}} + W_{\text{exc}}$ (dashed lines) is computed theoretically where Eq. 6.21 is used to obtain the excess loss . Experimental W_{diff} deviates from $\sqrt{f}$ law beyond 2500 Hz due to the emergence of skin effect.

effect because we want to check one more time, the validity of the standard classical loss formula (Eq. 6.1).

We started our analysis with the experimental characterization of sample LCS-2, at $J_{\text{p}} = 1.6$ T. The classical loss was firstly computed by using the standard classical formula (Eq. 6.1). Fig. 6.14 shows the experimental quantity $W_{\text{diff}} = W_{\text{tot}} - W_{\text{cl}}$ and its theoretical counterpart $W_{\text{diff}} = W_{\text{hyst}} + W_{\text{exc}}$ where the excess loss is computed by applying Eq. 6.21. The experimental and theoretical results are in agreement till 500 Hz. Beyond this frequency, a significant deviation is observed. The reason is that the standard classical loss formula can no longer be applied in the presence of skin effect. Similar results are reported in Fig. 6.15 for the sample LCS-1. It is observed that the region of frequencies not influenced by the skin effect is limited to $f \cong 60$
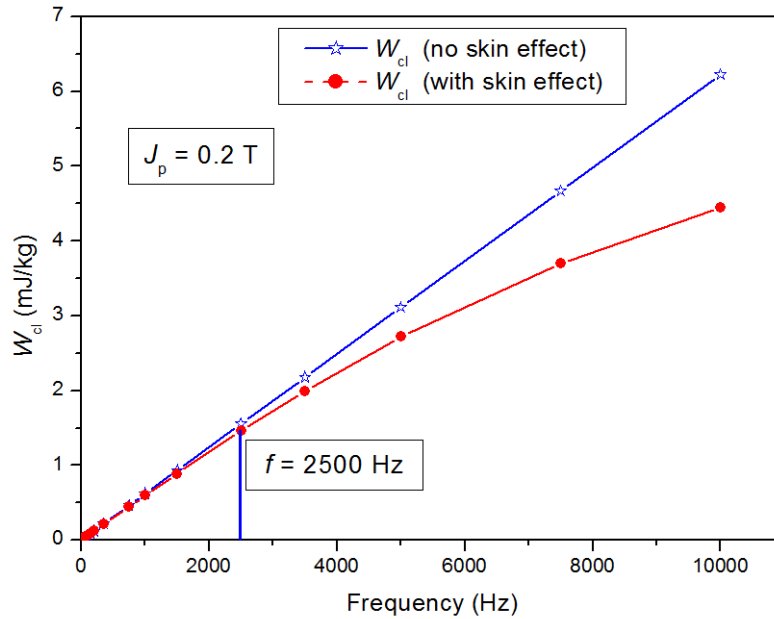
Fig. 6.12   Classical loss (with and without skin effect) is plotted vs. frequency in a 0.194 mm thick non-oriented Fe-(3.2wt%)Si sample till 10 kHz. W_{cl} (solid line) is obtained by applying standard classical loss formula (Eq. 6.1) while W_{cl} (dashed line), is obtained by applying Eq. 6.9, that takes skin effect into account. They begin to deviate at frequencies beyond 2500 Hz due to the appearance of skin effect.

Hz. A similar result ($f \cong 80$ Hz) has been found for the sample LCS-3. Both LCS-1 and LCS-3 have higher permeability as compared to LCS-2, that causes the early appearance of skin effect in these materials.

The conclusion is that under negligible skin effect, the experimental results can be accurately predicted with the STL, using standard classical loss formula (Eq. 6.1). Therefore, it is confirmed one more time that the standard classical loss formula can be even applied at high inductions, under negligible skin effect.

In order to discuss the classical loss formula obtained from the SWM model (Eq. 6.20), the loss separation has been performed in the same frequency range not influenced by the skin effect. Fig. 6.16 shows the decomposition of total energy loss into the three components in sample LCS-2. Here, $W_{cl}^{(SWM)}$ is the classical loss obtained by adopting SWM model (Eq. 6.20), whereas the W_{cl} is the classical
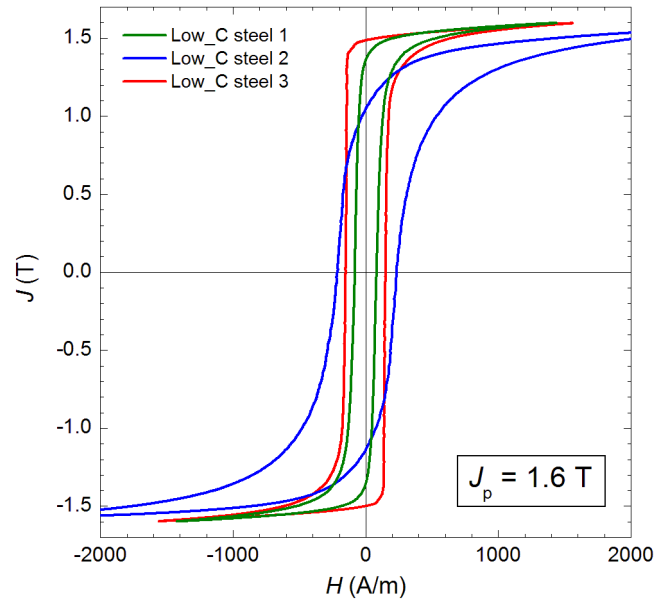
Fig. 6.13   DC hysteresis loops of the three adopted low carbon steel sheets at J_p=1.6 T. The loops resemble almost a step-like response.
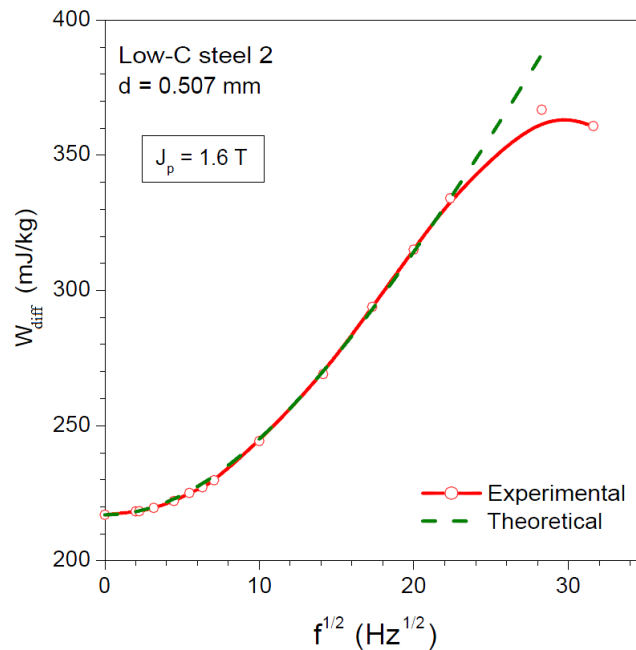
Fig. 6.14   The quantity $W_{diff} = W_{tot} - W_{cl}$ versus $\sqrt{f}$ in 0.507 mm thick LCS-2 at J_p=1.6 T (open circles) and its theoretical counter part $W_{diff} = W_{hyst} + W_{exc}$ (dashed line) where Eq. 6.21 has been applied to compute the excess loss. Deviation between the experimental and the theoretical results is observed at frequencies beyond 500 Hz due to the appearance of skin effect.
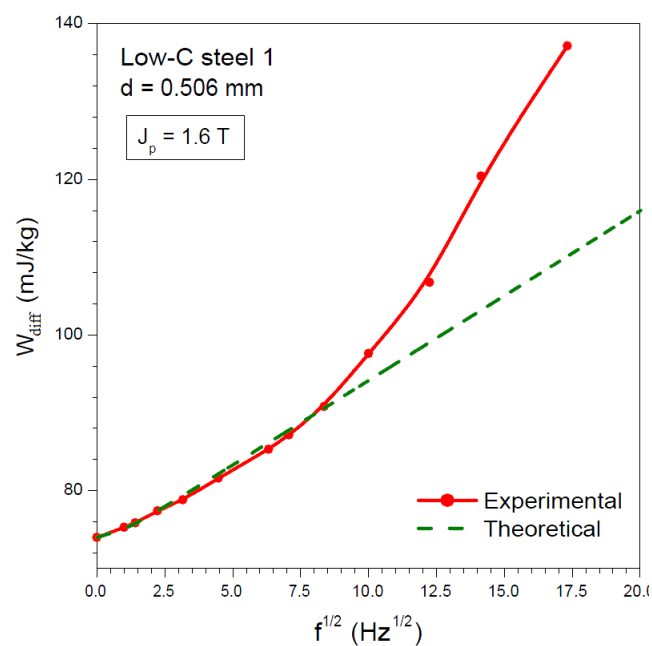
Fig. 6.15   The quantity $W_{\text{diff}} = W_{\text{tot}} - W_{\text{cl}}$ vs. $\sqrt{f}$ for a 0.506 mm thick LCS-1 at J_{p}=1.6 T (dots) along with the theoretical $W_{\text{diff}} = W_{\text{hyst}} + W_{\text{exc}}$ (dashed line) where Eq. 6.21 is applied to compute the excess loss. Again, a deviation between the experimental and theoretical results is observed beyond 60 Hz due the appearance of skin effect.
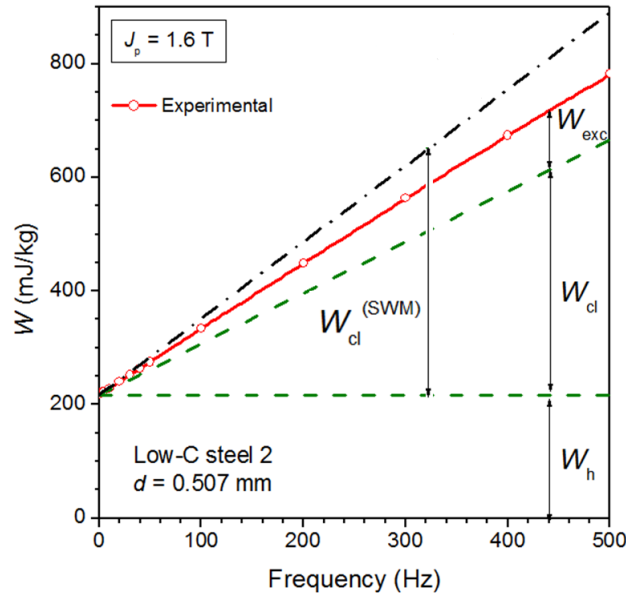
Fig. 6.16   Energy loss measurements performed on 0.507 mm thick LCS 2 at J_p=1.6 T upon the range of frequencies not influenced by the skin effect. $W_{cl}^{(SWM)}$ is the classical loss obtained from SWM model (Eq. 6.20), while W_{cl} is obtained by applying the standard classical loss formula (Eq. 6.1). It can be seen that $W_{cl}^{(SWM)}$ predict values even greater than the total loss (open circles).

loss obtained by applying standard classical formula (Eq. 6.1). It is observed that $W_{cl}^{(SWM)}$ predicts values even greater than the experimental total loss. This is in contradiction with the basic idea that the existence of domain walls and the corresponding local eddy current loss should in any case contribute to extra loss irrespective of the assumptions regarding the uniformity of flux density's distribution at low frequencies. In other words the values predicted by following the SWM model are not physical and the hypothesis of a step-like shape (Fig. 6.13) is not verified.

Similar results are obtained for sample LCS-1 and LCS-3, as shown in Fig. 6.17 and 6.18. Again it can be seen that the classical loss predicted by SWM overestimates the total loss. In conclusion, one can confidently state that STL predicts the energy loss vs. frequency behavior in all the investigated steel sheets accurately also at high induction levels. On the other end, the application of the SWM approach, leads to a huge contrast between the measured and predicted losses.
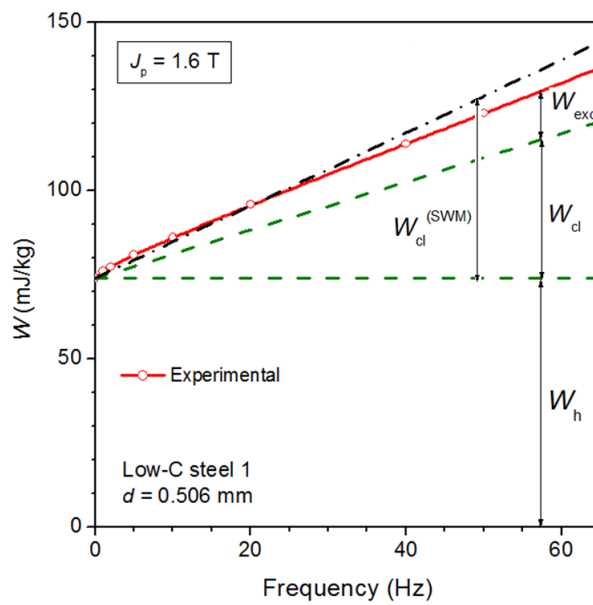
Fig. 6.17   Energy loss measurements performed on 0.506 mm thick LCS-1 sheet at J_p = 1.6 T, upon frequencies not influenced by skin effect. $W_{cl}^{(SWM)}$ is the classical loss obtained by SWM model (Eq. 6.20) while W_{cl} is obtained by applying the standard classical loss formula (Eq. 6.1). Again, it can be observed that $W_{cl}^{(SWM)}$ predicts values even greater than the experimentally obtained total loss.
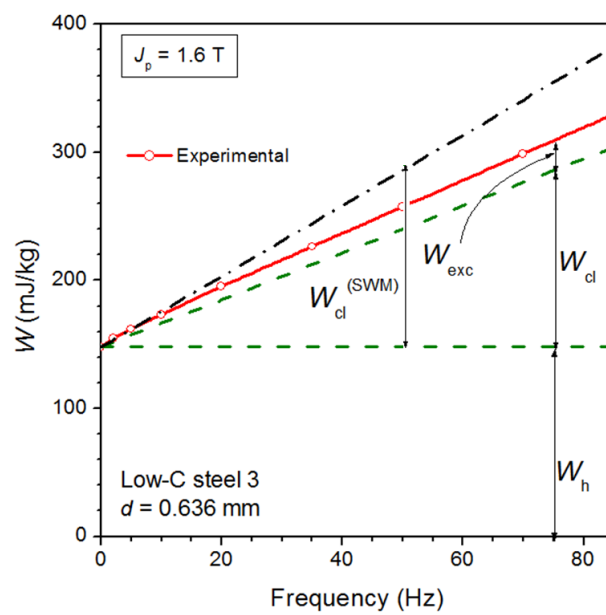
Fig. 6.18   Energy loss measurements performed on 0.636mm thick LCS 3 sheet at J_p=1.6T upon the region of frequencies not influenced by skin effect. $W_{cl}^{(SWM)}$ is the classical loss adopted by SWM model (Eq. 6.20), W_{cl} is obtained by applying the standard classical loss formula (Eq. 6.1). It can be seen that $W_{cl}^{(SWM)}$ (dashed line) predict values even greater than the total loss (open circles).

Chapter 7

Conclusion

7.1 Conclusion

The efficiency of the soft magnetic materials used in the core of electrical machines play a key role in the challenge of the global energy saving. For this reason, the accurate computation of magnetic loss is an important step in the design and optimization of electrical machines. Among the different models available, simple expressions based on the Steinmetz formula are currently applied because of their simplicity, but they reveal their limits especially under non conventional supply conditions. On the other end, the physical models based on the Statistical Theory of Loss and the loss separation concept can bridge the gap between engineers and physicists. In modern electrical machines and drives, the application of power electronics, new geometrical and magnetic configurations, high speed, and the needs in powertrain application of more compact configurations is responsible for complicated flux patterns, distorted waveforms, higher supply frequencies and high induction levels near saturation. For this reason, there is a need of experimental characterizations under non-conventional supply conditions comprising 1 and 2-dimensional fluxes, distorted

waveforms, high frequencies and higher induction levels, not always covered by standard measurement methods.

In this thesis, we have investigated non oriented soft magnetic materials under a wide range of supply conditions, including 2-D flux till magnetic saturation, 1-D flux at low and high inductions up to high frequencies. A complete characterization of Fe-(3.2 wt%)Si steel sheet was performed up to inductions close to magnetic saturation ($J_p/J_s \approx 0.98$) under 1 and 2-D fluxes. Models based on Statistical Theory of Loss and loss separation concept were applied under 1-D conditions, successfully extended to 2-D fluxes, and validated at least in the region of frequencies not influenced by the skin effect. The energy loss components under 1-D and 2-D conditions were interrelated in a rather universal fashion at all frequencies and it was shown that through a limited set of measurements under alternating and circular conditions, the corresponding behavior under a generic flux loci can be estimated.

Loss characterization of different non-oriented Fe-Si and low carbon steels were also performed under 1-D flux at very low and high sinusoidal inductions using Epstein frame, ring samples, and a compensated single sheet tester, over frequencies ranging from quasi-static conditions till 10 kHz. At low inductions, where a linear approximation of the constitutive relation holds, the solution of Maxwell equations provided an analytical approximation of the classical loss under skin effect conditions. Such result was applied to separate the loss and it was verified that STL found application at very low induction, even in the presence of skin effect. At high inductions, where the magnetic constitutive equation is highly non-linear, an analytical expression for the classical loss was worked out by using the so called Saturation Wave Magnetization (SWM) model, where the $B-H$ loop of a material is approximated by a step-like response. In this case, different low carbon steel sheets were tested at high induction levels where the $B-H$ loop seems to emulate a step-like response, but it was shown that the classical loss using SWM approach overestimated the experimental losses leading to "non-physical" results. On the other

end, in the region where skin effect is negligible, the experimental loss could be accurately predicted by using the standard classical loss formula in the framework of the STL.

A collateral research was developed during a visit to ENS, Cachan, France where a compensated Single Strip Tester with a simple and novel compensation technique was developed to reduce the systematic uncertainities introduce in measurements due to flux drop in the yokes of Single Sheet Testers. The developed compensated SST implements an effective MMF compensation method to neutralize the losses in the yoke through which the accurate characterization of soft magnetic steel sheets (both non-oriented and grain-oriented) were obtained.

References

[1] International energy outlook 2016. https://www.eia.gov/forecasts/ieo/emissions.cfm. Accessed: 2016-10-04.

[2] Energy-efficiency policy opportunities for electric motor-driven systems. http://www19.iadb.org/intal/intalcdi/PE/2011/08825.pdf. Accessed: 2016-09-04.

[3] K Atallah and D Howe. The calculation of iron losses in brushless permanent magnet dc motors. *Journal of magnetism and magnetic materials*, 133(1):578–582, 1994.

[4] E Sulaiman, T Kosaka, Y Tsujimori, and N Matsui. Design of 12-slot 10-pole permanant magnet flux-switching machine with hybrid excitation for hybrid electric vehicle. In *Power Electronics, Machines and Drives (PEMD 2010), 5th IET International Conference on*, pages 1–5. IET, 2010.

[5] G Radley and A Moses. Apparatus for experimental simulation of magnetic flux and power loss distribution in a turbogenerator stator core. *IEEE Transactions on Magnetics*, 17(3):1311–1316, 1981.

[6] Francis G Baily. The hysteresis of iron and steel in a rotating magnetic field. *Proceedings of the Royal Society of London*, 60(359-367):182–184, 1896.

[7] Carlo Appino, Mahmood Khan, Olivier De La Barriere, Carlo Ragusa, and Fausto Fiorillo. Alternating and rotational losses up to magnetic saturation in non-oriented steel sheets. *IEEE Transactions on Magnetics*, 52(5):1–4, 2016.

[8] Methods of measurement of the magnetic properties of electrical steel sheet and strip by means of an epstein frame. *IEC Standard Publication 60404-2*, 1996.

[9] Methods of measurement of the magnetic properties of electrical steel strip and sheet by means of a single sheet tester. *IEC Standard Publication 60404-3*, 2009.

[10] Steinmetz Chas Proteus. On the law of hysteresis. In *IEEE Proceeding*, volume 72, pages 197–221. USA: IEEE Press, 1984.

[11] Youguang Guo, Jian Guo Zhu, Jinjiang Zhong, Haiyan Lu, and Jian Xun Jin. Measurement and modeling of rotational core losses of soft magnetic materials used in electrical machines: A review. *Magnetics, IEEE Transactions on*, 44(2):279–291, 2008.

[12] Simon Steentjes, Georg von Pfingsten, Marco Hombitzer, and Kay Hameyer. Iron-loss model with consideration of minor loops applied to fe-simulations of electrical machines. *Magnetics, IEEE Transactions on*, 49(7):3945–3948, 2013.

[13] J Sievert. Recent advances in the one-and two-dimensional magnetic measurement technique for electrical sheet steel. *Magnetics, IEEE Transactions on*, 26(5):2553–2558, 1990.

[14] Herbert Hollitscher. Core losses in magnetic materials at very high flux densities when the flux is not sinusoidal. *Magnetics, IEEE Transactions on*, 5(3):642–647, 1969.

[15] RS Albir and AJ Moses. Improved dc bridge method employed to measure local power loss in electrical steels and amorphous materials. *Journal of Magnetism and Magnetic Materials*, 83(1):553–554, 1990.

[16] C Appino, F Fiorillo, C Ragusa, and Baochang Xie. Magnetic losses at high flux densities in nonoriented fe–si alloys. *Journal of Magnetism and Magnetic Materials*, 320(20):2526–2529, 2008.

[17] Takashi Todaka, Yoshitaka Maeda, and M Enokizano. Counterclockwise/clockwise (ccw/cw) rotational losses under high magnetic field. *Prezglad, Elektrotechniczny*, 85:20–24, 2009.

[18] Carlo Appino, Fausto Fiorillo, and Carlo Ragusa. One-dimensional/two-dimensional loss measurements up to high inductions. *Journal of Applied Physics*, 105(7):7E718, 2009.

[19] Ayman S Abdel-Khalik, Shehab Ahmed, Ahmed M Massoud, and Ahmed A Elserougi. An improved performance direct-drive permanent magnet wind generator using a novel single-layer winding layout. *IEEE Transactions on Magnetics*, 49(9):5124–5134, 2013.

[20] Mi-Jung Kim, Su-Yeon Cho, Ki-Doek Lee, Jae-Jun Lee, Jung-Ho Han, Tae-Chul Jeong, Won-Ho Kim, Dae-Hyun Koo, and Ju Lee. Torque density elevation in concentrated winding interior pm synchronous motor with minimized magnet volume. *IEEE Transactions on Magnetics*, 49(7):3334–3337, 2013.

[21] Jin-hee Lee and Byung-Il Kwon. Optimal rotor shape design of a concentrated flux ipm-type motor for improving efficiency and operation range. *IEEE Transactions on Magnetics*, 49(5):2205–2208, 2013.

[22] Zbigniew Gmyrek, Aldo Boglietti, and Andrea Cavagnino. Estimation of iron losses in induction motors: Calculation method, results, and analysis. *IEEE Transactions on Industrial Electronics*, 57(1):161–171, 2010.

[23] TV Tran, F Moussouni, S Brisset, and P Brochet. Adapted output space-mapping technique for a bi-objective optimization. *IEEE Transactions on Magnetics*, 46(8):2990–2993, 2010.

[24] Ferenc Preisach. Über die magnetische nachwirkung. *Zeitschrift für physik*, 94(5-6):277–302, 1935.

[25] I Mayergoyz. Mathematical models of hysteresis. *IEEE Transactions on magnetics*, 22(5):603–608, 1986.

[26] Chas Proteus Steinmetz. On the law of hysteresis. *Transactions of the American Institute of Electrical Engineers*, 9(1):1–64, 1892.

[27] G Ban and G Bertotti. Dependence on peak induction and grain size of power losses in nonoriented sife steels. *Journal of Applied Physics*, 64(10):5361–5363, 1988.

[28] F material. https://www.mag-inc.com/Products/Ferrite-Cores/F-Material. Accessed: 2017-01-23.

[29] Jürgen Reinert, Ansgar Brockmeyer, and Rik WAA De Doncker. Calculation of losses in ferro-and ferrimagnetic materials based on the modified steinmetz equation. *IEEE Transactions on Industry applications*, 37(4):1055–1061, 2001.

[30] Ansgar Brockmeyer. *Dimensionierungswerkzeug für magnetische Bauelemente in Stromrichteranwendungen*. Verlag der Augustinus-Buchh., 1997.

[31] Jieli Li, Tarek Abdallah, and Charles R Sullivan. Improved calculation of core loss with nonsinusoidal waveforms. In *Industry Applications Conference, 2001. Thirty-Sixth IAS Annual Meeting. Conference Record of the 2001 IEEE*, volume 4, pages 2203–2210. IEEE, 2001.

[32] G Bertotti. A general statistical approach to the problem of eddy current losses. *Journal of magnetism and Magnetic Materials*, 41(1):253–260, 1984.

[33] Pierre Weiss. L'hypothèse du champ moléculaire et la propriété ferromagné-tique. *J. Phys. Theor. Appl.*, 6(1):661–690, 1907.

[34] Vincent Del Toro. *Electric machines and power systems*. Prentice Hall Inc., Old Tappan, NJ, 1985.

[35] Charles Kittel. Physical theory of ferromagnetic domains. *Reviews of modern Physics*, 21(4):541, 1949.

[36] HJ Williams, W Shockley, and Ch Kittel. Studies of the propagation velocity of a ferromagnetic domain boundary. *Physical Review*, 80(6):1090, 1950.

[37] Giorgio Bertotti. Physical interpretation of eddy current losses in ferromagnetic materials. i. theoretical considerations. *Journal of applied Physics*, 57(6):2110–2117, 1985.

[38] G Bertotti. Space-time correlation properties of the magnetization process and eddy current losses: Applications. i. fine wall spacing. *Journal of applied physics*, 55(12):4339–4347, 1984.

[39] Giorgio Bertotti. *Hysteresis in magnetism: for physicists, materials scientists, and engineers*. Academic press, 1998.

[40] C Appino, C Ragusa, and F Fiorillo. Can rotational magnetization be theoretically assessed? *International Journal of Applied Electromagnetics and Mechanics*, 44(3, 4), 2014.

[41] C Ragusa, C Appino, and F Fiorillo. Magnetic losses under two-dimensional flux loci in fe–si laminations. *Journal of magnetism and magnetic materials*, 316(2):454–457, 2007.

[42] Philip N Ross and Paul Stonehart. The relation of surface structure to the electrocatalytic activity of tungsten carbide. *Journal of Catalysis*, 48(1-3):42–59, 1977.

[43] AJ Moghaddam and AJ Moses. Localised power loss measurement using remote sensors. *Magnetics, IEEE Transactions on*, 29(6):2998–3000, 1993.

[44] Carlo Ragusa, Carlo Appino, and Fausto Fiorillo. Comprehensive investigation of alternating and rotational losses in non-oriented steel sheets. *Przeglad Elektrotechniczny*, 85(1):7–10, 2009.

[45] Fausto Fiorillo. Measurements of magnetic materials. *Metrologia*, 47(2):S114, 2010.

[46] Methods for determining the magnetic properties of magnetic steel sheet and strip with 25cm epstein frame. *EURONORM*, pages 118–87.

[47] Methods of measurement of the dc magnetic properties of magnetically soft materials. *IEC standard Publication 60404-4*.

[48] Fausto Fiorillo. *Measurement and characterization of magnetic materials*. North-Holland, 2004.

[49] CG Svala. An improved, practical burrows permeameter. *Magnetics, IEEE Transactions on*, 12(6):816–818, 1976.

[50] John P Barranger. Very high-temperature permeameter. *Journal of Applied Physics*, 42(4):1796–1797, 1971.

[51] A Nafalski, AJ Moses, T Meydan, and MM Abousetta. Loss measurements on amorphous materials using a field-compensated single-strip tester. *Magnetics, IEEE Transactions on*, 25(5):4287–4291, 1989.

[52] LR Dupre, F Fiorillo, Jan Melkebeek, AM Rietto, and C Appino. Loss versus cutting angle in grain-oriented fe–si laminations. *Journal of magnetism and magnetic materials*, 215:112–114, 2000.

[53] LR Dupre, F Fiorillo, C Appino, AM Rietto, and Jan Melkebeek. Rotational loss separation in grain-oriented fe–si. *Journal of Applied Physics*, 87(9):6511–6513, 2000.

[54] F Fiorillo, LR Dupre, C Appino, and AM Rietto. Comprehensive model of magnetization curve, hysteresis loops, and losses in any direction in grain-oriented fe-si. *IEEE Transactions on Magnetics*, 38(3):1467–1476, 2002.

[55] F Fiorillo, C Appino, and Carlo Ragusa. Loss decomposition under two-dimensional flux loci in non-oriented steel sheets. *Przegląd Elektrotechniczny*, 83:25–30, 2007.

[56] C Ragusa, Stanislaw Zurek, C Appino, and Anthony John Moses. An intercomparison of rotational loss measurements in non-oriented fe–si alloys. *Journal of Magnetism and Magnetic Materials*, 320(20):e623–e626, 2008.

[57] N Nencib, A Kedous-Lebouc, and B Cornut. 2d analysis of rotational loss tester. *Magnetics, IEEE Transactions on*, 31(6):3388–3390, 1995.

[58] Yoshitaka Maeda, Hiroyasu Shimoji, Takashi Todaka, and Masato Enokizono. Rotational power loss of magnetic steel sheets in a circular rotational magnetic field in ccw/cw directions. *Journal of Magnetism and Magnetic Materials*, 320(20):e567–e570, 2008.

[59] Olivier de la Barrière, Carlo Appino, Fausto Fiorillo, Michel Lécrivain, Carlo Ragusa, and Patrice Vallade. A novel magnetizer for 2d broadband characterization of steel sheets and soft magnetic composites. *International Journal of Applied Electromagnetics and Mechanics*, 48(2, 3):239–245, 2015.

[60] F Fiorillo, E Barbisio, and Carlo Stefano Ragusa. Accurate measurement of magnetic power losses and hysteresis loops under generic induction waveforms with minor loops. 2004.

[61] J Sievert and Braunschweig Physikalisch-Technische Bundesanstalt. *Magnetic measurements on electrical steels using Epstein und SST methods*. Wirtschaftsverl. NW, Verlag für Neue Wiss., 2001.

[62] JD Sievert and D Son. On the effective magnetic path length used for field strength and loss determination. *Journal of Magnetism and Magnetic Materials*, 41(1):235–237, 1984.

[63] F Brailsford. Alternating hysteresis loss in electrical sheet steels. *Electrical Engineers, Journal of the Institution of*, 84(507):399–407, 1939.

[64] Sergey E Zirka, Yury I Moroz, Philip Marketos, and Anthony J Moses. Viscosity-based magnetodynamic model of soft magnetic materials. *IEEE transactions on magnetics*, 42(9):2121–2132, 2006.

[65] O Bottauscio, Mario Chiampi, and D Chiarabaglio. Iron losses in soft magnetic materials under periodic non-sinusoidal supply conditions. *Physica B: Condensed Matter*, 275(1):191–196, 2000.

[66] Giorgio Bertotti. Hysteresis in magnetism: for physicists, material scientists, and engineers. *Academic„ San Diego*, 1998.

[67] Cinzia Beatrice, Carlo Appino, Olivier de la Barrière, Fausto Fiorillo, and Carlo Ragusa. Broadband magnetic losses in fe-si and fe-co laminations. *IEEE Transactions on Magnetics*, 50(4):1–4, 2014.